Quantum Hall Effect-Mediated Josephson Junctions in Graphene

A DISSERTATION PRESENTED
BY
JING KATHLEEN SHI
TO
THE DEPARTMENT OF PHYSICS

IN PARTIAL FULFILLMENT OF THE REQUIREMENTS
FOR THE DEGREE OF
DOCTOR OF PHILOSOPHY
IN THE SUBJECT OF
PHYSICS

HARVARD UNIVERSITY
CAMBRIDGE, MASSACHUSETTS

MAY 2020

Thesis advisor: Professor Philip Kim Jing Kathleen Shi

Quantum Hall Effect-Mediated Josephson Junctions in Graphene

Abstract

Evidence supporting the existence of Majorana bound states has been observed in systems such as superconducting proximitized semiconducting nanowires, atomic chains and topological insulators. This dissertation explores the possibility of engineering these states in graphene quantum Hall states hybridized with superconducting niobium nitride (NbN) one-dimensional wires. Stepwise modulations of the critical current of graphene Josephson junctions in the quantum Hall regime were observed, with the origin being attributed to the change in the number of underlying quantum Hall edge states in graphene. This is the first observation of the superconducting coupling between a superconductor and quantum Hall edge states showing up as changes in the critical current of a Josephson junction. Further theoretical calculations corroborated the conjecture that topological gaps would open up in quantum Hall-superconductor systems, allowing for the generation of not only Majorana bound states, but a myriad of topological states that are inaccessible in other systems mentioned above.

Contents

Previous publications and list of authors

The following authors contributed to Chapter 3, Chapter 4, and Chapter 5: Gil-Ho Lee, Fernando Dominguez, Yuval Ronen, Önder Gül, Seung Hyun Park, Kenji Watanabe, Takashi Taniguchi, Ewelina Hankiewicz, Philip Kim

The following authors contributed to Chapter 6: Yuval Ronen, Önder Gül, Kenji Watanabe, Takashi Taniguchi, Philip Kim

Listing of figures

This thesis is dedicated to dear family, friends, teachers, and everyone else who have bestowed great inspiration and strength upon me.

Acknowledgments

I WOULD LIKE TO express my deepest appreciation to my dissertation committee. First and foremost, this dissertation would not have been possible without six years of guidance, support and encouragement from my research advisor, Prof. Kim. He has the substance of a genius; he is knowledgeable and meticulous, yet humble and dependable. I would also like to extend my deepest gratitude to Prof. Bertrand Halperin for having taught me a year of graduate quantum mechanics, another course on topological states of matters, and for providing insightful comments and raising interesting questions during our discussions. I have learned a tremendous amount from Prof. Halperin. I am also extremely grateful to Prof. Jenny Hoffman, whom I had the honor to work with before joining the Kim lab. In addition to being a brilliant scientist, her dedication to research, family, mentoring, and her passion for running have inspired me and many others alike.

I am hugely indebted to Gil-Ho Lee, now a professor at Pohang University of Science and Technology (POSTECH) in Korea. Gil-Ho played an instrumental role in the main project presented in this dissertation, initiating projects involving quantum Hall and superconductivity, and offered a lot of indispensable guidance and mentorship toward the success of my project. In addition, I am in gratitude to our theorist collaborators, Dr. Fernando Dominguez and Prof. Ewelina Hankiewicz from Würzburg University in Germany. I learned a lot over numerous Zoom meetings we had. I would also like to extend my gratitude to Yuval Ronen and Önder Gül for helpful discussions and interesting ideas they proposed, as well as Prof. Amir Yacoby and members of the Yacoby lab, for their continuous support and friendship.

I would like to express my heartfelt thanks to other colleagues and friends who influenced my research career at Harvard. Dennis Huang and Can-Li Song, for being my first mentors in Jenny's lab; Jayakanth Ravichandran, for his mentorship and candid advice when I first joined the Kim lab; Xiaomeng Liu and Frank Zhao, for being wonderful collaborators in lab and research projects; Austin Cheng, for answering numerous questions of mine. In addition, I am deeply appreciative of the administrative support from Carolyn Moore and Hannah Belcher, as well as equipment support from the Center for Nanoscale Systems (CNS) and other Kim lab members.

Last but not the least, I am very grateful for the support and friendship from the following people: Lisa Cacciabaudo and Jacob Barandes, classmates from 2012 physics G1 class, all members of the Kim lab, teachers and classmates from the Japanese Program, other personal friends, as well as my family.

Thank you all, for gifting me eight years of irreplaceable experiences and memories, and for shaping me into the person I am today.

Q: What is a topologist?

A: Someone who cannot distinguish between a doughnut

and a coffee cup.

1

Topological states and Majorana fermions

Majorana zero modes are zero-energy, degenerate states residing at the boundary between a topological superconductor and a trivial insulator, such as vacuum. They belong to class of excitations called non-abelian anyons, which serve as the basis for topological quantum bits (qubits) with application in topological quantum computation. Topological quantum computing holds great promise for fault-tolerant quantum computation owing to its topological protection. Because of this promise, the creation, detection and braiding of non-abelian anyons such as Majorana zero

modes, also known as Majorana fermions, have been actively pursued on various material platforms.

In this chapter, we provide a brief, theoretical introduction to topological states of matter, with a focus on superconducting proximitized spin-helical states. The generation and detection of Majorana zero energy modes in these systems will also be discussed.

1.1 Topology in Mathematics

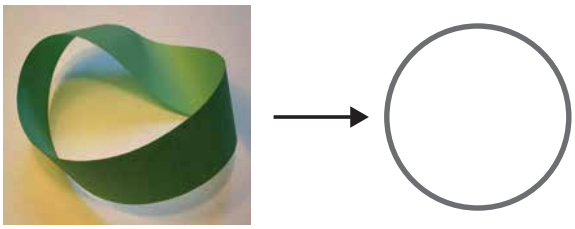

Figure 1.1: The edge of a Möbius strip (left) is equivalent to a circle (right) as both objects can be smoothly deformed into each other.

Topology is a branch of mathematics concerning the geometry and the connectivity of objects in space. If one object can be smoothly deformed into another object, then the two objects are said to be topologically equivalent. For instance, the edge of a Möbius strip is equivalent to a circle (Fig. 1.1) as the Möbius strip has one continuous boundary and can be gradually deformed into a circle.

Consider the familiar example of closed, two-dimensional surfaces in three dimensions consisting of an orange, a donut, and a coffee cup (Fig. 1.2). An orange is different from a donut or a coffee cup, because an orange can never be changed smoothly into either of the latter without some drastic alteration that punches a hole in the middle. On the other hand, an orange can be deformed into the surface of a disk or a bowl, making them topologically equivalent.

This difference in geometry is expressed as a topological invariant, the Euler characteristic χ. For

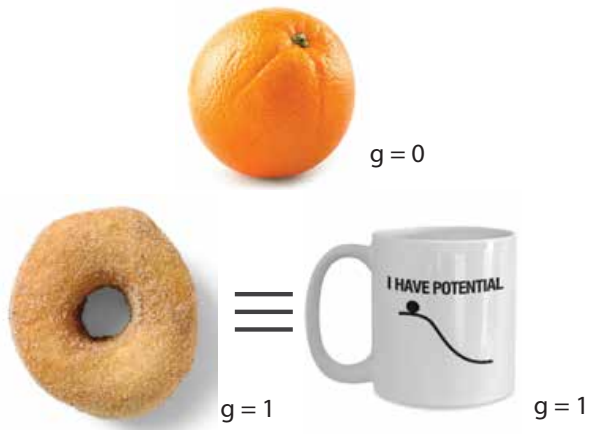

Figure 1.2: The difference in topology of an orange, a donut, and a coffee cup can be interpreted as the difference in the number of holes in these objects, which is characterized by the genus g. A donut ($g = 1$) is equivalent to a coffee cup ($g = 1$), but not to an orange ($g = 0$).

surfaces, the Gaussian curvature K integrated over the surface area defines the Euler characteristic,[27]

$$\chi = \frac{1}{2\pi} \int_S K \, dA, \tag{1.1}$$

referred to as the Gauss-Bonnet theorem. Thus, for a sphere of radius R, where $K = 1/R^2$, χ is equal to 2. The classification can also be represented by the genus g, which counts the number of holes present in the object. The genus is related to χ by $\chi = 2 - 2g$, so for a sphere, $g = 0$.

Although it originated in mathematics, the concept of topology is used in condensed matter systems to classify materials and to make important predictions.

1.2 Topological insulators

Insulators are materials with an electronic energy gap that separates the ground state from the excited states, and topologically equivalent insulators are insulators that can be transformed into one another by slowly (adiabatically) changing the Hamiltonian while the system remains in its ground

state. During such an adiabatic transformation between topologically equivalent insulators, the gap necessarily remains finite. Conversely, a change between two topologically *distinct* insulators involves a phase transition where the gap vanishes. [13]

The term "topological insulator" refers to an insulator that is topologically non-trivial, the occurrence of which in nature is rare compared to the vast majority of "trivial" insulators that are equivalent to vacuum. The simplest description of the topological classification is based on the band theory of solids, which utilizes the independent electron approximation.

1.2.1 The topology of the Brillouin zone

Consider a lattice with crystal momentum $\mathbf{k}$. Bloch's theorem gives $|\psi(\mathbf{k})\rangle = e^{i\mathbf{k}\cdot\mathbf{r}}|u(\mathbf{k})\rangle$, where $|u(\mathbf{k})\rangle$ is an eigenstate of the Bloch Hamiltonian,

$$H(\mathbf{k}) = e^{i\mathbf{k}\cdot\mathbf{r}} H e^{-i\mathbf{k}\cdot\mathbf{r}}, \tag{1.2}$$

in which the eigenvalues $E_n(\mathbf{k})$ give the energy spectrum and the band structure.

The analogy to topology in mathematics lies in the translational symmetry of the lattice, $H(\mathbf{k} + \mathbf{G}) = H(\mathbf{k})$, where $\mathbf{G}$ is the reciprocal lattice vector. The crystal momentum $\mathbf{k}$ as defined in the Brillouin zone obeys the relation $\mathbf{k} \equiv \mathbf{k} + \mathbf{G}$, which is equivalent to the topology of a torus T^d in d dimensions. The geometry of the Brillouin zone allows the insulators to be classified with a topological invariant. The Brillouin zone-torus can be thought of as if it were mapped onto the Bloch Hamiltonian with an energy gap.

1.2.2 The Chern invariant

The Bloch states $|u(\mathbf{k})\rangle$ are defined up to a phase, due to the phase ambiguity in the wavefunction,

$$|u(\mathbf{k})\rangle \to e^{i\varphi(\mathbf{k})}|u(\mathbf{k})\rangle. \tag{1.3}$$

Furthermore, the Berry connection $\mathbf{A}$ is defined as

$$\mathbf{A} = -i\langle(u(\mathbf{k})|\nabla_{\mathbf{k}}|u(\mathbf{k})\rangle, \tag{1.4}$$

and transforms as $\mathbf{A} \to \mathbf{A} + \nabla_{\mathbf{k}}\varphi(\mathbf{k})$ under Eq. 1.3.

$\mathbf{A}$ is analogous to the electromagnetic vector potential in that it is not gauge invariant. However, the magnetic flux is gauge invariant. Therefore, a gauge invariant magnetic flux analog called the Berry phase can be defined as

$$\gamma_C = \oint_C \mathbf{A} \cdot d\mathbf{k} = \int_S \mathcal{F}\, d\mathbf{k}, \tag{1.5}$$

where $\mathcal{F} = \nabla \times \mathbf{A}$ is the Berry curvature.

The definition of the Berry phase (Eq. 1.5) is the condensed matter version of the Gauss-Bonnet equation (Eq. 1.1). Moreover, the Berry phase is quantized to be multiples of 2π. This quantization comes from the fact that for a closed surface, the "inside" and the "outside" of the line integral in Eq. 1.5 are arbitrarily defined, therefore the integral of the "inside" and the "outside" can only differ by multiples of 2π. It then follows that the Berry curvature integrated over the entire surface containing both the "inside" and the "outside" must be multiples of 2π.

A topological invariant called the Chern number[27] is defined for a closed surface S as

$$n = \frac{1}{2\pi}\int_S \mathcal{F}\, d\mathbf{k}, \tag{1.6}$$

in which n must take integer values, with the Berry curvature $\mathcal{F}$ playing the role of the Gaussian curvature K in the Gauss-Bonnet equation.

1.3 Integer quantum Hall effect as a topological state

At the boundary of two topologically distinct insulators, the distinctiveness in the topology demands closure of the gap and the subsequent emergence of metallic states. The key to topological protection is that these metallic states are independent of the sample geometry and are thus robust against impurities in the sample, as the topology of the insulator remains invariant under an adiabatic change of the Hamiltonian. While most insulators are band insulators that are equivalent to the vacuum, topological systems that host conducting edge states such as the integer quantum Hall effect, have become a subject of interest to physicists [11,18,30].

The quantum Hall effect describes a phenomenon where the bulk is insulating with quantized conducting chiral edge states. It arises in a two-dimensional electron gas system in a perpendicular magnetic field. The circular orbits of the electrons are quantized with the cyclotron frequency ω_c, resulting in quantized Landau levels with energy

$$\varepsilon_m = \hbar\omega_c(m + \frac{1}{2}). \tag{1.7}$$

These energy levels are gapped just as in an ordinary insulator. However, there exist one-dimensional chiral edge states around the sample with a quantized Hall conductivity,

$$\sigma_{xy} = N\frac{e^2}{h}, \tag{1.8}$$

where N is an integer. Thouless, Kohmoto, Nighingale and den Nijs (TKNN) [36] computed N with the Kubo formula, and showed that it is identical to the Chern invariant n, elucidating the topologi-

cal nature of the quantum Hall edge states.

A semi-classical skipping-orbit picture is often used to understand the quantum Hall edge states. Under a magnetic field, the electrons in the bulk are localized whereas those at the edges propagate with a skipping-orbit motion and are able to carry an electrical current (Fig. 1.3).

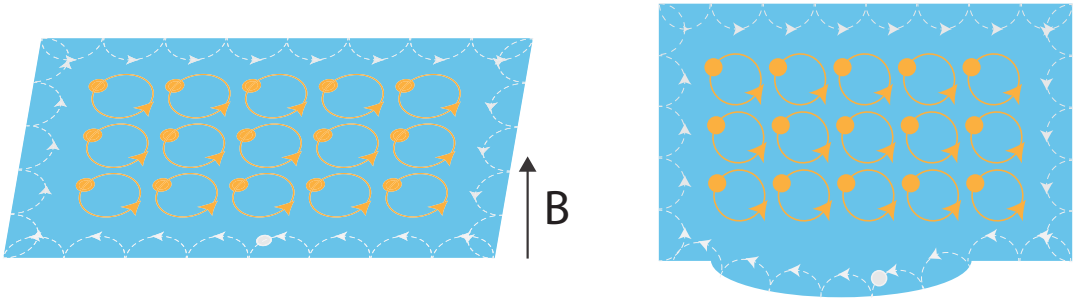

Figure 1.3: The semi-classical picture of the integer quantum Hall effect. Left: the quantum Hall effect develops in a 2D electron system in the presence of a perpendicular magnetic field. The electrons form closed orbits in the bulk and are non-conducting. However, as the orbits cannot be completed at the edge, conducting chiral edge states are formed. Right: the quantum Hall effect is robust against back scattering caused by edge defects and non-magnetic impurities.

The quantum Hall effect and its robustness have been verified experimentally in two-dimensional electron gas (2DEGs) systems; it was first observed in silicon metal-oxide-semiconductor field-effect transistors (MOSFET) in 1980 by von Klitzing [18], and later in GaAs heterostructures [29], exfoliated graphene systems [28,46,47], transition metal dichacogenides (TMDCs) [22], as well as black phosphorus [43]. The quantization of σ_{xy} has been measured to an accuracy of 1 part in 10^9 [38].

In the case of graphene, with a linear dispersion close to the Dirac point, the energy for the nth Landau level is

$$E_n = \mathrm{sgn}(n)\sqrt{2\,e\hbar\, v_F^2|n|B}, \tag{1.9}$$

where $n > 0$ is the electron-like Landau level indices, and $n < 0$ the hole-like ones.

Assuming that the energy separation of E_n is much larger than the Zeeman splitting, and ignoring the effect of the electron-electron interaction, the spin and valley degrees of freedom give each

Landau level a 4-fold degeneracy. The quantized conductance in graphene is

$$\sigma_{xy} = \pm 4 \left(n + \frac{1}{2} \right) \frac{e^2}{h}, \tag{1.10}$$

where n is an integer and $n \geqslant 0$.

1.4 Topological superconductors

Besides insulators, superconductors also possess a finite energy gap. In the Bardeen-Cooper-Schrieffer (BCS) formalism, the electrons at the vicinity of the Fermi energy form Cooper pairs via the electron-phonon interaction, opening up a gap between the superconducting ground state and the excited quasiparticle states.

The BCS Hamiltonian is

$$H_{\text{BCS}} = \sum_{\mathbf{k}\sigma} \varepsilon_{\mathbf{k}} c^\dagger_{\mathbf{k}\sigma} c_{\mathbf{k}\sigma} + \sum_{\mathbf{k}\mathbf{k}'} U_{\mathbf{k}\mathbf{k}'} c^\dagger_{\mathbf{k}\uparrow} c^\dagger_{-\mathbf{k}\downarrow} c_{-\mathbf{k}'\downarrow} c_{\mathbf{k}'\uparrow}, \tag{1.11}$$

where U is the electron-electron interaction, and $\varepsilon_{\mathbf{k}} = (\hbar\mathbf{k})^2/2m - \mu$. In a mean field treatment where one defines $a_{\mathbf{k}} = \langle c^\dagger_{\mathbf{k}\uparrow} c^\dagger_{-\mathbf{k}\downarrow} \rangle$, the BCS Hamiltonian can be written as

$$H_{\text{BCS}} = \sum_{\mathbf{k}\sigma} \varepsilon_{\mathbf{k}} c^\dagger_{\mathbf{k}\sigma} c_{\mathbf{k}\sigma} + \sum_{\mathbf{k}} \left(\Delta_{\mathbf{k}} c^\dagger_{\mathbf{k}\uparrow} c^\dagger_{-\mathbf{k}\downarrow} + \Delta^*_{\mathbf{k}} c_{-\mathbf{k}\downarrow} c_{\mathbf{k}\uparrow} \right) + \sum_{\mathbf{k}} \Delta^*_{\mathbf{k}} a_{\mathbf{k}}, \tag{1.12}$$

where the order parameter $\Delta_{\mathbf{k}} = \sum_{\mathbf{k}'} U_{\mathbf{k}\mathbf{k}'} a_{\mathbf{k}'}$. For simplicity, we assume a constant order parameter Δ for s-wave pairing.

We can further introduce the spinor $\Psi_{\mathbf{k}} \equiv \begin{pmatrix} c_{\mathbf{k},\uparrow} & c_{\mathbf{k},\downarrow} & c^\dagger_{-\mathbf{k},\uparrow} & c^\dagger_{-\mathbf{k},\downarrow} \end{pmatrix}^T$, and write the BCS Hamiltonian with the Bogoliubov-de Gennes (BdG) formalism. Dropping the constant term, we

have

$$H_{\mathrm{BCS}} = \sum_{\mathbf{k}} \Psi_{\mathbf{k}}^{\dagger} H_{\mathrm{BdG}}(\mathbf{k}, \Delta) \Psi \mathbf{k}, \tag{1.13}$$

where

$$H_{\mathrm{BdG}}(\mathbf{k}, \Delta) = \frac{1}{2} \begin{pmatrix} \varepsilon(\mathbf{k}) & 0 & 0 & \Delta \\ 0 & \varepsilon(\mathbf{k}) & -\Delta & 0 \\ 0 & -\Delta^* & \varepsilon(-\mathbf{k}) & 0 \\ \Delta^* & 0 & 0 & \varepsilon(-\mathbf{k}) \end{pmatrix}. \tag{1.14}$$

More compactly, H_{BdG} can be written as

$$H_{\mathrm{BdG}}(\mathbf{k}, \Delta) = \varepsilon(\mathbf{k}) \tau^z \otimes I_{2\times 2} - (\mathrm{Re}\Delta) \tau^y \otimes \sigma^y - (\mathrm{Im}\Delta) \tau^x \otimes \sigma^y, \tag{1.15}$$

where τ^a and σ^a are Pauli matrices for particle-hole and spins, respectively.

Diagonalizing H_{BdG} gives the energy spectrum

$$E_{\pm} = \pm \sqrt{\varepsilon(\mathbf{k})^2 + |\Delta|^2}. \tag{1.16}$$

The spectrum has two doubly degenerate bands, as a result of the electron-hole redundancy introduced by the spinor $\Psi_{\mathbf{k}}$. As shown in Fig. 1.4a, the system exhibits a gap when $\Delta \neq 0$. However, we can also achieve a very similar energy spectrum in a band insulator with a fine-tuned particle-hole symmetry. The only difference is that in the case of a superconductor, the quasiparticle excitations are combinations of particle and hole states, not fermionic excitation as in the case of a band insulator.

With the Bogoliubov-de Gennes approach, we can investigate the consequences of having a *p*-wave pairing in a 1D spinless wire. Starting from the mean-field equation (Eq. 1.12), we first drop spin dependence. Noting the fact that the *s*-wave pairing is not possible in a 1D spinless wire, we

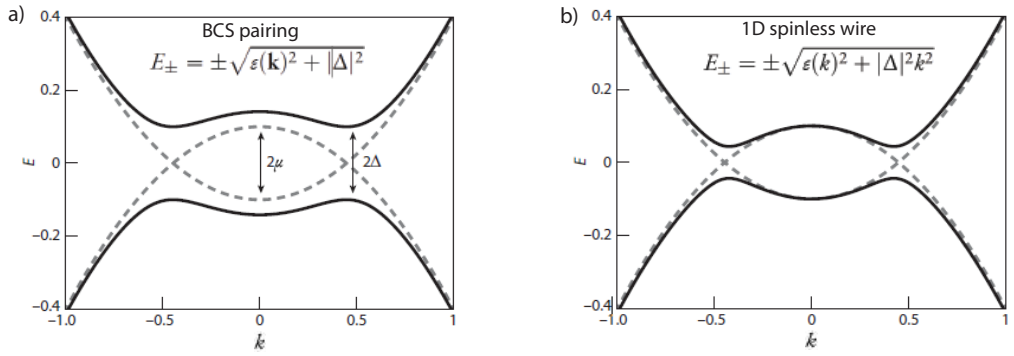

Figure 1.4: Energy spectra of an s-wave superconductor and a 1D spinless wire. $\varepsilon(k) = (\hbar k)^2/2m - \mu$, dotted line: $m = 0.1, \mu = 0.1, |\Delta| = 0$; solid line: $m = 0.1, \mu = \Delta = 0.1$. **a**, Each band is doubly degenerate. A topologically trivial gap opens for $\Delta \neq 0$. **b**, $\mu = 0$ separates the system into the weak pairing regime ($\mu > 0$), and the strong pairing regime ($\mu < 0$). While the weak pairing regime resembles the s-wave superconductors in **a**, the strong pairing regime is a gapped insulator without a pairing Δ, and a topological superconductor with a non-zero pairing Δ. Figures adapted from Bernevig and Huges, 2013[5].

introduce a momentum-dependent p-wave potential, and the Hamiltonian becomes

$$H_{\text{1D wire}} = \sum_k \varepsilon_k c_k^\dagger c_k + \sum_k \Delta k c_k c_{-k} + \Delta^* k c_{-k} c_k. \tag{1.17}$$

The Bogoliubov-de Gennes equation is

$$H_{\text{BdG}} = \sum_k \frac{1}{2} \Psi_k^\dagger \begin{pmatrix} \varepsilon(k) & \Delta k \\ \Delta^* k & -\varepsilon(k) \end{pmatrix} \Psi_k, \tag{1.18}$$

where $\Psi_k = \begin{pmatrix} c_k & c_{-k}^\dagger \end{pmatrix}^T$. The energy spectrum is gapped as long as $\mu \neq 0$,

$$E_\pm = \pm\sqrt{\varepsilon(k)^2 + |\Delta|^2 k^2}. \tag{1.19}$$

In fact, $\mu = 0$ is the critical point that separates two regimes, the weak-pairing phase for $\mu > 0$ and the strong-pairing phase for $\mu < 0$ (Fig. 1.4b). The weak-pairing regime is similar to a BCS

superconductor, resulting in a metallic system in the absence of pairing, whereas the strong pairing regime is a gapped insulator without pairing, and is the topological superconducting phase.

The p-wave 1D wire is also referred to as a Kitaev chain [17], owing to Kitaev who first predicted the existence of a mode described by Majorana operators occurring at each end of such a wire. The Majorana mode emerges directly from solving the Bogoliubov-de Gennes Hamiltonian in the real space and rewriting it with Majorana operators. The real-space picture of a 1D spinless wire is illustrated in Fig. 1.5. The pairing that leaves two unpaired half-fermions (Majorana modes) at both ends of the wire corresponds to the topological phase (Fig. 1.5, lower).

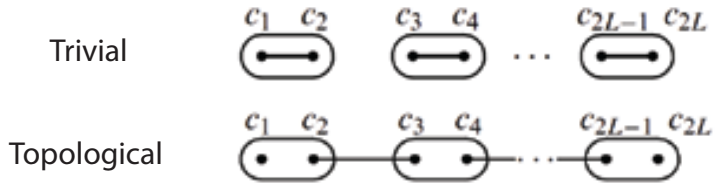

Figure 1.5: An illustration of the Kitaev 1D spinless chain. Two c operators combine to form one fermion, the resulting chain is either in the trivial state (upper) or the topological state (lower). Adapted from Kitaev, 2001 [17].

1.4.1 Majorana modes and topological quantum computing

Majorana fermions are hypothetical elementary particles that are their own antiparticles. They satisfy

$$\gamma^\dagger = \gamma, \quad \{\gamma_i, \gamma_j\} = 2\delta_{ij}. \tag{1.20}$$

Majorana fermions are sometimes viewed as half of a fermion, as a complex fermionic operator c can be expressed as

$$\begin{aligned} c &= (\gamma_1 + i\gamma_2)/2 \\ c^\dagger &= (\gamma_1^\dagger - i\gamma_2^\dagger)/2. \end{aligned} \tag{1.21}$$

Note that the γ operators are equivalent to the c operators used in Kitaev's original paper and in Fig. 1.5.

Majorana states appearing at the end of a 1D p-wave wire are a pair of degenerate zero-energy states, also referred to as Majorana zero modes. The non-abelian statistics of Majorana zero modes come from the fact that exchanging their positions is equivalent to performing a unitary transformation on the Hilbert space, which in general does not commute with one another. Specifically, an exchange of the Majorana zero modes $\gamma_0^{(i)}$ and $\gamma_0^{(j)}$ is represented by the unitary transformation $U_{ij} = \exp\left(-(\pi/4)\gamma_0^{(i)}\gamma_0^{(j)}\right)$ [15]. Furthermore, these Majorana zero energy modes are "protected", i.e. they cannot be pushed out of the energy gap, as guaranteed by the difference in topology between the p-wave wire and the vacuum.

For a system with N isolated Majorana sites, the ground state degeneracy is $2^{\frac{N}{2}}$, as two Majorana sites can either be filled or empty at a given time. One important feature of the degeneracy of the Majorana zero energy mode is that it is robust against local perturbations, as pairs of Majoranas are spatially separated. Energy splitting only happens when the wavefunctions of two Majoranas overlap. Furthermore, the splitting falls off exponentially as $e^{-r/\xi}$, where ξ is the microscopic coherence length in the system. The overlap of Majorana zero modes can be controlled and the resulting energy splitting has been measured in experiments [1].

For a system in which the Majoranas are sufficiently far apart, the robustness of the ground state degeneracy forms the basis for topological protection in quantum computing. Consider a series of adiabatic operations on Majorana modes, which are slow compared with finite-energy excitations in the system, but faster than the exponentially small energy splittings of the Majorana fermions. Such adiabatic operations are then equivalent to performing a unitary transformation on the original Hilbert space consisting of N low energy Majoranas. For a 2D system in which only the site positions of Majoranas are exchanged, the final state would not depend on the exact path of motion undergone by the Majoranas, but only on the topology of the operation, i.e. the order of the

braiding. As a result, the braiding operations are said to be "topologically protected".

Although qubits formed from pairs of Majoranas are insufficient for universal quantum computing and non-topological processes are required, a combination of other anyonic species are capable of achieving universal quantum computing.

True spinless 1D wires do not exist in reality. However, the "fermion doubling theorem" can be overcome by combining a semiconducting nanowire with strong spin-orbit effect, superconducting proximity effect, and a small magnetic field. Experimental evidence of Majorana zero modes on nanowire systems has been observed across different research groups [1,8,25]. Majorana zero modes were also observed in other systems, such as atomic chains on a superconducting substrate [26], topological insulators coupled to a superconductor [31,44,6]. In addition, 5/2 fractional Quantum Hall state is also a candidate system that hosts Majorana zero modes [24].

1.4.2 Proximitized Quantum spin Hall edge states

In order to engineer Majorana fermions, besides proximitizing semiconducting nanowires, one can alternatively utilize the 1D edge states that reside on the edge of 2D material platforms, namely the quantum spin Hall or quantum Hall systems. The overarching idea is very similar to the nanowire approach: by introducing superconductivity via proximity effect where only a single band crosses the Fermi energy, p-wave pairing could be produced.

Proximity effect

When a normal metal is well contacted to a superconductor, the Cooper pairs from the superconductor diffuse into the normal metal, which makes the normal metal weakly superconducting. This effect is called *proximity effect* [37]. At the same time, the order parameter of the superconductor near the normal-superconductor (NS) interface also decreases due to the "inverse proximity effect", as

shown in Fig. 1.6[21].

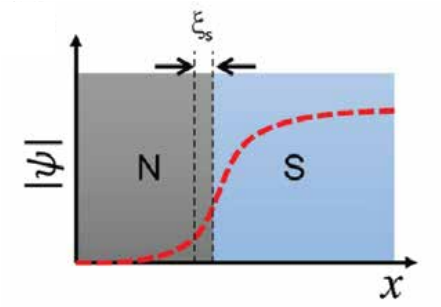

Figure 1.6: The superconducting order parameter $|\Psi|$ at the normal-superconductor (NS) interface. ξ_s is the superconducting coherence length. Figure adapted from Lee, 2018[21].

In the ballistic regime,

$$\xi_{b,T=0} = \frac{\hbar v_F}{2\Delta}, \tag{1.22}$$

where v_F is the Fermi velocity in the normal region.

In the diffusive regime,

$$\xi_{d,T=0} = \sqrt{\frac{\hbar D}{2\Delta}}, \tag{1.23}$$

where D is the diffusion constant in the normal region. For 2D systems, $D = v_F l_{\mathrm{MFP}}/2$, and for 3D systems, $D = v_F l_{\mathrm{MFP}}/3$, where l_{MFP} is the mean free path of charge carriers.

A proximity Josephson junction can be formed by placing a superconductor on both sides of the normal metal, separated by a distance smaller than the superconducting coherence length ξ_s.

The proximity effect can also be understood with a microscopic description of the Andreev reflection, which is a phenomenon at the NS interface, whereby an incident electron of an energy below the quasiparticle energy gap gets reflected as a hole back into the normal region. As a result, two electrons are injected into the superconductor as a Cooper pair.

One can write down a wavefunction that captures the processes happening at an NS interface:

$$\psi_E(x) = \left[A_E \begin{pmatrix} 1 \\ 0 \end{pmatrix} \exp\left(ik_c^N x\right) + B_E \begin{pmatrix} 1 \\ 0 \end{pmatrix} \exp\left(-ik_c^N x\right) + C_E \begin{pmatrix} 0 \\ 1 \end{pmatrix} \exp\left(ik_h^N x\right) \right] \theta(-x) + \left[D_E \begin{pmatrix} u_e \\ v_e \end{pmatrix} \exp\left(ik_e x\right) + F_E \begin{pmatrix} u_h \\ v_h \end{pmatrix} \exp\left(-ik_h x\right) \right] \theta(x), \tag{1.24}$$

where parameters A through F account for the right and left moving electrons and holes, capturing various processes at the NS interface. These processes include Andreev reflection (incident electrons reflected as holes of the opposite momentum, resulting in a cooper pair entering the superconductor), normal (specular) reflection (incident electrons reflected as electrons with the opposite momentum without entering the superconductor), as well as co-tunneling (two uncorrelated electrons tunneling into the superconductor together) The amplitudes can be solved by using the continuity equations at the NS interface.

Another related process to consider is the crossed Andreev reflection, which happens when a narrow superconductor (compared with the coherence length ξ) is sandwiched between two normal metals. If the superconductor is held at a lower potential with respect to one of the normal regions, a reflected hole can continue into the normal region on the opposite side of the superconductor (crossed Andreev reflection), instead of being reflected back into the normal region of the incident electron (Andreev reflection). Assuming for simplicity that the incident electron onto the NS interface has a positive energy, and that superconductor is grounded, the crossed Andreev reflected hole will have a negative energy, measurable as a negative potential. More specifically, Andreev reflection is also referred to as "local Andreev reflection" and considered a "local process", while crossed Andreev reflection is considered a "non-local process".

PROXIMITY EFFECT IN A 1D WIRE

For a 1D wire and a conventional bulk s-wave superconductor, we have

$$H_{1D} = \int \frac{dk}{2\pi} \psi_k^\dagger \mathcal{H}_k \psi_k, \tag{1.25}$$

$$H_{SC} = \int \frac{d^3\mathbf{k}}{(2\pi)^3} [\varepsilon_{sc}(\mathbf{k}) \eta_{\mathbf{k}}^\dagger \eta_{\mathbf{k}} + \Delta_{sc}(\eta_{\uparrow\mathbf{k}} \eta_{\downarrow-\mathbf{k}} + \text{H.c.})], \tag{1.26}$$

where $\varepsilon_{sc}(\mathbf{k}) = \mathbf{k}^2/2m_{sc} - \mu_{sc}$.

In addition, there is also a single-electron tunneling term,

$$H_T = -T \int dx \, [\psi_x^\dagger \eta(x, 0, 0) + \text{H.c}\,], \tag{1.27}$$

where T is the tunneling amplitude with units of energy $\times$ length. The Hamiltonian for the entire system is

$$H = H_{1D} + H_{SC} + H_T. \tag{1.28}$$

Following the argument outlined by Alicea, 2012 [2], if the Fermi wavevector of K_F^{sc} greatly exceeds that of the 1D system such that $Tk_F^{sc} \ll \Delta_{sc}$, the hybridization between the 1D wire and the superconductor primarily depends on the properties of the superconductor and tunneling T. Treating H_T as a perturbation, one can derive an effective Hamiltonian for the 1D system:

$$H_{eff} = H_{1D} + H_\Delta, \tag{1.29}$$

$$H_\Delta = \Delta \int dx \left(\psi_{\uparrow x} \psi_{\downarrow x} + \text{H.c.} \right). \tag{1.30}$$

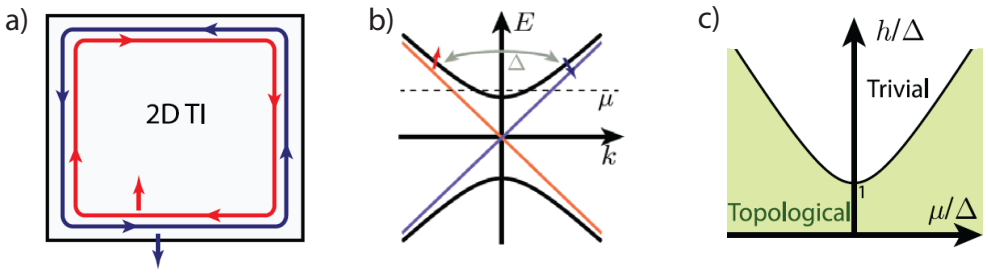

Figure 1.7: **a**, Counter-propagating edges with opposite spins in a 2DTI. **b**, Blue and red: dispersion without Zeeman field; black: a gap opens at $k = 0$ in a finite Zeeman field; grey: Intra-band pairing is p-wave like. **c**, Phase diagram illustrating the trivial and topological phase in a proximitized 2DTI system. Note that the system is always topological in the absence of any Zeeman field. Figures adapted from Alicea, 2012[2].

Topological superconductivity in quantum spin Hall systems

For a quantum spin Hall system (2DTI) as shown in Fig. 1.7a,

$$H = H_{\text{2DTI}} + H_{\Delta}, \tag{1.31}$$

$$H_{\text{2DTI}} = \int \mathrm{d}x \psi^{\dagger}(-iv\partial_x \sigma^z - \mu)\psi, \tag{1.32}$$

$$H_{\Delta} = \int \mathrm{d}x \Delta(\psi_{\uparrow}\psi_{\downarrow} + \text{H.c.}). \tag{1.33}$$

Introducing a Zeeman term,

$$H_{\text{Z}} = -b \int \mathrm{d}x \psi^{\dagger}\sigma^x \psi, \qquad b \geqslant 0, \tag{1.34}$$

where b is the dimensionless magnetic field, we have

$$H' = H_{\text{2DTI}} + H_{\text{Z}} + H_{\Delta}. \tag{1.35}$$

For $\Delta = 0$, the energy spectrum is $\varepsilon_{\pm}(k) = -\mu \pm \sqrt{(vk)^2 + b^2}$, as shown in Fig. 1.7. The gap opening at $k = 0$ is simply a result of time-reversal symmetry breaking in a finite magnetic field.

Using the basis of $\psi_{\pm}^{\dagger}(k)$, which are operators that create electrons with energy $\varepsilon_{\pm}(k)$, H' can be expressed as

$$\begin{aligned} H' = \int \frac{\mathrm{d}k}{2\pi} \Big\{ & \varepsilon_{+}(k)\psi_{+}^{\dagger}(k)\psi_{+}(k) + \varepsilon_{-}(k)\psi_{-}^{\dagger}(k)\psi_{-}(k) \\ & + \frac{\Delta_{\mathrm{p}}(k)}{2} \left[\psi_{+}(-k)\psi_{+}(k) + \psi_{-}(-k)\psi_{-}(k) + \mathrm{H.c.}\right] \\ & + \Delta_{\mathrm{s}}(k) \left[\psi_{-}(-k)\psi_{+}(k) + \mathrm{H.c.}\right] \Big\}, \end{aligned} \tag{1.36}$$

where the pairing terms Δ_p and Δ_s are

$$\Delta_p(k) = \frac{vk\Delta}{\sqrt{(vk)^2 + h^2}}, \tag{1.37}$$

$$\Delta_{\mathrm{s}}(k) = \frac{h\Delta}{\sqrt{(vk)^2 + h^2}}. \tag{1.38}$$

We can see that both *s*-wave and *p*-wave pairing terms emerge from the effective Hamiltonian in the $\psi_{\pm}$ basis. Inter-band pairing between the upper and lower bands ψ_{-} and ψ_{+} is of *s*-wave nature, whereas intra-band pairing is characterized by a *p*-wave term (Fig. 1.7b). Whether we have an effective *p*-wave pairing would depend on the competition between the *s*-wave and *p*-wave terms, which in turn depends on relative strength of the Zeeman field and the size of the superconducting gap (order parameter) in the parent bulk *s*-wave superconductor. In the case of a very large Zeeman energy h, the upper and lower energy band in Fig. 1.7b will be completely spin polarized and the resulting system would be a trivial insulator. It turns out that in the 2DTI case, as long as h is not too large and the Fermi energy does not lie in the Zeeman gap, we would end up with a 1D topological superconducting state.

More quantitatively, the eigenenergies of the 2DTI-superconductor system (Eq. 1.36) are

$$E'_{\pm}(k) = \sqrt{\Delta^2 + \frac{\varepsilon_{+}^2 + \varepsilon_{-}^2}{2} \pm (\varepsilon_{+} - \varepsilon_{-}) \sqrt{\Delta_{\mathrm{s}}^2 + \mu^2}}. \tag{1.39}$$

The quasiparticle gap as described in Eq. 1.36 vanishes only when $b^2 = \Delta^2 + \mu^2$, where the gap closes at $k = 0$. Consequently, $b < \sqrt{\Delta^2 + \mu^2}$ and $b \geqslant \sqrt{\Delta^2 + \mu^2}$ must be two topologically distinct areas. As argued above, the limit of large b ($b \gg \Delta$) is topologically trivial, so we must have $b < \sqrt{\Delta^2 + \mu^2}$ being the topological phase as in Fig. 1.7c.

1.4.3 Proximity effect in $\nu = 1$ integer quantum Hall states

Similar arguments made in the case of quantum spin Hall (2DTI) systems can be adapted to the $\nu = 1$ integer quantum Hall case, with a few assumptions:

1. The counter-propagating quantum Hall edge states are in close proximity with the bulk superconductor (within its superconducting coherence length);

2. The bulk superconductor has a large spin-orbit coupling, consequently, spin is not a good quantum number;

3. The energy gap between $\nu = 1$ and $\nu = 2$ is large ($E_{\text{gap}} \gg vk - \mu$).

Similar to a 2DTI,

$$\mathcal{H}_{\nu=1} = \mathcal{H}_k + \mathcal{H}_\Delta. \tag{1.40}$$

Writing it in the basis of $\Psi = (\psi_{1\uparrow} \quad \psi_{1\downarrow} \quad \psi_{2\uparrow} \quad \psi_{2\downarrow})^{\mathrm{T}}$ (see Fig. 1.8),

$$\mathcal{H}_k = \begin{pmatrix} vk - \mu & i\alpha k & 0 & 0 \\ -i\alpha k & E_{\text{gap}} & 0 & 0 \\ 0 & 0 & -vk - \mu & i\alpha k \\ 0 & 0 & -i\alpha k & E_{\text{gap}} \end{pmatrix}, \tag{1.41}$$

with H_Δ having its usual form of $H_\Delta = \Delta\psi_{1\uparrow}(k)\psi_{2\uparrow}(-k) + \Delta\psi_{1\downarrow}(k)\psi_{2\uparrow}(-k) + \text{H.c.}$.

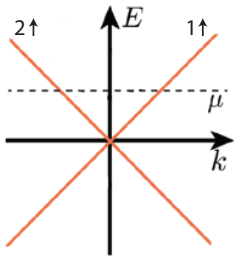

Figure 1.8: Dispersion relations of spin-polarized $\nu = 1$ integer quantum Hall states from two opposite edges of a sample. Band labelled with 1 and 2 correspond to ψ_1 and ψ_2 in spinor Ψ. A small spin-orbit coupling can be induced by contacting it with a superconductor with a large spin-orbit coupling term.

Treating the spin-orbit coupling $\alpha k \sigma^y$ in the proximitized quantum Hall states as a perturbation, $\mathcal{H}$ can be diagonalized:

$$\begin{aligned}
\left|\psi_{1+}\right\rangle &= \left|\psi_{1\uparrow}\right\rangle + \frac{\left\langle\psi_{1\perp}\left|\mathcal{H}'\right|\psi_{1\uparrow}\right\rangle}{E_{1\uparrow}-E_{1\downarrow}}\left|\psi_{1\downarrow}\right\rangle \\
&= \left|\psi_{1\uparrow}\right\rangle + \frac{i\alpha k}{E_z-(vk-\mu)}\left|\psi_{1\downarrow}\right\rangle \\
\left|\psi_{1-}\right\rangle &= \left|\psi_{1\downarrow}\right\rangle + \frac{i\alpha k}{E_z-(vk-\mu)}\left|\psi_{1\uparrow}\right\rangle \\
\left|\psi_{2+}\right\rangle &= \left|\psi_{2\uparrow}\right\rangle + \frac{i\alpha k}{E_z+(vk+\mu)}\left|\psi_{2\downarrow}\right\rangle \\
\left|\psi_{2-}\right\rangle &= \left|\psi_{2\downarrow}\right\rangle + \frac{i\alpha k}{E_z+(vk+\mu)}\left|\psi_{2\uparrow}\right\rangle
\end{aligned} \tag{1.42}$$

In this new basis and dropping higher order terms, the s-wave pairing terms in H_Δ become

$$\begin{aligned}
&\Delta\psi_{1\uparrow}(k)\psi_{2\downarrow}(-k) \\
\simeq\ &-\Delta_p\left(\psi_{1+}(k)\psi_{2+}(-k)+\psi_{1-}(k)\psi_{2-}(-k)\right)+\Delta\psi_{1+}(k)\psi_{2-}(-k),
\end{aligned} \tag{1.43}$$

$$\begin{aligned}
&\Delta\psi_{1\downarrow}(k)\psi_{2\uparrow}(-k) \\
\simeq\ &-\Delta_p\left(\psi_{1+}(k)\psi_{2+}(-k)+\psi_{1-}(k)\psi_{2-}(-k)\right)+\Delta\psi_{1-}(k)\psi_{2+}(-k),
\end{aligned} \tag{1.44}$$

where again a p-wave pairing term emerges.

$$\Delta_p \simeq -\frac{i\alpha k}{E_z}\Delta. \tag{1.45}$$

Experimentally, the counter propagating states would have to come from edges of two separate pieces of graphene, either stacked vertically with opposite doping on each layer, or separated with a narrow superconductor in between in a planar geometry. However, the induced spin-orbit coupling[40] acts to tilt the spins in the spin-polarized $\nu = 1$ edges, and if there is significant induced superconductivity in the $\nu = 1$ quantum Hall states, it would result in a 1D topological superconductor. The experiments presented in Chapter 3 and Chapter 6 are examples of devices made to investigate this effect.

1.4.4 Majorana modes in 2D system

We have discussed the creation of a superconducting 1D wire from coupling the edge states in a 2D system with a bulk superconductor. However, in order to generate localized Majorana zero modes, a domain wall needs to be created between the induced 1D topological superconductor and a topologically trivial region. Possible methods include using a ferromagnetic insulator or a gate to gap out part of the quantum spin Hall edge states[2], or selectively driving supercurrent near the edge of the sample[33]. For graphene-superconductor hybrid devices that will be discussed in this dissertation, the trivial phase is the incompressible bulk states at inner end of the superconducting fingers, as a natural consequence of the quantum Hall effect.

One advantage of creating Majorana fermions in 2D systems over nanowires is that the same experimental setup could be easily extended to create parafermions by driving the sample into some fractional quantum Hall states[3]. Consequently, one could possibly realize universal quantum computing on these systems.

1.5 Experimental detection of Majorana fermions

The two main ways for identifying zero energy Majorana modes include the measurement of a zero-bias tunneling peak, and the 4π-Josephson junction effect. However, as these effects can also be caused by a number of factors other than topological superconductivity and Majorana zero modes, caution has to be exercised in interpreting the results.

1.5.1 Tunneling to the end of a topological superconducting wire

The zero energy Majorana mode pair at the end of a 2D wire can either be occupied or unoccupied by a single fermion, resulting in a non-zero differential conductance when the Fermi level of the 1D wire is aligned with that of the normal lead. The electron that tunneled is subsequently Andreev reflected as a hole back into the normal lead, creating a Cooper pair. The tunneling process is shown in Fig. 1.9.

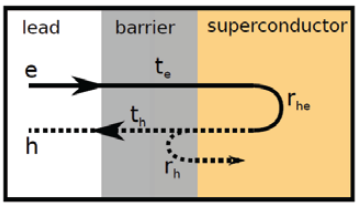

Figure 1.9: Tunneling between a normal lead and a superconductor. t's and r's are transmission coefficients and reflection coefficients respectively. Subscripts e and h refer to electrons and holes respectively. Figure adapted from von Oppen, 2017 [39].

The total amplitude of Andreev reflection can be calculated as a geometric sum [39],

$$A_{he} = t_h \left[1 + r_{he} r_e r_{eh} r_h + (r_{he} r_e r_{eh} r_h)^2 + \dots\right] r_{he} t_e = \frac{t_h r_{he} t_e}{1 - r_{he} r_e r_{eh} r_h}, \tag{1.46}$$

where the t's and r's are transmission and reflection coefficients respectively. Note that for an inci-

dent electron with energy below the superconducting gap, transmission t vanishes and the reflection r must be unitary

$$r = \begin{pmatrix} r_{ee} & r_{eh} \\ r_{he} & r_{hh} \end{pmatrix}. \tag{1.47}$$

Furthermore, particle-hole symmetry of the superconductor requires that

$$\tau_x r(-E)\tau_x = r^*(E), \tag{1.48}$$

or $r_{ee} = r^*_{hh}$ and $r_{eh} = r^*_{he}$, from which we conclude that $\det r(E = 0)$ is real. Since the determinant must also be unitary, we arrive at the conclusion that

$$\det r = \pm 1. \tag{1.49}$$

So a particular band falls into either of the two following cases:

1. $\det r = 1$: this corresponds to perfect normal reflection ($|r_{ee}| = 1$) and no Andreev reflection ($r_{eh} = 0$). This is the trivial phase.

2. $\det r = -1$: this corresponds to perfect Andreev reflection ($|r_{eh}| = 1$) and no normal reflection ($r_{ee} = 0$). This is the topological phase.

The tunneling current can be calculated by integrating over the the product of the Andreev reflection probability $|A_{he}|^2$ and the Fermi distribution of incoming electrons and outgoing holes $n_F(\omega - eV)[1 - n_F(\omega + eV)]$ as

$$I = \frac{1}{2} 2e \int \frac{d\omega}{2\pi\hbar} |A_{he}|^2 \left[n_F(\omega - eV) - n_F(\omega + eV) \right], \tag{1.50}$$

where V is the bias applied between the normal lead and the superconductor.

The differential conductance is

$$\frac{\mathrm{d}I}{\mathrm{d}V} = \frac{2e^2}{h}\frac{\Gamma^2}{eV^2 + \Gamma^2}, \tag{1.51}$$

where Γ is the tunneling rate, which is the same for electrons and holes at the Fermi level owing to particle-hole symmetry, $\Gamma = \Gamma_{e/h} = \frac{1}{2}\Delta t_{e/h}^2$.

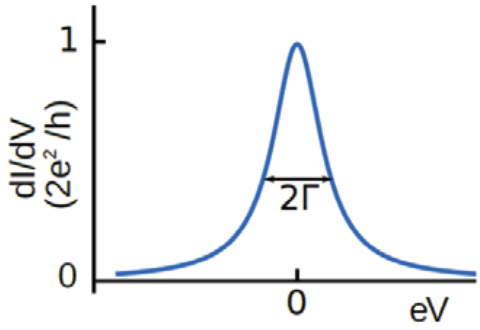

Figure 1.10: Quantized zero-bias conductance between a normal metal lead and a topological superconductor, adapted from von Oppen, 2017[39].

As shown in Fig. 1.10, the resulting differential conductance has a quantized height at $2e^2/h$ with the width of the peak determined by the rate of tunneling. The quantization of the conductance peak is a signature of tunneling through Majorana zero modes, which comes from perfect Andreev reflection. The other subgap states such as regular Andreev bound states result in peaks that are not quantized, with the resonance shift in energy as a function of magnetic field and gate voltage.

However, the quantized conductance is almost never observed in experiments. The first reason is that there is always temperature broadening. If the temperature exceeds broadening Γ, the width of the conductance peak will be determined by T, and the height of the conductance peak is reduced by a factor of order Γ/T. Second, finite temperature also causes inelastic quasiparticle transitions between the zero-energy state and other subgap states or the quasiparticle continuum, which destroys

the quantization and increases the broadening. This effect can be accounted for phenomenologically as

$$\frac{dI}{dV} = \frac{2e^2}{h} \frac{\Gamma^2}{eV^2 + \left(\Gamma + \Gamma_{qp}\right)^2}, \tag{1.52}$$

with an additional rate term Γ_{qp} that accounts for quasiparticle poisoning.

1.5.2 Josephson junction

4π current-phase relation

For a Josephson junction consisting of two 1D superconducting wires, the two Majorana bound states from the near ends of both wires overlap and fuse into a conventional fermion with non-zero energy. The resulting Josephson junction has a 4π current-phase relation. In contrast, in a conventional Josephson junction where supercurrent is carried though Andreev bound states, the current phase relationship exhibits a 2π-periodicity.

A simple way to see how the 4π-periodicity develops is to consider the tunneling Hamiltonian

$$H_T = t c_L^\dagger c_R + t^* c_R^\dagger c_L, \tag{1.53}$$

where c operators are annihilation operations of electrons at the junction in the left and right superconductor, and t is the tunneling matrix element. Using $c_L \simeq u_L \gamma_L$ and $c_R \simeq i u_R \gamma_R$, where $u_{L/R}$ are real Majorana wavefunctions in the left and right bank, H_T can be re-expressed as

$$H_T = \left(t + t^*\right) u_L u_R P, \tag{1.54}$$

where $P = i\gamma_L\gamma_R$ is the parity operator of the Majoranas. We can fix a gauge, such that for a phase difference φ across the junction, the tunneling t can be expressed as $t = t_0 e^{i\phi/2}$, and the subgap

energy spectrum is

$$E = \pm 2\cos(\phi/2)t_0 u_L u_R, \tag{1.55}$$

as shown in Fig. 1.11. The plus-minus branches in the energy corresponds to the parity eigenvalue ± 1. Although the entire spectrum including both fermion parity sectors are 2π periodic, the spectrum is 4π periodic for a fixed fermion parity, and the degeneracy at $\varphi = \pi$ is said to be protected by fermion parity.

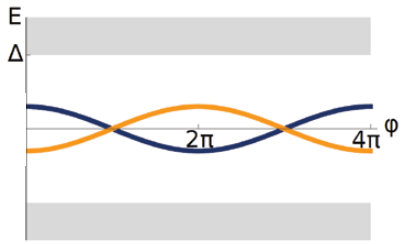

Figure 1.11: Subgap energy spectrum of a topological Josephson junction. The blue curve corresponds to a parity of 1 and orange a parity of -1. Each branch has a periodicity of 4π and the crossing is protected by parity conversation. Figure adapted from von Oppen, 2017[39].

From the dc Josephson junction effect,

$$I = 2e\frac{dE}{d\phi}, \tag{1.56}$$

we can see that the current is also 4π periodic for a given fermion parity.

Ac Josephson junction measurement

For a conventional Josephson junction with an applied voltage of the form

$$V = V_0 + V_1 \cos\omega_1 t, \tag{1.57}$$

the Josephson current is

$$I_J = I_c \sum_n (-1)^n J_n \left(2eV_1/\hbar\omega_1\right) \sin\left(\varphi_0 + \omega_0 t - n\omega_1 t\right), \tag{1.58}$$

where φ_0 is the initial phase difference at $t = 0$, $\omega_0 = 2eV_0/\hbar$ and J_n the nth Bessel function. Due to the oscillation of the Bessel function, each term in the summation is non-zero only when $V_0 = n\hbar\omega_1/2e$, at which the critical current experiences a jump. These voltage steps in an ac Josephson junction are also called Shapiro steps (Fig. 1.12b). With a 4π current-phase relation, the jump in the critical current happens at $V_0 = n\hbar\omega_1/e$, i.e. only at every second Shapiro step. Alternatively referred to as fractional ac Josephson junction effect, it has been observed in both superconducting nanowire Josephson junctions[32], and HgTe-based topological Josephson junctions[42] in Fig. 1.12.

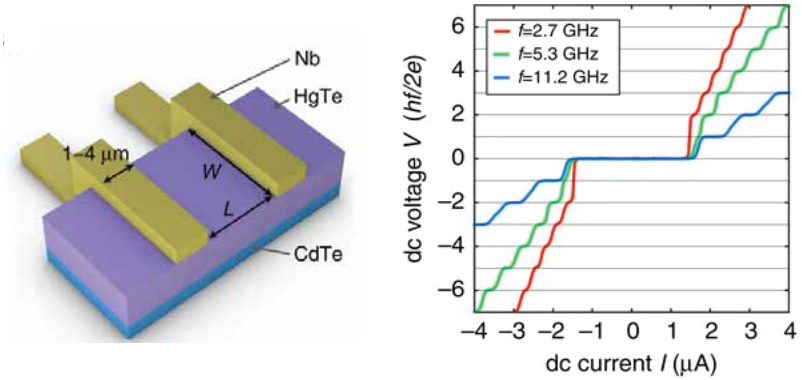

Figure 1.12: A HgTe based topological Josesphson junction device (left) and the Shapiro step measurement (right). The first Shapiro step became weaker and eventually disappeared with a decreasing frequency of the applied microwave. Figures adapted from Wiedemann, 2016[42].

In experiments, fermion parity is easily violated by quasiparticle poisoning if the phase of the junction is varied too slowly, or if there is Joule overheating[19], and the system reverts back to a conventional 2π-periodicity. By employing an ac voltage at microwave frequency in a measurement of Shapiro steps, the quasiparticle poisoning problem can be effectively minimized due to the fast-

varying phase.

There are no solutions. There are only trade-offs.

Thomas Sowell

2

Niobium nitride contact on graphene

2.1 General properties of niobium nitride (NbN)

Niobium nitride (NbN) is a type-II superconductor with a bulk critical temperature (T_c) ranging from 14 K to 16 K[7,34,45]. The critical temperature of a thin film of NbN is lower: for a NbN nanofinger about 100 nm wide, 1 μm to 1.5 μm long, and 70 nm thick that we successfully fabricated, the T_c was around 10 K. The upper critical field of NbN film is between 20 T and 30 T[35], well above the maximum magnetic field (8 T) applied in our experiments. The BCS coherence length for NbN, ξ_{BCS}, is given by $\xi_{\mathrm{BCS}} = \hbar v_{\mathrm{F}}/\pi\Delta \simeq 100$ nm ($v_{\mathrm{F}} \simeq 10^6$ m/s[23], $\Delta \simeq 2$ meV[20]). In a similar NbN-graphene system, ξ was estimated to be about 50 nm[20] from experiments. The high critical temperature and high critical field of NbN allow us to perform experiments to study simultaneously the superconductivity in NbN and well-developed quantum Hall states in graphene.

2.2 Making NbN-graphene contact

Before making NbN contact onto graphene, the hBN encapsulated graphene was etched with reactive ion etching (Appendix A) to expose fresh edges for contact. No graphene was left underneath the NbN, and NbN makes direct contact onto the edges of graphene. This allows maximal quasiparticle tunneling between NbN and quantum Hall edge states when the sample is placed in a perpendicular magnetic field.

The NbN superconducting contact consists of 5 nm of titanium (Ti) deposited by electron-beam evaporation, followed by 5 nm of niobium (Nb) and 55 nm to 75 nm of NbN deposited by sputtering. The electron-beam evaporator and the sputterer share the same chamber at a base pressure below 10^{-7} Torr. NbN was sputtered with reactive sputtering in an argon/nitrogen gas environment. The bottom Ti acts as a sticking layer, and Nb protects Ti from reactive nitrogen radicals during reactive sputtering of NbN.

2.3 Fabricating NbN nanostructures

In an earlier paper[20], coupling between quantum Hall edge states in graphene and NbN was measured through crossed Andreev reflection. For experiments in this dissertation, we would like to enhance the crossed Andreev reflection in hopes of creating Majorana zero modes. Thus, it would be ideal to make NbN fingers as narrow as possible without losing the superconductivity of NbN.

In search of optimal fabrication parameters, we fabricated and measured the T_c of NbN wires 5 μm long and of three different widths on a silicon substrate (Fig. 2.1d). As the width of the NbN finger increases, T_c also increases for all fabrication conditions. We also note that the narrowest NbN finger fabricated (design width: 80 nm) showed two different transition temperatures, which is due to the non-uniform width of the finger in actual devices fabricated.

Moreover, increasing the thickness of Ti from 5 nm in the standard recipe to 7 nm depressed T_c slightly due to a stronger inverse proximity effect induced by a thicker normal layer. On the other hand, heating from the atomic layer deposition (ALD) at 250°C did not degrade the quality of NbN significantly. However, it is unknown whether heating has a significant effect on the quality of graphene-NbN contact. As the quality of contact depends on the etch profile of graphene and sputtering condition, and could vary for two samples fabricated at the same time with exactly the same fabrication conditions.

We note that the widths of NbN reported here are design parameters rather than actual widths of the samples. It is common practice to slightly overdose during electron-beam lithography. As the interaction between the electrons from the electron-beam lithography and the sample varies from stack to stack and substrate to substrate, a design width of 75 nm to 80 nm usually yielded an actual width of 100 nm to 120 nm of sputtered NbN in an hBN encapsulated graphene device (see Fig. 3.1 of Chapter 3). The actual separation between graphene on either side of the NbN contact is likely smaller than the width of the NbN contact measured from a scanning tunneling electron (SEM)

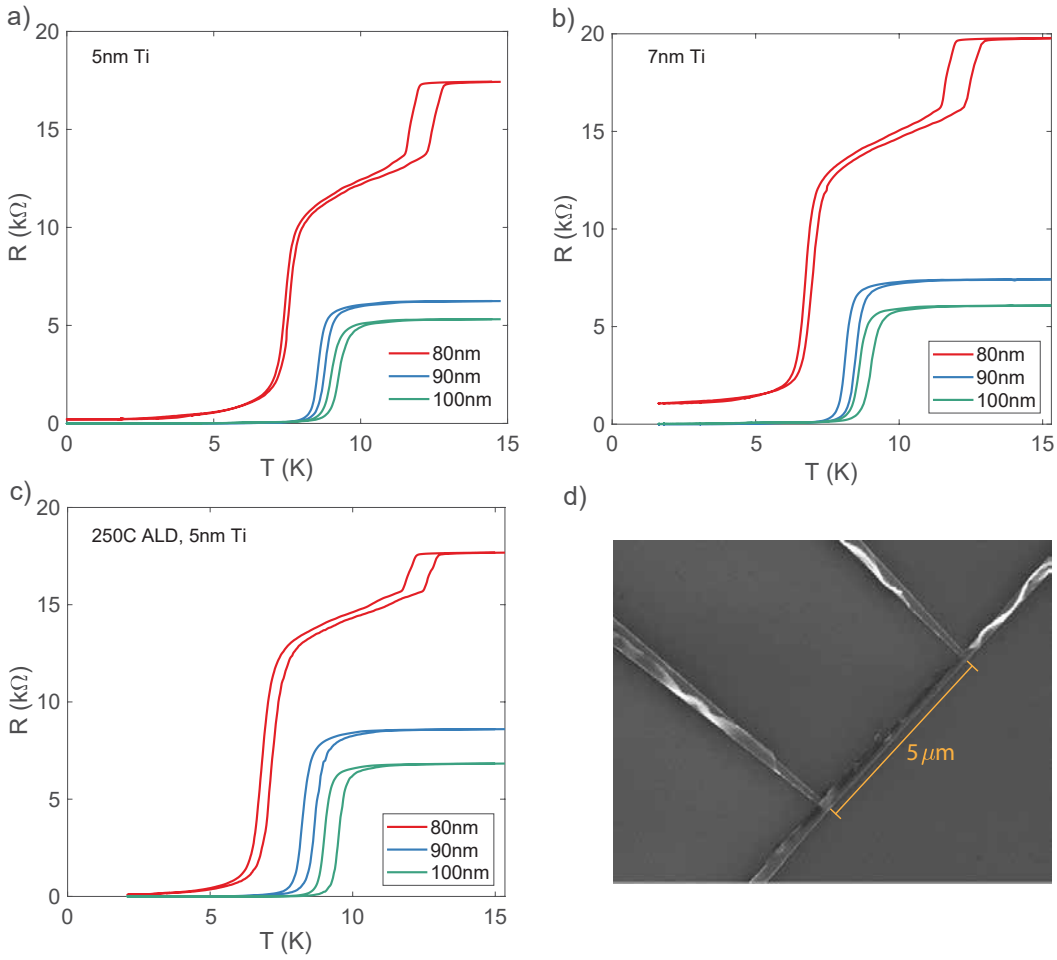

Figure 2.1: Resistance vs. temperature plots of 5 μm NbN fingers of different widths fabricated with **a**, The standard recipe with 5nm of Ti as the sticking layer. **b**, A slightly thicker 7 nm of Ti sticking layer. **c**, 5 nm of Ti but with NbN subjected to an atomic layer deposition (ALD) step at 250°C. Neither a thicker Ti layer nor an elevated temperature significantly altered the critical current for nominal (i.e. designed) widths of 90 nm and 100 nm. The narrowest finger (80 nm) exhibits two transitions, most likely due to the wire having non-uniform width along its length. Part of the wire had a width of even larger than 100 nm, as seen from the upper transition temperature, which was higher than both the 90 nm and 100 nm samples). **d**, A scanning electron microscope (SEM) image of one such test device.

image, due to an angled etch profile of the graphene stack (see Fig. 3.2 of Chapter 3).

In addition, the lengths of NbN fingers fabricated in graphene-NbN hybrid devices ranged from 1 μm to 1.5 μm, shorter than the length used (5 μm) in the test measurement. A less skewed aspect ratio would have mitigated the problem of having multiple critical temperatures due to non-uniform widths in a single NbN finger.

One common feature of sputtered NbN is the "bunny ears" (extra metal left on the substrate) from the lift-off process (Fig. 2.1d). Unlike evaporation which is directional, sputtering is an isotropic process and the materials get deposited on the side walls of the nanostructures. While it is very difficult, if not impossible, to completely eliminate "bunny ears" in these nanofinger structures, using a relatively thin layer of resist leaves less prominent bunny ears, albeit counter-intuitive at first. The sputtered NbN films are highly stressed, and lift-off happens as the NbN film releases the built-up stress and breaks at its thinnest point (i.e. the side walls of the resist). Therefore, having a thinner resist causes less NbN to be deposited on the side walls to begin with, and thus less leftover from lift-off. This is different from lift-off processes for deposition of metals by evaporation, where a thicker resist gives a cleaner lift-off.

2.4 Properties of NbN fingers

The NbN finger structures fabricated have a critical temperature between 8 K and 12 K, and remains fully superconducting at the maximum magnetic field (8 T) applied.

The quality of contact between NbN and graphene was characterized either through a local Andreev reflection over the normal-superconductor (NS) interface or a crossed Andreev reflection measurement in the quantum Hall regime, as shown in Fig. 2.2. As the NbN contact is grounded (energy = 0), in the case of a perfect Andreev reflection, the quantum Hall edge states of energy E must exit with an energy of $-E$ from the opposite side of NbN. This gives rise to a negative voltage

signal, which was measured in a previous experiment[20].

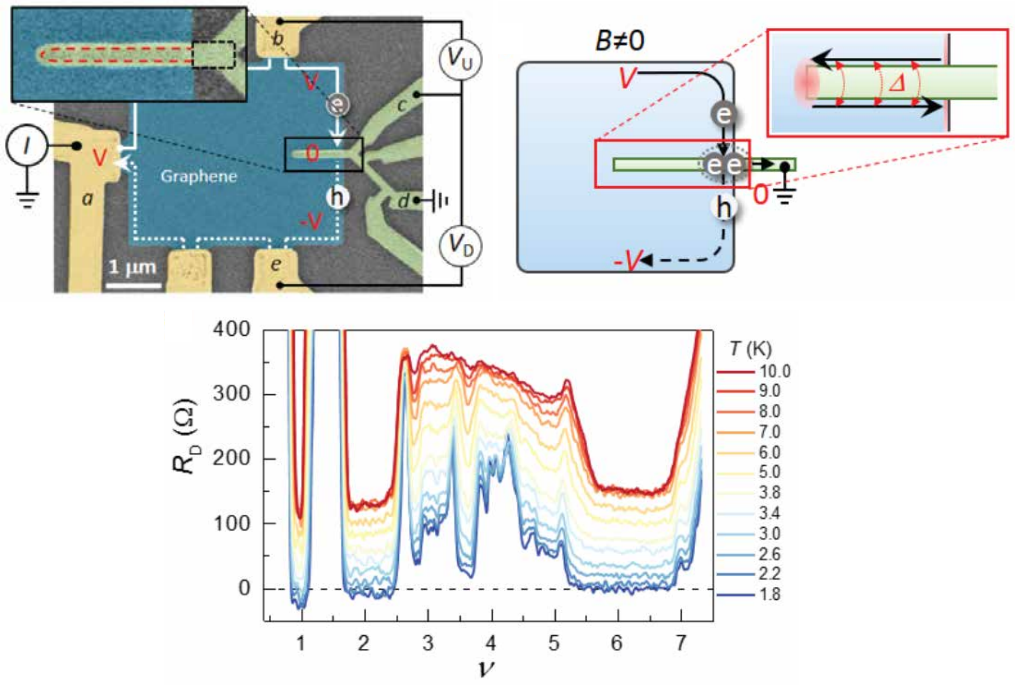

Figure 2.2: The quality of superconducting contact between NbN and quantum Hall edge states in graphene can be characterized through crossed Andreev reflection measurement. Upper panel: quantum Hall edge states with clockwise chirality enter the NbN finger contact at energy E, and some are crossed Andreev reflected to the lower section of graphene with energy $-E$. Lower panel: voltage V_D measured downstream (normalized by the total current) are negative for filling factors 1, 2 and 6 at low temperatures, consistent with crossed Andreev reflection happening at the N-S-N interface. Figures adapted from Lee, 2017[20].

Look up at the stars and not down at your feet. Try to make sense of what you see, and wonder about what makes the universe exist. Be curious.

Stephen Hawking

3

Narrow quantum Hall Josephson junctions

In order to further investigate the coupling between the quantum Hall edge states, Josephson junctions consisting of two copies of NbN fingers described in Chapter 2 were fabricated. The NbN fingers were placed as closely together as the fabrication would allow. Strong Josephson coupling was observed, and the critical current I_c was found to correlate with the bulk filling factors of graphene.

3.1 Device geometry

As the superconducting NbN finger electrodes are narrow (about 100 nm in width) compared with "wide" Josephson junctions (Chapter 4), we will refer to them as narrow junctions hereafter. Theoretical discussion in Chapter 1.3 and prior experiments [20] suggest that a Majorana zero mode is likely to emerge at each end of a single NbN finger. To minimize the wavefunction overlap of these Majorana fermions, the length of NbN fingers cannot be too short. However, it cannot be too long either, as it is extremely difficult to fabricate a thin and long NbN wire with uniform thickness. An uneven width of the NbN finger would give rise to a varying superconducting order parameter as shown in Fig. 2.1 and introduce complications into the measurement. Without any prior knowledge of the coherence length of the Majorana mode in graphene, we fabricated Josephson junctions with NbN fingers between 1 μm and 1.5 μm wide, and two of such junctions, narrow junctions 1 and 2, are shown in Fig. 3.1.

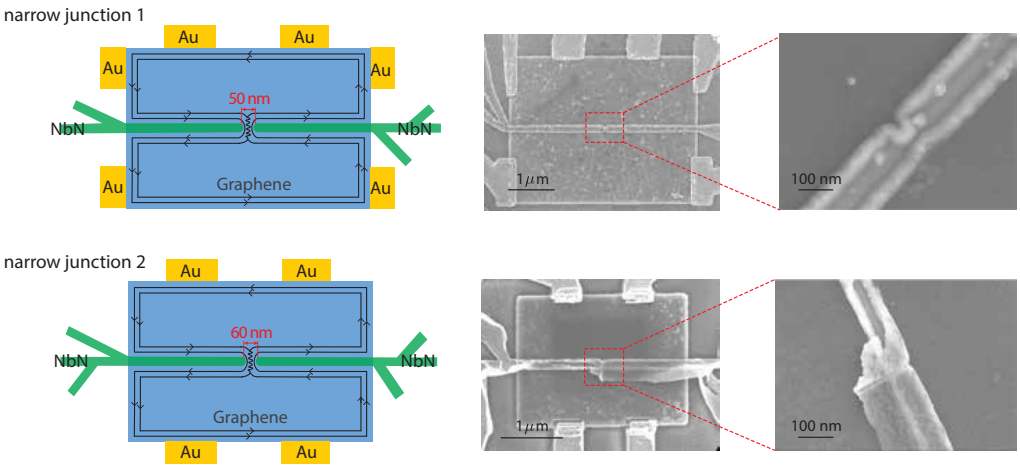

Figure 3.1: Upper panel: The schematic and scanning electron microscope (SEM) images of narrow junction 1 (3 μm by 3.6 μm). Lower panel: The schematic and SEM images of narrow junction 2 (2 μm by 2.8 μm). Multiple electrodes of both Au and NbN enable multi-terminal measurement of the quantum Hall effect in graphene and the Josephson junction effect. From the zoomed-in SEM image on the rightmost column of the figure, NbN leads are connected through a very narrow section of NbN for junction 1, and a few nanometer thick NbN film for junction 2. The width of the NbN fingers is about 100 nm for both junctions.

Another critical design parameter is the separation between the two NbN fingers. In order to realize a Majorana-mediated Josephson junction, the separation of the NbN fingers should be as small as possible to allow maximal overlap of the Majorana zero mode from each NbN electrodes. However, as the electron-beam lithography and the etching process have some degree of uncertainty, the separation was designed to be ranged from 50 nm to 70 nm.

Due to imperfect lift-off of the sputtered NbN as discussed in Chapter 2, the Josephson junctions were connected by a NbN weak link, in addition to graphene, as seen from the zoomed-in scanning electron microscope (SEM) images in Fig. 3.1. This additional weak link can be avoided by slightly increasing the separation between the NbN leads. However, for narrow Josephson junctions fabricated with a designed separation larger than 60 nm, we found either no Josephson coupling or a very weak one that quickly turned normal upon the application of a magnetic field, making it impossible for the observation of superconducting coupling of quantum Hall states.

As the unintended NbN left over from lift-off is extremely narrow or thin, it would have been very unlikely that it was exposed before the etch step such that the graphene underneath was etched away. Therefore, despite that the NbN electrodes are connected through a NbN weak link, there is still graphene underneath where the NbN weak link is due to the angled etch profile of the BN-graphene-BN stack as shown in Fig. 3.2. Detailed fabrication steps are outlined in Appendix A.

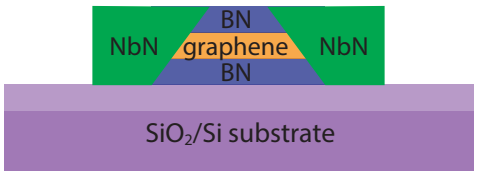

Figure 3.2: Cross section of the NbN-graphene-NbN Josephson junction. Due to the angled etch profile, there would still be unetched graphene connecting NbN electrodes, even though the NbN electrodes could be touching from a top-view SEM image.

3.2 Narrow Junctions at zero magnetic field

We confirm that graphene contributes to the total Josephson current, and that the partially connected NbN fingers indeed only form a weak link, by measuring the dependence of the critical current of the junction as a function of the carrier density in the graphene, in the absence of a magnetic field. If the Josephson junction were dominated by the NbN link (i.e. shorted), the critical current of the junction would not depend on the back gate. However, a gate dependence was observed, as shown in Fig. 3.3.

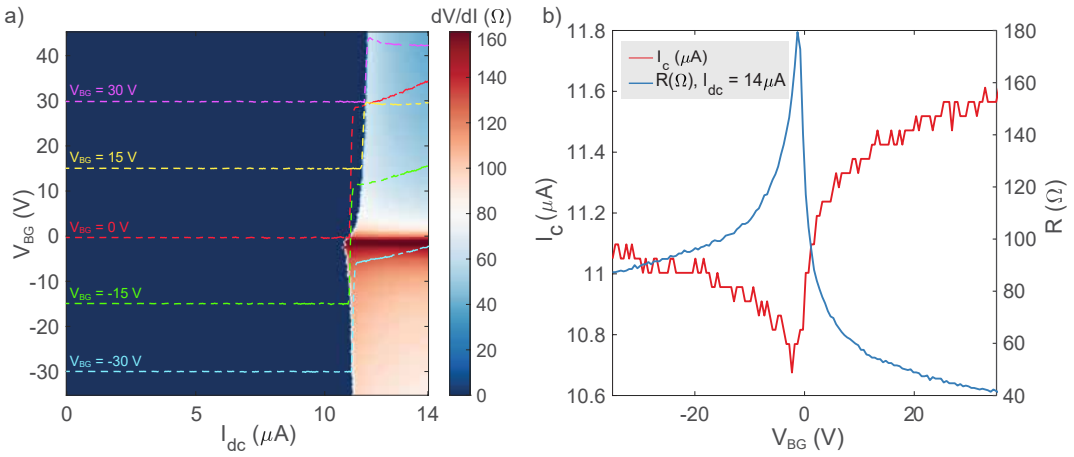

Figure 3.3: Narrow junction 1 at zero magnetic field and a temperature of 300 mK. **a**, Differential resistance across the junction as a function of dc current across the junction (I_{dc}), as well as the back gate (V_{BG}) of graphene. **b**, Critical current and junction resistance at a dc current of 14 μA. The critical current is suppressed at the Dirac point of graphene as one would expect.

A relatively large I_c of above 10 μA was seen for the entire gate range scanned in Fig. 3.3. We note that the weak dependence of the I_c on the back gate is within expectation, as the bulk of the Josephson current is carried through a small area of the graphene immediately adjacent to the NbN electrodes in the junction, and this area of graphene experiences Fermi-level pinning due to proximity to the NbN electrodes. This is consistent with the observation of a gate-independent component of the normal resistance, $R_{\text{n, direct}}$ (Section 3.4.5) and a corresponding gate-independent critical cur-

rent, $I_{c,\,\mathrm{direct}}$ (Section 5.2 of Chapter 5).

A rough estimate of the $I_c R_n$ product gives a value quite close to the gap of the NbN ($\sim$ 2 meV), indicating good coupling in the NbN-graphene-NbN junction. An alternative visualization of data presented in Fig. 3.3 as a function of the voltage bias across the junction can be found in Fig. C.2 of Appendix C.

Similar data were also measured in narrow junction 2 at 1.5 K (Fig. 3.4), and at 300 mK (Fig. 3.5). However, compared with a critical current of more than 14 μA in narrow junction 1, narrow junction 2 has a critical current of about 4 μA at zero magnetic field. In addition, outside of the first and the second transitions, which are the superconductor-normal transition of the Josephson junction and that of NbN respectively, a multitude of transitions were observed (Fig. 3.5). These transitions were also observed in other narrow Josephson junctions we fabricated, and are likely to be due to microscopic fluctuations in these NbN fingers due to their narrowness and the irregular geometry of the NbN thin film weak link.

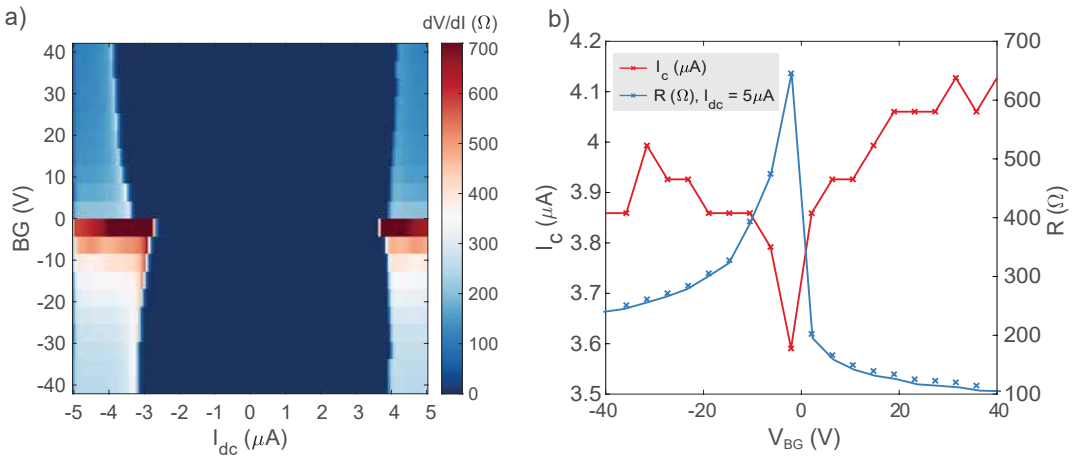

Figure 3.4: Narrow junction 2 at zero magnetic field and a temperature of 1.5 K. **a**, Differential resistance across the junction measured as a function of dc current (I_{dc}) across the junction, as well as the back gate (V_{BG}) of graphene. **b**, Critical current and the resistance across the junction at a dc current of 5 μA. The critical current is suppressed at the Dirac point of graphene.

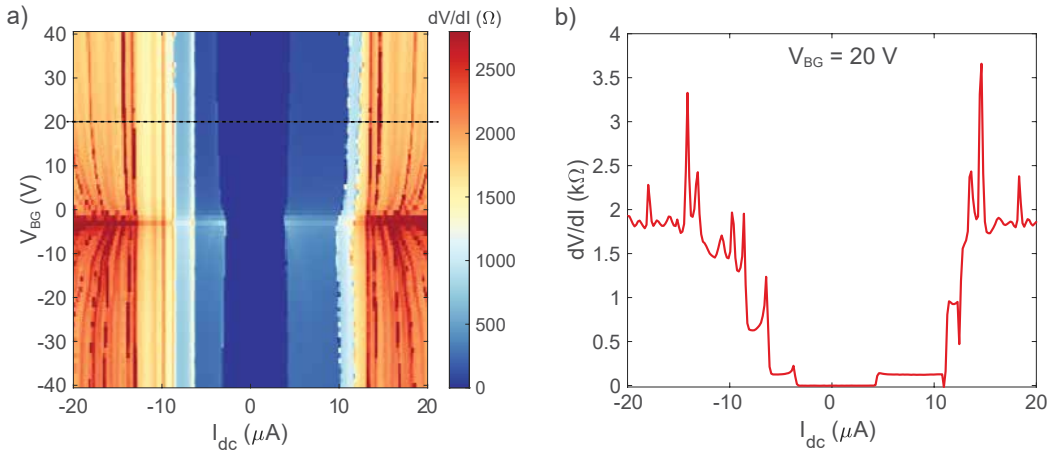

Figure 3.5: Narrow junction 2 at zero magnetic field and a temperature of 300 mK. **a**, Differential resistance across the junction measured as a function of dc current across the junction, as well as the back gate (V_{BG}) of graphene. **b**, Differential resistance of the junction at a back gate of 20 V, i.e. a horizontal line cut from **a**, showing multiple transitions above the critical current.

3.3 Narrow junctions in a finite magnetic field

3.3.1 Magnetic field dependence of I_c

The critical current I_c of narrow junction 1 decreases with an increasing magnetic field (Fig. 3.6). However, an I_c of above 6 μA was sustained even at a magnetic field of 8 T in narrow junction 1.

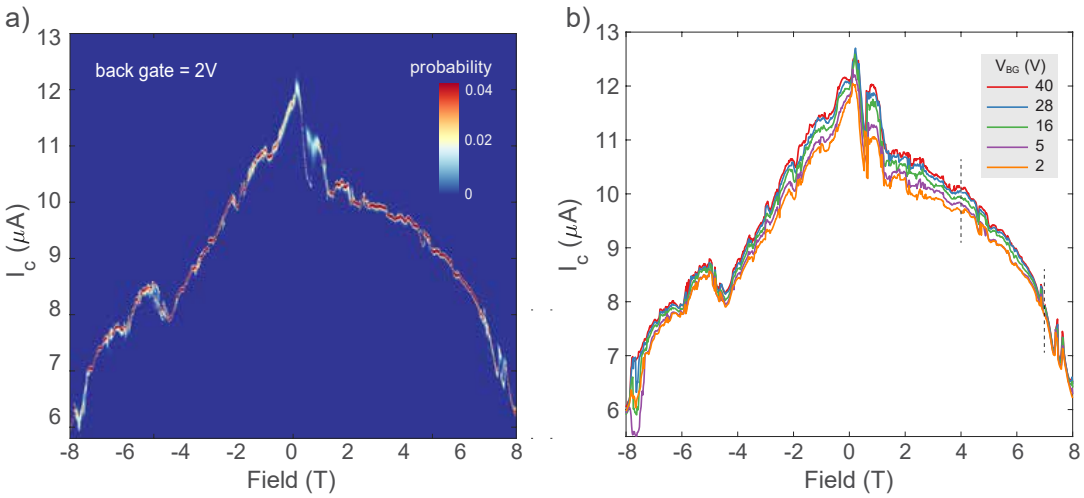

Figure 3.6: Magnetic field dependence of I_c for narrow junction 1 at different back gate voltages. **a**, The probability distribution of I_c (out of approximately 4500 dc measurements) at a back gate of 2 V with varying magnetic fields. **b**, The critical current I_c as a function of of the magnetic field at several back gate values.

The gate dependence of I_c becomes less significant at higher magnetic fields. For example,Ic for different gate values differ less at 7 T than at 3 T, as indicated by the vertical lines in Fig. 3.6b. This can be understood as follows. First, as the magnetic field increases, the superconducting order parameter of the NbN becomes smaller, and any change induced by other factors, such as carrier density of the normal region, becomes diminished. Second, if part of the Josephson current is mediated by quantum Hall edge states, the change in I_c would correlate directly with the filling factor of graphene at a constant magnetic field. As the magnetic field increases, the same increment of the back gate voltage leads to a smaller change in the filling factor, resulting in a smaller increment of I_c.

We defer a detailed discussion of the gate dependence of I_c to the next section.

Based on the SEM images, the junction area is about 3000 nm^2 (30 nm $\times$ 100 nm), which would in turn produce a Fraunhofer pattern with a periodicity of roughly 0.7 T. Although there is some hint of such an oscillation in Fig. 3.6, the absence of a clear interference pattern suggests that the current flowing through narrow junction 1 is highly non-uniform. Moreover, I_c is asymmetric with respect to a reversal in polarity of the magnetic field, possibly due to very strong vortex pinning in NbN fingers and an asymmetric spatial Josephson current density. On the other hand, the same measurement performed on narrow junction 2 shows a more symmetric I_c with respect to the magnetic field (Fig. 3.7a), resembling the Fraunhofer interference pattern for a conventional Josephson junction. We defer the discussion of this large scale critical current variation to Chapter 5.

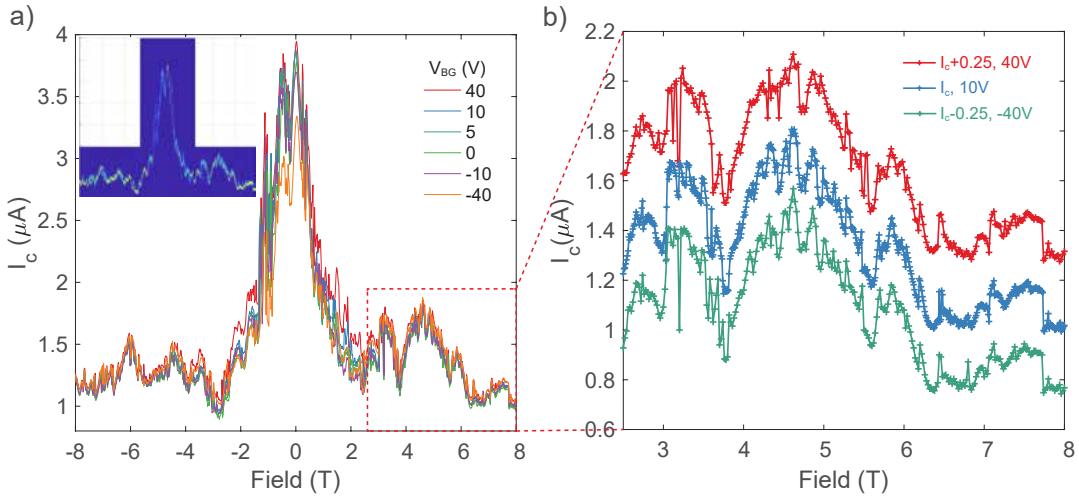

Figure 3.7: Magnetic field dependence of I_c at different back gate voltages for narrow junction 2. **a**, I_c at selected back gate voltages with varying magnetic fields. Inset: The probability distribution of I_c at a back gate of 5 V. **b**, A zoomed-in view of I_c at a back gate value of 40 V, 10 V and -40 V, showing identical fine-scale data modulations across different back gate values. These small modulations are robust and reproducible. For clarity, I_c is shifted up and down by 0.25 μA for data taken at 40 V and -40 V respectively.

We note that for each critical current measurement, the applied dc current was always swept from zero to a finite positive value, and that the magnetic field was swept from positive to negative

or from negative to positive values, for each back gate value. The absence of hysteresis suggests that any magnetic impurity present in the devices would have been frozen out at low magnetic fields and could not have caused the observed asymmetry. We also comment that changing the sample from the electron-doped regime to the hole-doped regime does not change the Fraunhofer pattern observed.

3.3.2 Gate dependence of I_c

At a given magnetic field, variations in the critical current are brought about by changes in the number of edge states present. Thus, we can remove the background contribution of I_c by subtracting the I_c measured around charge neutrality point of graphene from the total I_c measured. On the electron-doped side (40 V) shown in Fig. 3.8a, periodic modulations of I_c as a function of the magnetic field appear for magnetic fields larger than 4 T, with the height of each step being about 25 nA, as indicated with the vertical arrows. If the appearance of these steps are due to a change in filling factors at different back gate values, then one would expect to see the same steps appearing if the filling factor is tuned by sweeping the back gate at a constant magnetic field. This is indeed the case, and will be discussed in Section 3.4.

On the other hand, similar stepwise increment of I_c as a function of back gate is absent at a back gate of -40 V (Fig. 3.8b). This is not surprising due to the following two reasons: first, the graphene-NbN contact quality tends to drop when the graphene is hole-doped; second, the creation and annihilation of superconducting vortices in NbN, brought about by changing the external magnetic field, affect the I_c in an unpredictable manner.

A similar analysis was also done for narrow junction 1 and is included in Fig. C.4 of Appendix C.

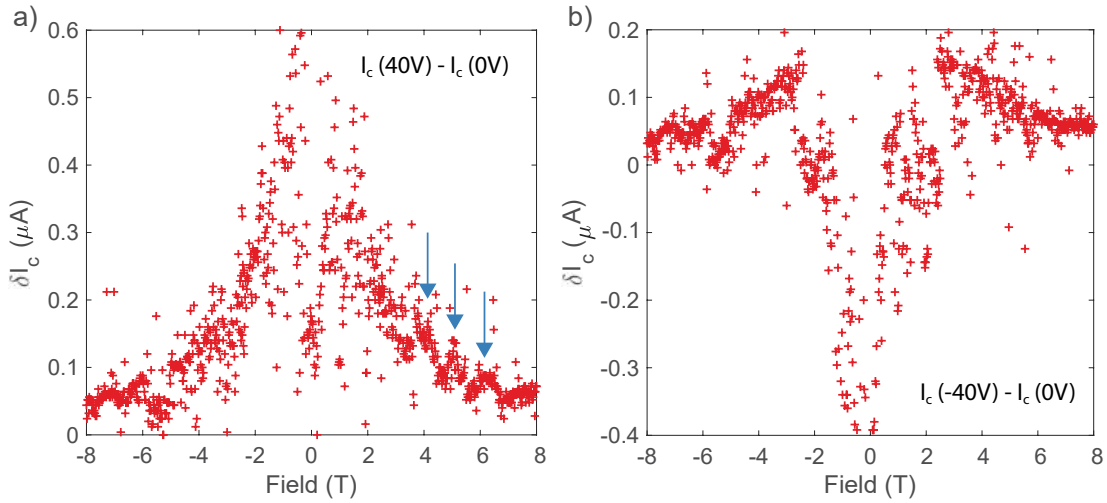

Figure 3.8: Magnetic field dependence of I_c with the $I_{c,Dirac}$ subtracted for narrow junction 2. **a**, I_c measured at a back gate of 40 V with I_c measured at 0 V subtracted. Periodic modulations of I_c emerge for positive magnetic fields, as indicated by the vertical arrows. **b**, I_c measured at a back gate of -40 V with I_c measured at 0 V subtracted.

3.4 Quantum Hall states and the critical current I_c

In this section, we will discuss the interplay between quantum Hall edge states in graphene and superconductivity in NbN, in the presence of a magnetic field. As varying the magnetic field changes the vortex configuration in NbN finger contacts and induces large fluctuations in the Josephson junction, we varied quantum Hall states by changing the back gate while keeping the magnetic field constant.

3.4.1 Quantum Hall states in graphene

The quality of quantum Hall states in graphene was verified through both a 4-terminal measurement with only normal gold contacts, and through a 3-terminal measurement in which NbN is used as the current drain, similar to previous work from our group [20] (see Fig. 2.2). We observed well-developed conductance plateaus of broken symmetry quantum Hall states under magnetic fields

ranging from 4 T to 8 T in both of the narrow Josephson junction devices. In addition, narrow junction 1 (Fig. 3.9) showed better quantum Hall plateaus than narrow junction 2 (Fig. 3.10).

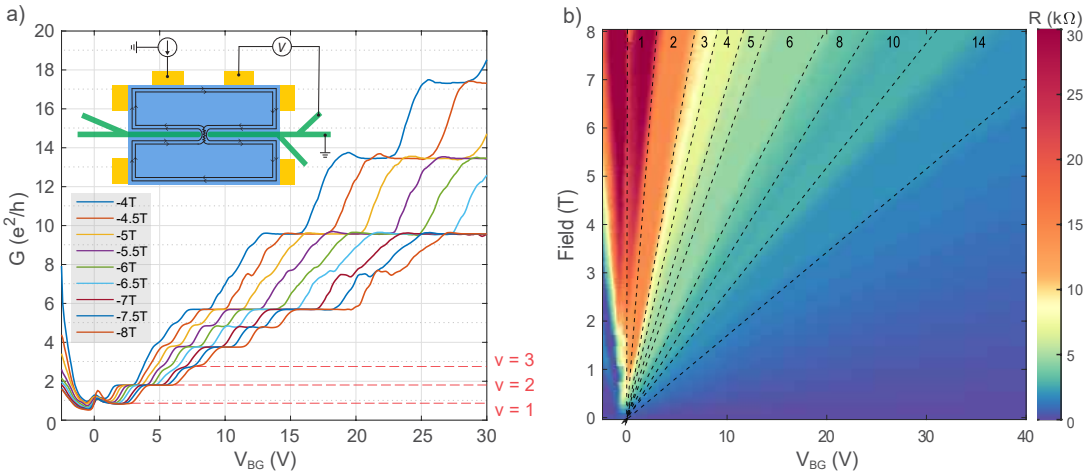

Figure 3.9: 3-terminal measurement of quantum Hall states of graphene in narrow junction 1 at 300 mK. **a**, Conductance in units of e^2/h, showing broken symmetry quantum Hall plateaus. **b**, A 2D plot of resistance as a function of both back gate and magnetic field, with the bulk filling factors of graphene labeled at the top.

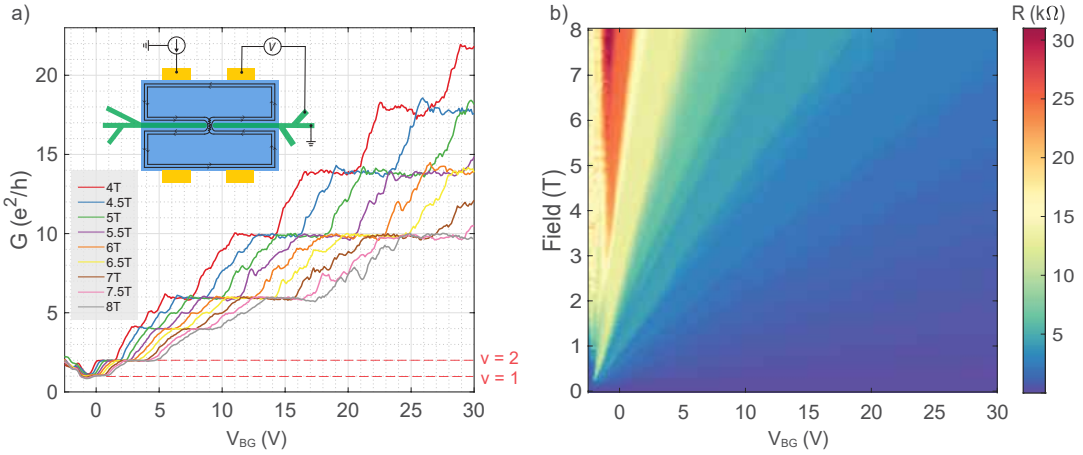

Figure 3.10: 3-terminal measurement of quantum Hall states of graphene in narrow junction 2 at 1.5 K. **a**, Conductance in units of e^2/h plotted as a function of back gate. **b**, A 2D plot of resistance as a function of both back gate and magnetic field.

3.4.2 Narrow junction 1: I_c as a function of graphene filling factor

When the critical current I_c was measured as a function of back gate voltage, I_c showed stepped features that were reminiscent of the conductance plateaus in a typical gate-dependent measurement at a fixed magnetic field. Fig. 3.11 shows the probability distributions of I_c over 5000 independent measurements, in which the plateaus can be observed clearly. A large number of measurements were made to maximize accuracy, minimizing fluctuations due to the stochastic nature of the critical current distribution.

In addition, I_c sometimes shows a bimodal (Fig. 3.11, 8 T) or a trimodal (Fig. 3.11, 7.1 T) distribution. The exact distribution is not only sample dependent, but also varies with the sweeping rate of the dc current source. Furthermore, vortices created in large magnetic fields also introduce more stochasticity in the switching current. Thus, in an attempt to make the comparison of I_c consistent across different magnetic fields and gate values, we computed the most probable I_c and identified it as the I_c for each back gate and magnetic field. The details of the measurement methodology can be found in Appendix B.

When the critical current is compared with the 3-terminal quantum Hall conductance measured with normal electrodes on the same plot, the one-to-one correlation between the plateaus measured in I_c and those in quantum Hall conductance becomes clear, as shown in Fig. 3.12.

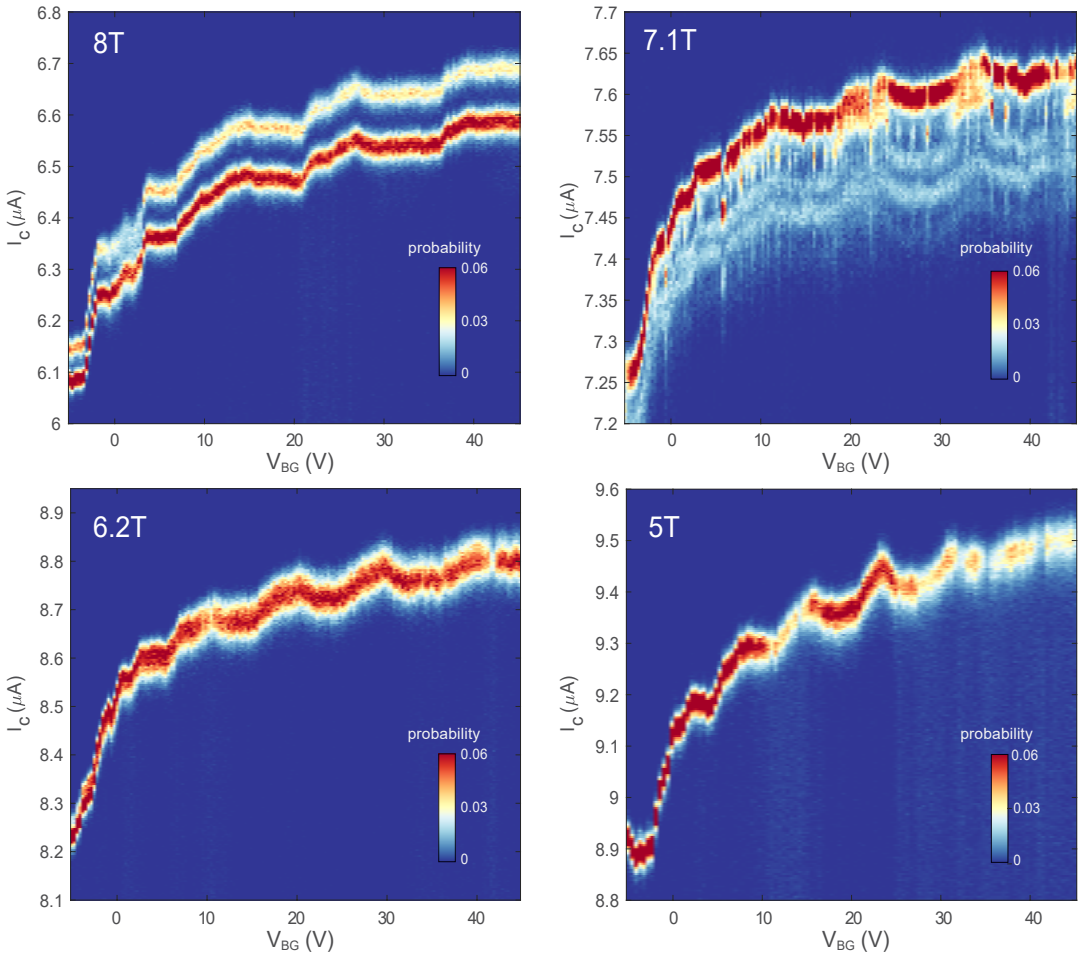

Figure 3.11: Probability distributions of critical current I_c versus back gate at several magnetic fields, showing steplike features that would normally appear in a quantum Hall conductance measurement.

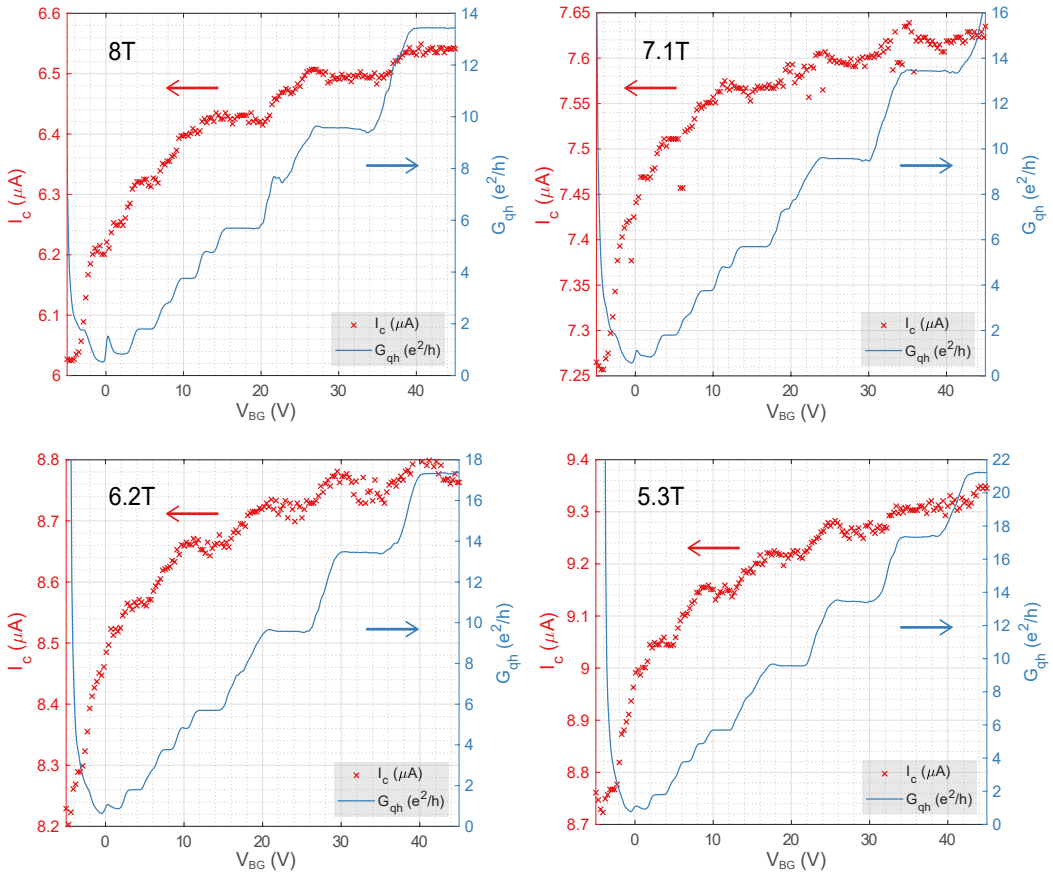

Figure 3.12: A direct comparison between the I_c of the Josephson junction (left axis, red curve) and quantum Hall conductance (right axis, blue curve), revealing that the steps in both the I_c and quantum hall conductance are of a similar origin.

We can further investigate the dependence of I_c on the bulk filling factor ν of graphene by examining I_c in the magnetic field-back gate phase space in Fig. 3.13a. This does not look like a typical quantum Hall fan diagram, because the measurement is dominated by large variation of I_c across different magnetic fields, resulting in the gate-dependent change of I_c at a particular magnetic field being overshadowed, as illustrated in Fig. 3.13d.

However, this relatively large baseline shift is not related to the quantum Hall effect. It can be seen by considering an infinitesimal change in magnetic field while holding the back gate constant (a vertical line cut in Fig. 3.13a), for which the number of quantum Hall edge states should remain the same. Therefore, the large shift in I_c across magnetic fields mainly come from the non-quantum Hall component of NbN-graphene-NbN junction, in which the supercurrent goes from one NbN contact to another via the small area of graphene sandwiched in between. In fact, as we will argue in Chapter 5.1, the background I_c is largely gate-independent and only provides an offset to the total I_c measured at a given magnetic field.

This non-quantum Hall contribution I_c can be read off from the I_c values at the charge neutrality point of graphene (-0.27 V for this sample) in Fig. 3.13b. Using $I_{c,Dirac}$ as a proxy for the background I_c, subtracting $I_{c,Dirac}$ from the corresponding total I_c at each magnetic field restores the familiar fan diagram of quantum Hall critical current $I_{c,qH}$ in Fig. 3.13c.

The I_c fan diagram can be alternatively visualized by adding an offset to I_c measured at different magnetic fields (Fig. 3.14, left). Moreover, the normal conductance G_n, measured at elevated temperatures, also exhibits a similar trend as expected (Fig. 3.14, right).

Besides tracking the evolution of $I_{c,qH}$ as a function of back gate at a constant magnetic field, one can also keep the back gate at a fixed value and investigate the dependence of $I_{c,qH}$ as a function of magnetic field, equivalent to taking a vertical slice in Fig. 3.13c. We defer a more detailed discussion to Chapter 5.

Figure 3.13 ***(following page)*****:** Critical current I_c at various back gate (V_{BG}) and magnetic field (Field) values for narrow junction 1. **a**, Measured critical current I_c as a function of back gate (x-axis) and magnetic field (y-axis). I_c decreases with magnetic field, and a fan diagram is barely visible. **b**, $I_{c,Dirac}$ at the Dirac point (filling factor $\nu = 0$) at each magnetic field. **c**, $I_{c,qH}$, the critical current after subtracting $I_{c,Dirac}$ from the measured critical current I_c. A fan diagram emerges with bulk filling factors of graphene ν identified. **d**, A comparison of the critical current I_c measured at several magnetic fields, showing the change in I_c going from one magnetic field to another.

Figure 3.13: (continued)

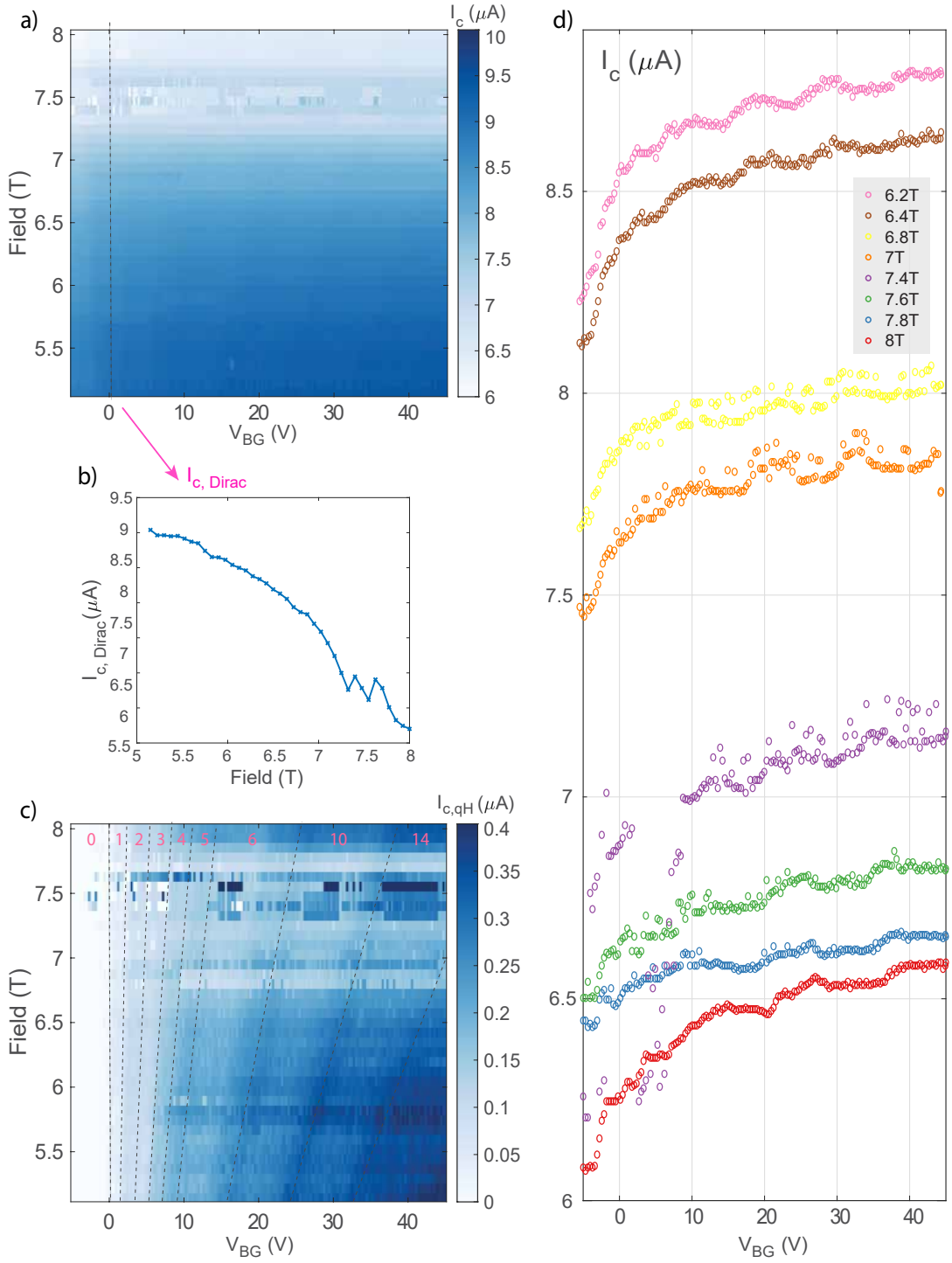

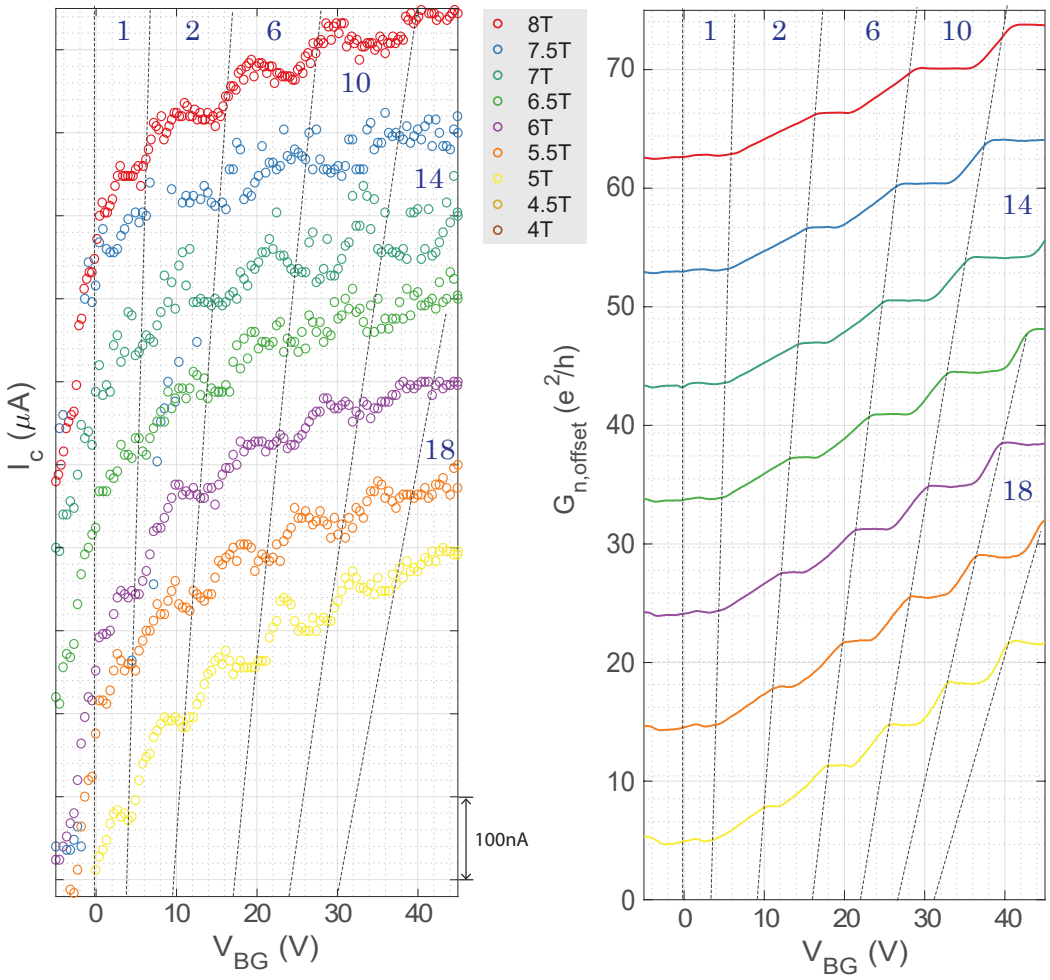

Figure 3.14: Critical current I_c (with an offset) and normal conductance G_n, with bulk filling factor ν labelled. Left: I_c with an offset of 100 nA for successive magnetic fields. Right: G_n with an offset of $10e^2/h$ for successive magnetic fields.

3.4.3 Narrow junction 2: I_c as a function of the filling factor

Although the overall amplitude of I_c for narrow junction 2 is much smaller than that for narrow junction 1, steps in I_c are clearly visible (Fig. 3.15). However, the sizes of the I_c steps are much smaller, and the steps due to broken-symmetry quantum Hall states could not be resolved.

I_c and the quantum Hall conductance G_{qH} of the sample are compared to confirm the correspondence between I_c and the quantum Hall states in the bulk (Fig. 3.16). Similar to narrow junction 2, both I_c and G_n develop quantum Hall-like steps, which correspond to filling factors of the bulk as shown in Fig. 3.17.

The two-dimensional plot of I_c versus the back gate and magnetic field in Fig. 3.18a, shows relatively large fluctuations in I_c as the field changes. I_c does not decrease monotonically, and reaches its highest value between a magnetic field of 6 T and 6.5 T as shown in Fig. 3.18b, if we track the change of the critical current at the Dirac point $I_{c,Dirac}$ with the magnetic field. This trend is reproducible across different rates and the direction of the magnetic field sweep, back gate values and the applied dc bias. However, the field at which the sample exhibits the maximum I_c shifts when the sample is thermal cycled, suggesting that the fluctuations and bumps in I_c as a function of magnetic field is related to vortex pinning in NbN.

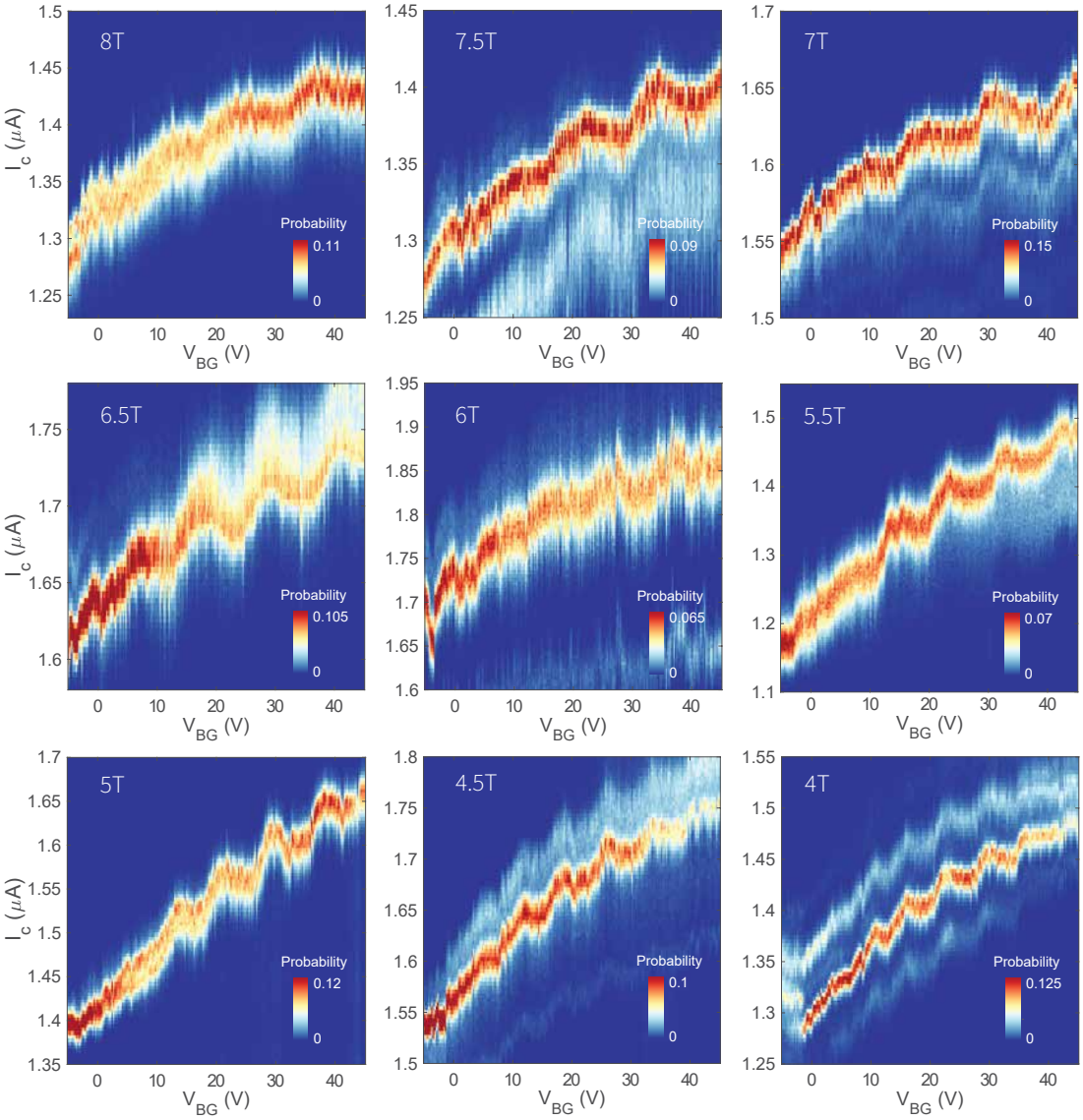

Figure 3.15: Probability distributions of I_c versus back gate at different magnetic fields for narrow junction 2. spin- and sublattice symmetry- degenerate Landau levels were observed.

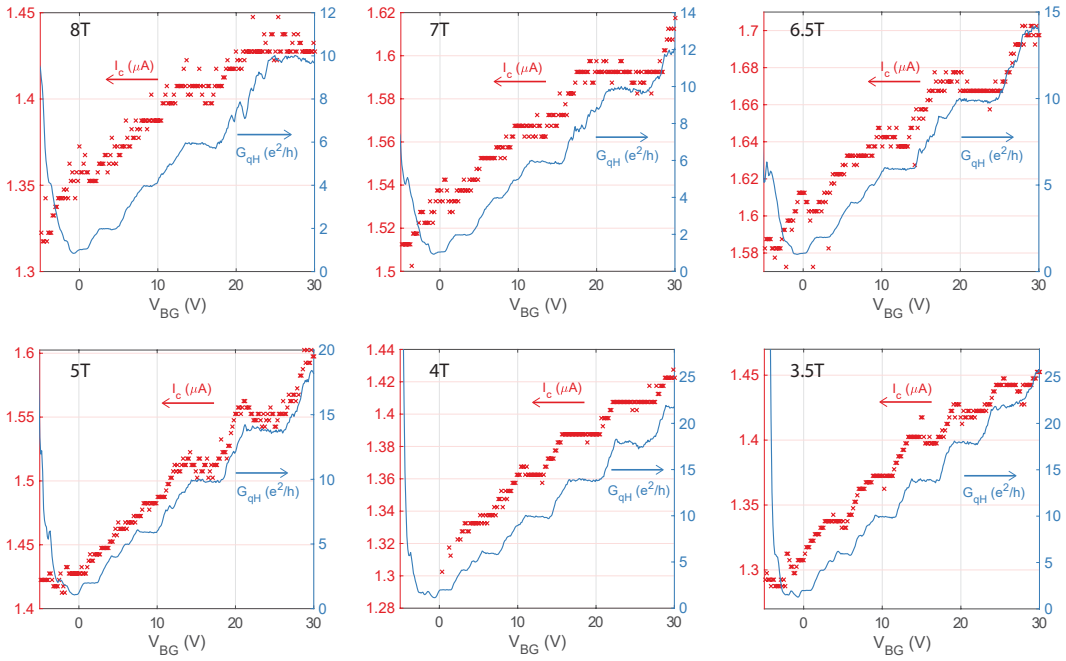

Figure 3.16: A direct comparison of I_c (left axis, red curve) and quantum Hall conductance G_{qH} (right axis, blue curve) measured with normal contacts. Broken symmetry states are not visible in the critical current measured, despite being present in the quantum Hall conductance G_{qH} measurement.

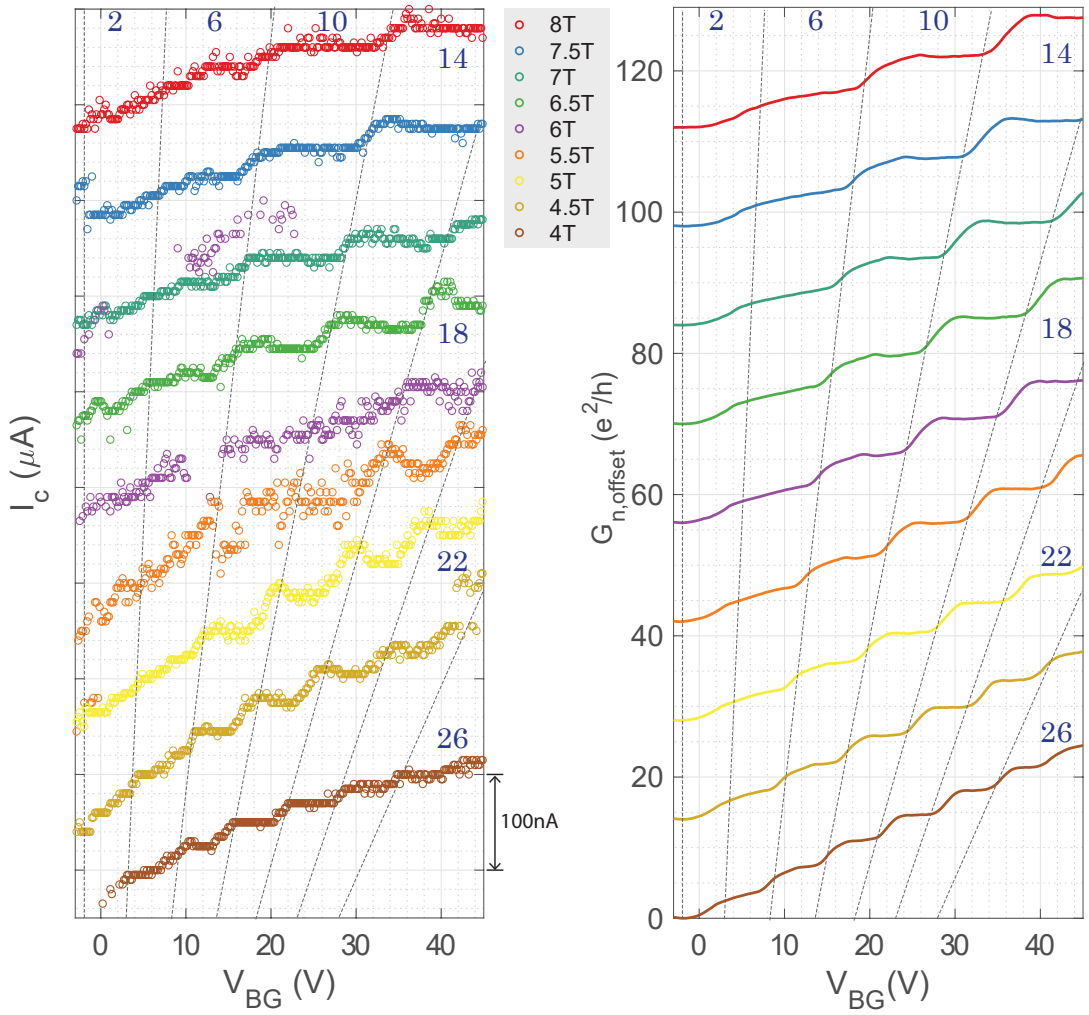

Figure 3.17: Critical current I_c (with an offset) and normal conductance G_n of narrow junction 2, with bulk filling factor ν labelled. Left, I_c with an offset of 100 nA for successive magnetic fields. Right, G_n with an offset of $10e^2/h$ for successive magnetic fields.

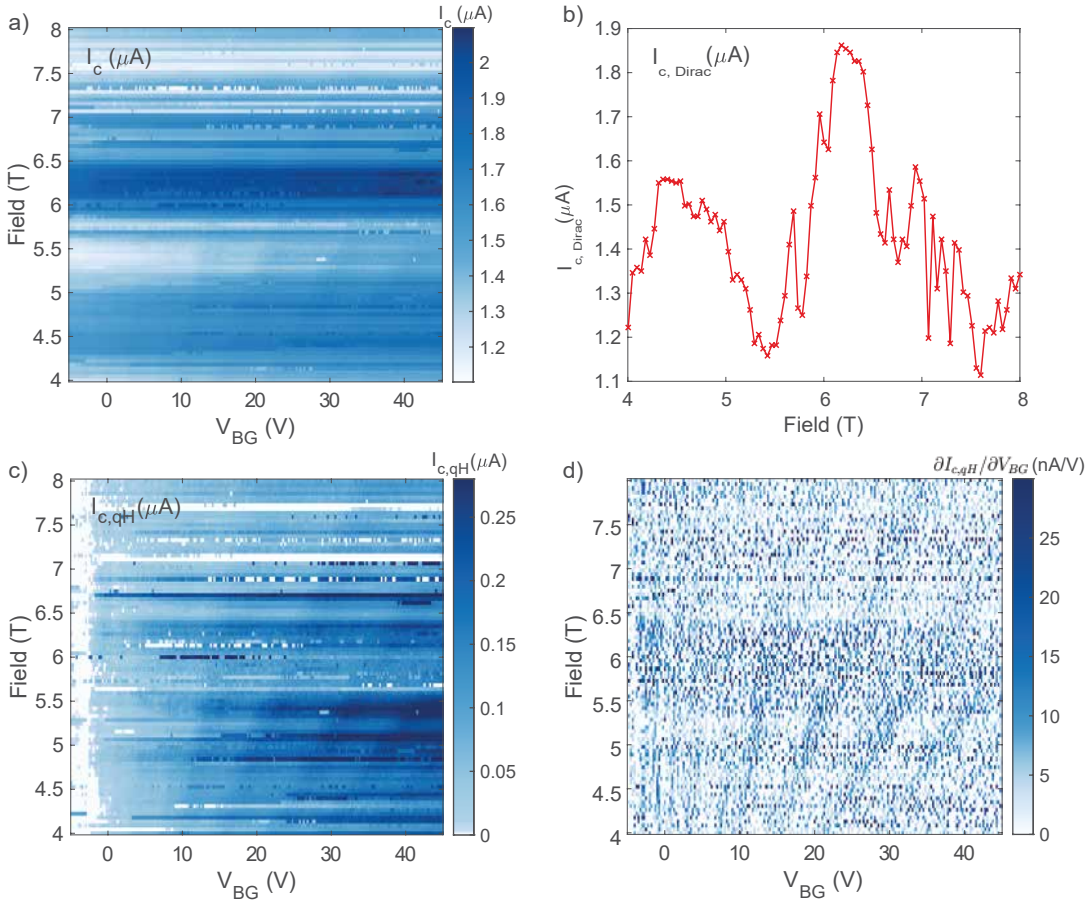

Figure 3.18: Critical current of narrow junction 2. **a**, 2D plot of I_c as a function of back gate voltage (V_{BG}) and magnetic field (Field), showing large fluctuations in I_c across different magnetic fields. **b**, The critical current at the Dirac point (-2.479 V) versus magnetic field. **c**, Critical current $I_{c,qH}$ obtained when $I_{c,Dirac}$ is subtracted from I_c measured for each magnetic field. **d**, A clear fan diagram emerges when we take $\partial I_{c,qH}/\partial V_{BG}$ for each magnetic field.

Because of this effect, even after subtracting off $I_{c,Dirac}$ as we did in Fig. 3.13, which corresponds to subtracting Fig. 3.18b at a given magnetic field from each horizontal line in Fig. 3.18a, we do not obtain a clean fan diagram (Fig. 3.18c). Nevertheless, the step-like feature emerges when we take the differential of I_c with respect to the back gate ($\partial I_{c,qH}/\partial V_{BG}$), as shown in Fig. 3.18d.

Besides having stronger magnetic field dependent fluctuations than narrow junction 1, the discernment of finer features (for example, broken symmetry quantum Hall state signature in I_c) is difficult in narrow junction 2, as both the total critical current I_c and the stepwise increment of ΔI_c is about 4 times smaller than those in narrow junction 1.

3.4.4 Crossed Andreev reflection

The efficiency of Andreev reflection provides a measure of how well the superconductor (NbN) is coupled to the normal material, which we could verify in our narrow junctions through a measurement geometry similar to that in a previous work[20] (Fig. 2.2). The crossed Andreev signal V_{CAR} is normalized by dividing it with the 3-terminal quantum Hall signal V_{qH}. We define R_{CAR} and R_{qH} to be V_{CAR} and V_{qH} divided by the total current passing through the junction respectively. Thus, V_{CAR}/V_{qH} is equivalent to R_{CAR}/R_{qH}.

As shown in Fig. 3.19, a negative voltage was observed for all gate values for narrow junction 1. This is different from the measurement done in the previous work, as the measurement setup employed in this experiment detects both crossed Andreev reflection of the quantum Hall edge states, as well as contributions from compressible states of graphene in between quantum Hall plateaus. At a magnetic field of -8 T, the efficiency of the crossed Andreev reflection decreases with the filling factor of the bulk, with the largest at $\nu = 1$ and $\nu = 2$. However, this trend was not observed in narrow junction 2 at either 8 or -8 T, as the efficiency of the crossed Andreev reflection was close to a constant across different filling factors, as shown in Fig. 3.20.

Crossed Andreev reflection was also measured at elevated incoming electron energies in narrow

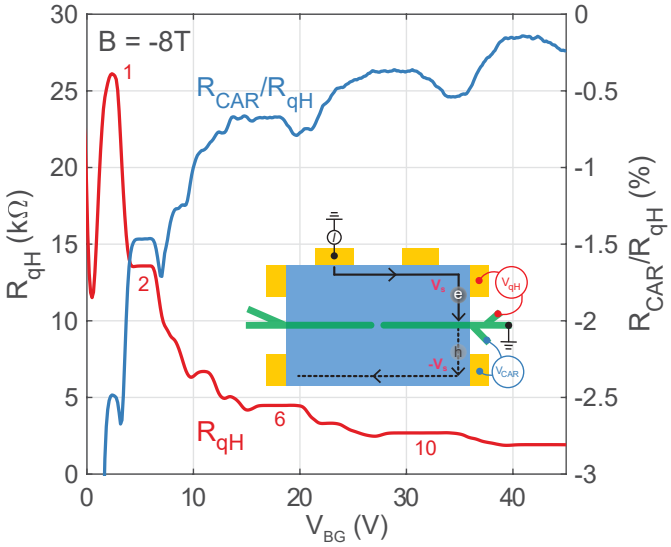

Figure 3.19: Crossed Andreev reflection at -8 T in narrow junction 1. Left axis (red curve): 3-terminal R_{qH}. Right axis (blue curve): The efficiency of the crossed Andreev process, R_{CAR}/R_{qH}, in percentage. Crossed Andreev reflection happens at the interface between graphene and the NbN finger on the right side of the device.

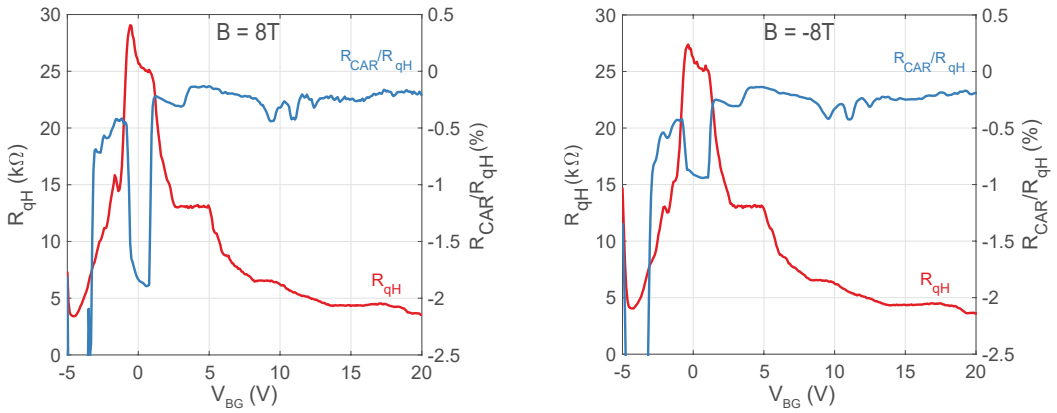

Figure 3.20: Crossed Andreev reflection in narrow junction 2 at 8 T (left) and -8 T (right). Left axis (red curve): 3-terminal R_{qH}. Right axis (blue curve): The efficiency of the crossed Andreev process, R_{CAR}/R_{qH}, in percentage.

junction 1. In addition to the small excitation current (between 20 nA and 100 nA) we used for differential resistance measurement, an additional dc current of a few microamperes was also applied. The measurement geometry and results are shown in Fig. 3.21. As the energy of the incoming electrons increases, we expect the probability of the crossed Andreev reflection to decrease accordingly, as competing processes such as quasi-particle tunneling and co-tunneling become more likely. This trend can be observed in Fig. 3.21b. If we take $\nu = 2$ as an example, the energy of the incoming electrons would be 12.9 k$\Omega \times 2\,\mu$A ~ 2.6 eV, which is comparable to the size of the gap of the NbN superconductor. As such, at a dc current of above 2.1 μA, the measured downstream voltage turns positive as shown in Fig. 3.21b. The 3-terminal resistance V_{qH} was also monitored at the same time, and we observe that the plateaus get washed out as the dc current increases. In addition, when the sourced dc current goes above ~ 6 nA (the critical current of the Josephson junction) at -8 T, a voltage drop develops across the two NbN fingers and this measurement ceases to be a true 3-terminal quantum Hall measurement.

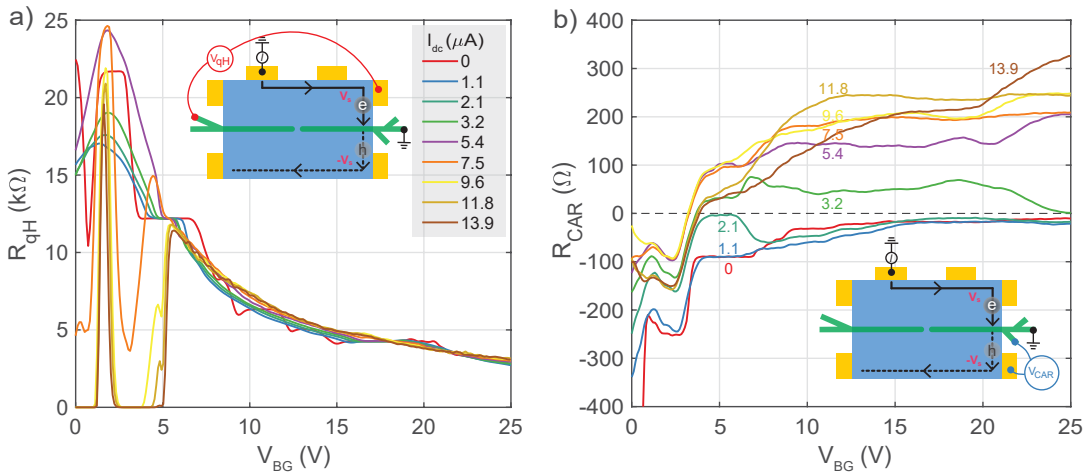

Figure 3.21: Crossed Andreev reflection at -8 T with higher energy incoming electrons. The quantum Hall voltage was monitored concurrently. **a**, 3-terminal quantum Hall voltage V_{qH} measurement. **b**, Crossed Andreev reflection signals turning positive for dc currents above 2.1 μA.

Additional data can be found in Appendix C.

3.4.5 Normal resistance R_n of the junction

In order to better characterize the Josephson junctions, it it important to measure R_{n}, the resistance of the junction in its normal state. R_{n} of the junction was measured at elevated temperatures such that while the Josephson coupling was absent, the NbN contacts were still superconducting. This is to avoid the resistance of NbN contact from being included in the measurement. As the transition of Josephson junction varies as a function of magnetic field, the R_{n} measurement was performed at different temperatures for a given magnetic field. We note that the R_{n} measured here is an estimate of the strict definition of R_{n} in a Josephson junction. A detailed description of the measurement methodology, additional results and analysis of R_{n}, are presented in Appendix D.

The normal resistance R_{n} as function of back gate values and the magnetic field is shown in Fig. 3.22. As part of the current is carried via quantum Hall states, once the Josephson junction turns normal, quantum Hall-like fan diagram features emerge.

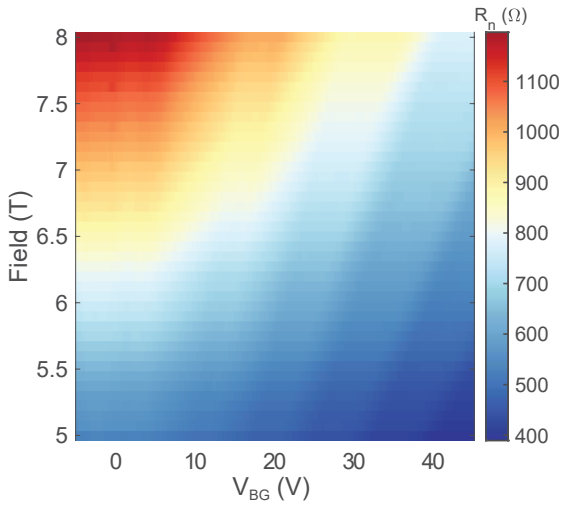

Figure 3.22: The normal resistance R_{n} across the Josephson junction 1, as a function back gate and magnetic field, showing features of a quantum-Hall fan diagram.

Horizontal line cuts of Fig. 3.22, which shows R_{n} as a function of back gate at a fixed magnetic

field, revealed quantum Hall-like steps (Fig. 3.23a). Moreover, at fixed carrier densities (vertical line cuts in Fig. 3.22), R_n increases with increasing magnetic field, with the steps being blunted by the simultaneous increase in resistance due to the decreasing order parameter of NbN, as shown in Fig. 3.23b.

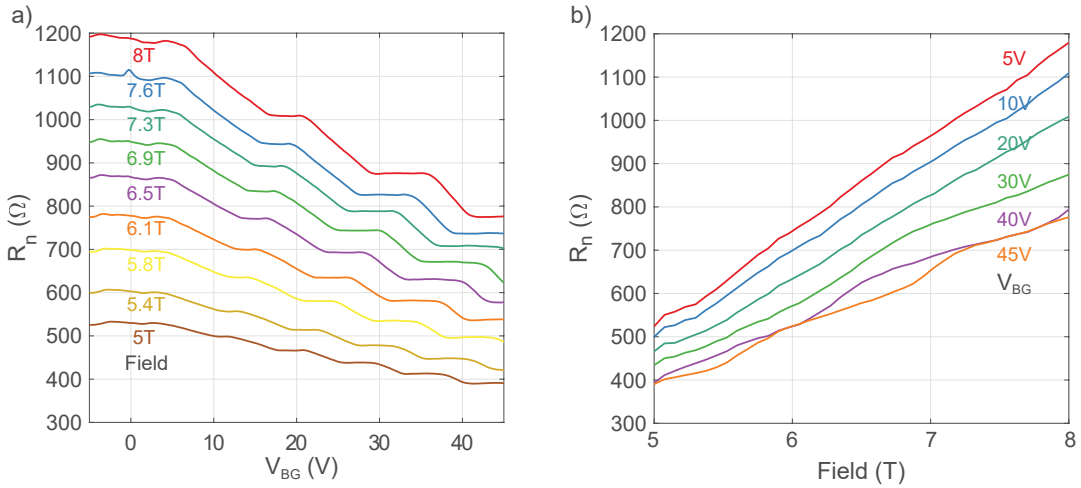

Figure 3.23: **a**, R_n as a function of back gate for several magnetic fields (horizontal line cuts of Fig. 3.22). **b**, R_n as a function of magnetic field for several back gate values (vertical slices of Fig. 3.22).

We further note that the resistance values are an order of magnitude smaller than the expected quantum Hall resistance. This can be understood by considering the junction in its normal state as two resistors, $R_{\text{n, direct}}$ and $R_{n,qH}$, connected in parallel as shown in Fig. 3.24.

For convenience, we consider the normal conductance G_n, and we have

$$G_{\text{n, total}} = G_{\text{n, direct}} + G_{\text{n},qH}. \tag{3.1}$$

Consequently, G_{direct} can be obtained by subtracted $G_{\text{n},qH}$ from $G_{\text{n,total}}$ measured. $G_{\text{n,total}}$ and the corresponding $G_{\text{n, direct}}$ for narrow junction 1 and 2 are shown in Fig. 3.25 and Fig. 3.26 respectively, from which we conclude that G_{direct} is largely gate independent. This agrees with our earlier

conjecture that G_{direct} is due to the NbN weak link and the small region of graphene in between the NbN contacts. Due to contact doping from the contacts, this area of graphene is not gate tunable. A direct comparison of $G_{\text{n, total}}$ and G_{qH} can also be found in Section D.5 of Appendix D.

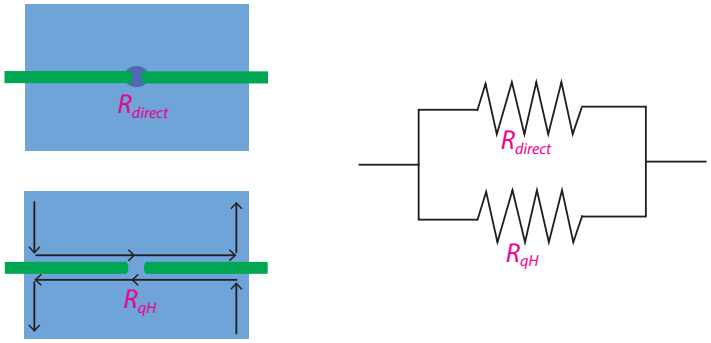

Figure 3.24: The Josephson junction in its normal state is equivalent to a system with two resistors, R_{direct} and R_{qH}, connected in parallel. As $R_{\text{n, direct}}$ is smaller than $R_{n,qH}$, more current goes through the small area of graphene in between NbN contacts than through quantum Hall states.

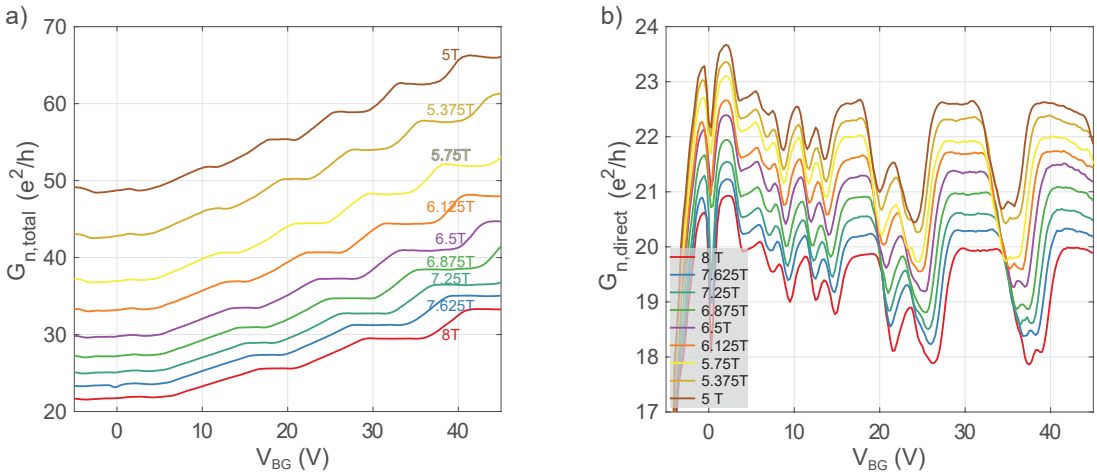

Figure 3.25: **a**, $G_{\text{n,total}}$, and **b**, $G_{\text{n, direct}}$ of narrow junction 1. **b** is obtained by subtracting experimentally measured 3-terminal G_{qH} (Fig. 3.9) from $G_{\text{n, total}}$ in **a**. G_{direct} is constant when the sample is in the quantum Hall regime at a given magnetic field.

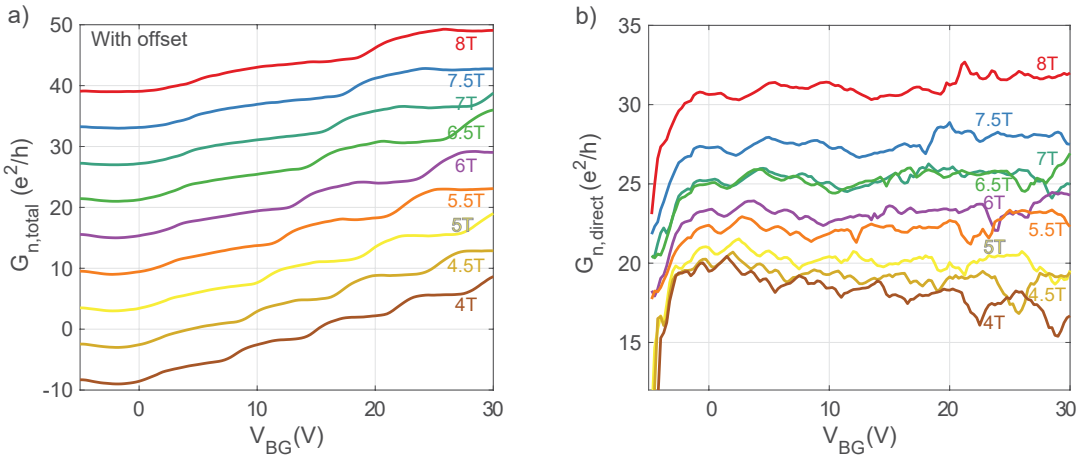

Figure 3.26: **a**, $G_{\text{n,total}}$ (plotted with offset for clarity), and **b**, $G_{\text{n, direct}}$ of narrow junction 2. **b** is obtained by subtracting experimentally measured 3-terminal G_{qH} (Fig. 3.10) from $G_{\text{n, total}}$ in **a**. For a given magnetic field, $G_{\text{n, direct}}$ is approximately constant.

As a side note, while $G_{\text{n, total}}$ and $G_{\text{n, direct}}$ decrease with increasing magnetic field in narrow junction 1 as shown in Fig. 3.25, $G_{\text{n, direct}}$ of narrow junction 2 exhibits an opposite trend in Fig. 3.26. We attribute this to the complex vortex configuration and superconducting coupling between NbN leads in junction 1, and is also evident in the critical current data in Fig. 3.18.

Finally, we calculate the $I_c R_n$ product of the junctions. It is of the same order of magnitude as the superconducting gap of NbN, which is 2 meV. This indicates that the contact between NbN and graphene is in the strongly-coupled regime instead of the tunneling regime, with Andreev processes being readily accessible.

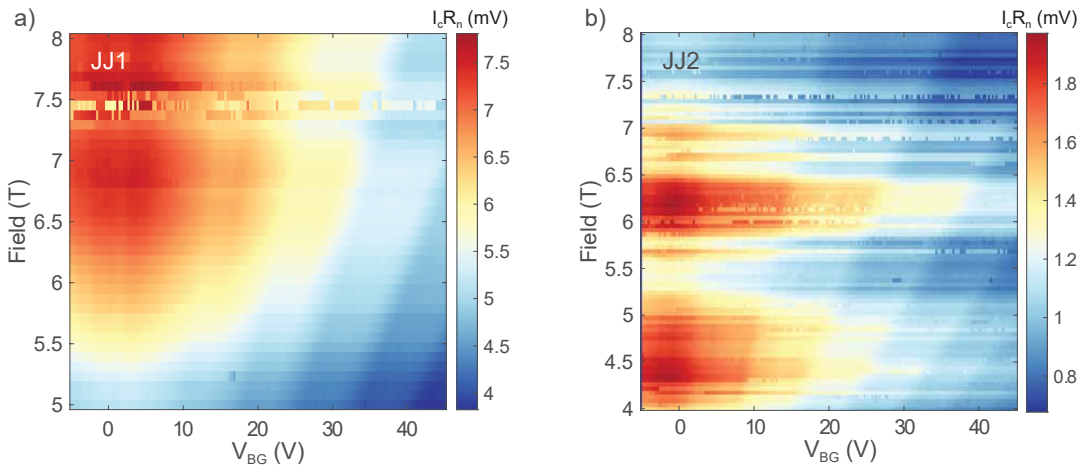

Figure 3.27: The product of I_cR_n as a function of magnetic field and back gate values for **a**, narrow junction 1, and **b**, narrow junction 2. They are both of the same order of magnitude of the superconducting gap of NbN of 2 meV, suggesting a transparent contact between graphene and NbN.

3.5 Shapiro steps at zero magnetic field

As discussed earlier in Chapter 1, a topological Josephson junction exhibits a 4π current-phase relation, which can be verified in an ac Josephson junction measurement (Shapiro step measurement). The microwave power was supplied via an antenna close to the sample, measured at a temperature of about 50 mK in a dilution refrigerator. Although the Josephson junction was superconducting even at 8 T, the Shapiro step signature was quickly washed out in a finite magnetic field. In this section, we will present data at zero magnetic field.

In contrast to a typical Josephson junction, which consists of two superconducting electrodes connected though a weak link (typically a normal metal), the narrow Josephson junctions we studied also have graphene along the length of NbN. Therefore, a narrow junction device can be considered as an ideal Josephson junction with a resistor connected in parallel. Once the current exceeds the I_c of the Josephson junction, the shunting resistance gives rise to a background dc current proportional to the applied dc voltage. Consequently, the discrete increment of current observed at

$V_{dc} = nhf/2e$ in a conventional Josephson junction was not observed. Instead, the Shapiro steps manifest themselves in the differential resistance measurement, as shown in Fig. 3.28. At places where the voltage steps appear (see Fig. 1.12 in Chapter 1 for an example), the differential resistance drops.

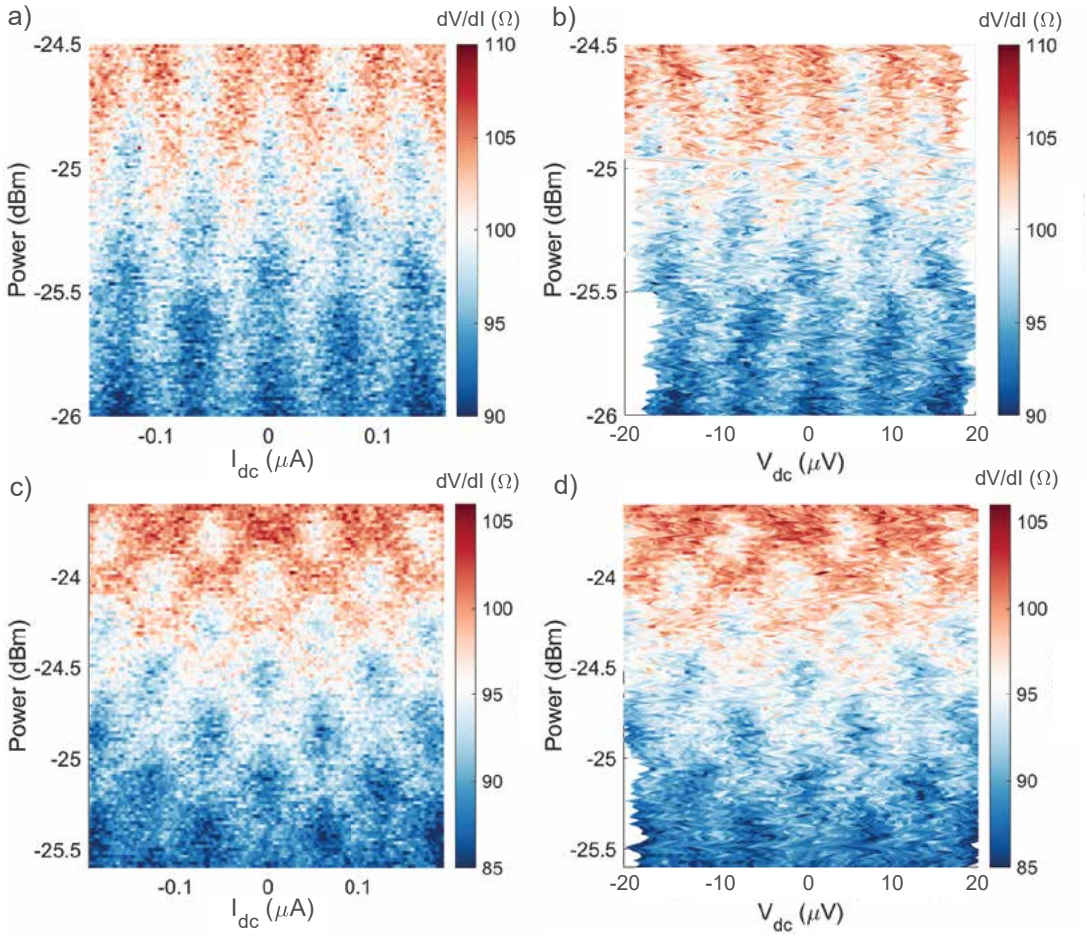

Figure 3.28: Shapiro steps of narrow junction 2 at zero magnetic field, when the device was irradiated with a microwave at 3.367 GHz in **a** and **b**, and 3.041 GHz in **c** and **d**, respectively. The widths of the steps (in volts) are independent of the power of the microwave as seen from each of the 2D plots. The dc voltage across the junction was measured with an operational amplifier, the noise and drift of zero offset over time gives rise to measurement artifacts observed in **b** and **d**.

The same measurement was repeated at 5 different microwave frequencies and the sizes of the

Shapiro steps in dc voltage were plotted against the frequency in Fig. 3.29, confirming that the spacing in voltages observed in a differential measurement in Fig. 3.28 is indeed due to Shapiro steps in an ac Josephson junction.

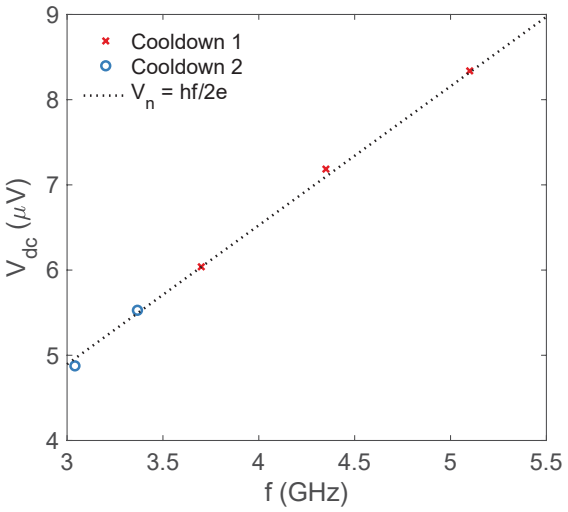

Figure 3.29: The width of Shapiro steps (in μV) from 5 different measurements, plotted against the frequency of the microwave applied, are in good agreement with the expected width of Shapiro steps (the dotted line).

Measure what can be measured, and make measurable
what cannot be measured.

Galileo Galilei

4

Wide quantum Hall Josephson junctions

One question that naturally arises in the study of quantum Hall-mediated narrow Josephson junctions pertains to the exact coupling mechanism between the edge states and the NbN fingers, namely, which states can be considered superconducting "proximitized", and whether the local Andreev reflection or the crossed Andreev reflection plays a bigger role. To address these questions, "wide" Josephson junctions were fabricated with triangularly shaped NBN contacts in which the neighboring two edges of NbN contacts are far enough to suppress any crossed Andreev reflection process.

4.1 Device Geometry

In order to suppress the crossed Andreev reflection while holding the rest of the experimental conditions identical, the dimensions of the graphene in the wide junctions was made similar to that of the narrow junctions, about 2 μm by 3 μm as shown in Fig. 4.1. The triangularly shaped NbN contacts physically separate the counterpropagating edge states on either side of one contact such that they are at a distance further than the coherence length of NbN. At the same time, the local geometry of the closest point of contact of NbN in the center of the device was kept similar to that in the narrow junctions. The designed separation between the closest point of contact of NbN ranged from 50 nm to 60 nm, however they are partially connected in the real device (Fig. 4.1, right), similar to the situation in narrow junctions.

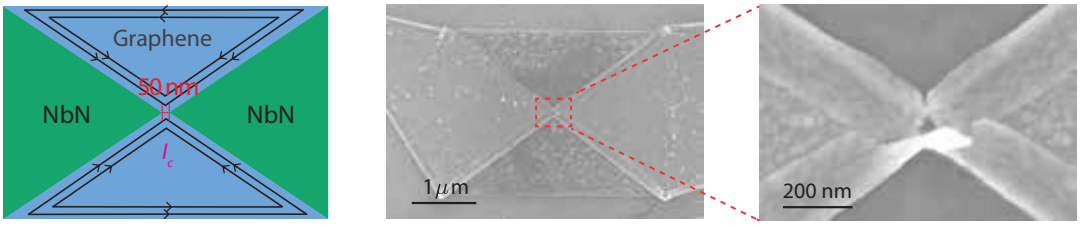

Figure 4.1: Left, the schematic of the wide Josephson junction. Crossed Andreev reflection is suppressed as quantum Hall edge states on opposite edges of the NbN contacts are spatially separated. Middle, an SEM image of the wide junction. Right, A zoomed-in view of the Josephson junction, showing a thin film of NbN connecting the two NbN electrodes, similar to the narrow junctions.

Another difference between this wide junction device and the narrow junction devices is the employment of a graphite back gate in the wide junction device, making it more charge homogeneous across the graphene in the wide junction. Although the quality of the quantum Hall states could not be verified directly due to a lack of normal contacts, based on the measurement of other graphite-gated devices, we are confident that this device has more quantum Hall states at lower magnetic fields compared with the narrow junctions.

4.2 Wide junctions at zero magnetic field

Similar to in the narrow junctions, the gate tunability of the sample was confirmed by measuring dV/dI across the junction at zero magnetic field. In addition, a stronger Josephson coupling between graphene and NbN was observed in the electron-doped regime of graphene, as indicated by a larger critical current and a lower normal resistance in Fig. 4.2. These observations, as well as other NbN-graphene proximity effect measurements, are consistent with the results of narrow junctions in Chapter 3.

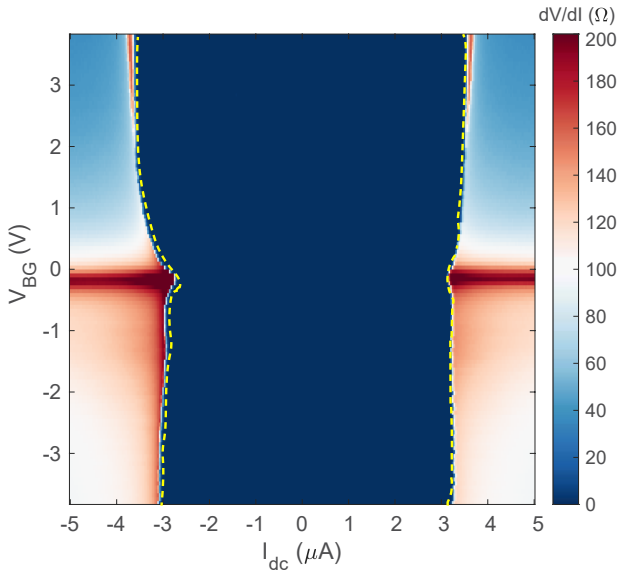

Figure 4.2: Gate dependence of a wide Josephson junction at zero magnetic field. Similar to in the narrow junctions, the smallest critical current was observed around the Dirac point of the graphene. Moreover, the electron-doped graphene has higher critical current and lower normal resistance than in the hole-doped regime.

4.3 Wide junctions at a finite magnetic field

The magnetic field dependence of I_c is similar to that of narrow junction 2 (Fig. 3.7) in that the gate dependence is weak, and that there are Fraunhofer-like oscillations. While the weak gate dependence

might have the same origins as in the narrow junctions, the Fraunhofer oscillations have a smaller periodicity of about 0.7 T, which roughly correspond to a Junction area size of 3000 nm^2. We defer a detailed discussion to Chapter 5.

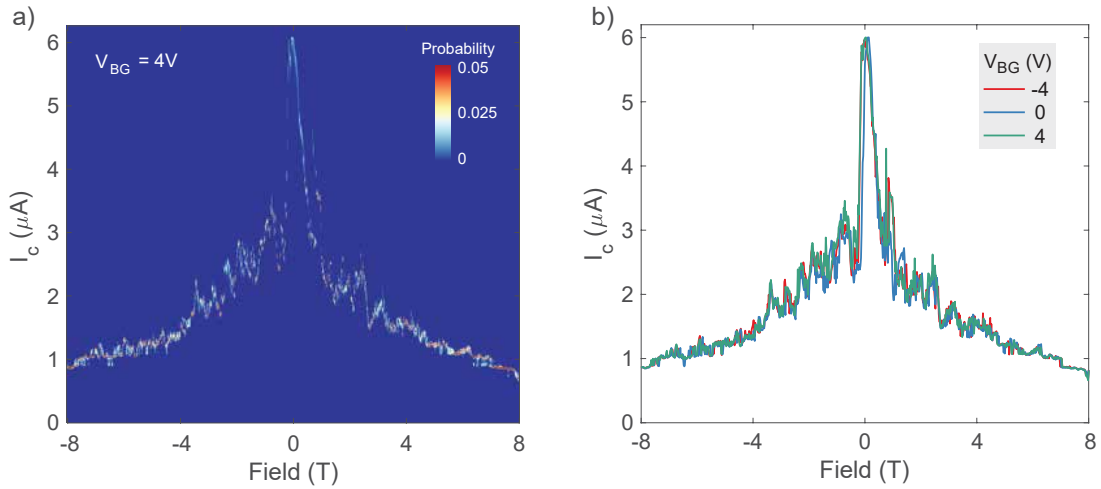

Figure 4.3: Magnetic field dependence of I_c at different back gate voltages. **a**, The probability distribution of I_c at a back gate of 2 V with varying magnetic fields. **b**, The critical current I_c as a function of magnetic field for a few back gate values, showing very little variation in I_c across different back gate voltages.

4.4 Wide junction I_c in the quantum Hall regime

The relationship between the critical current as a function of back gate (or filling factor) at high magnetic fields was investigated. Unlike in the narrow junctions, no step-like features in I_c were observed (Fig. 4.4). This trend is more obvious in Fig. 4.5, where the most probable critical current at each magnetic field is plotted as a function of the back gate voltage.

As explained earlier in section 4.1, the only significant difference between the wide junction and the narrow junction is presence of possible crossed Andreev reflection. By comparing the magnitude of I_c and the step sizes of I_{qH} observed in narrow junctions, we conclude that the absence of steps in I_c in the wide junction is indeed due to the absence of a quantum Hall dependence, instead of a

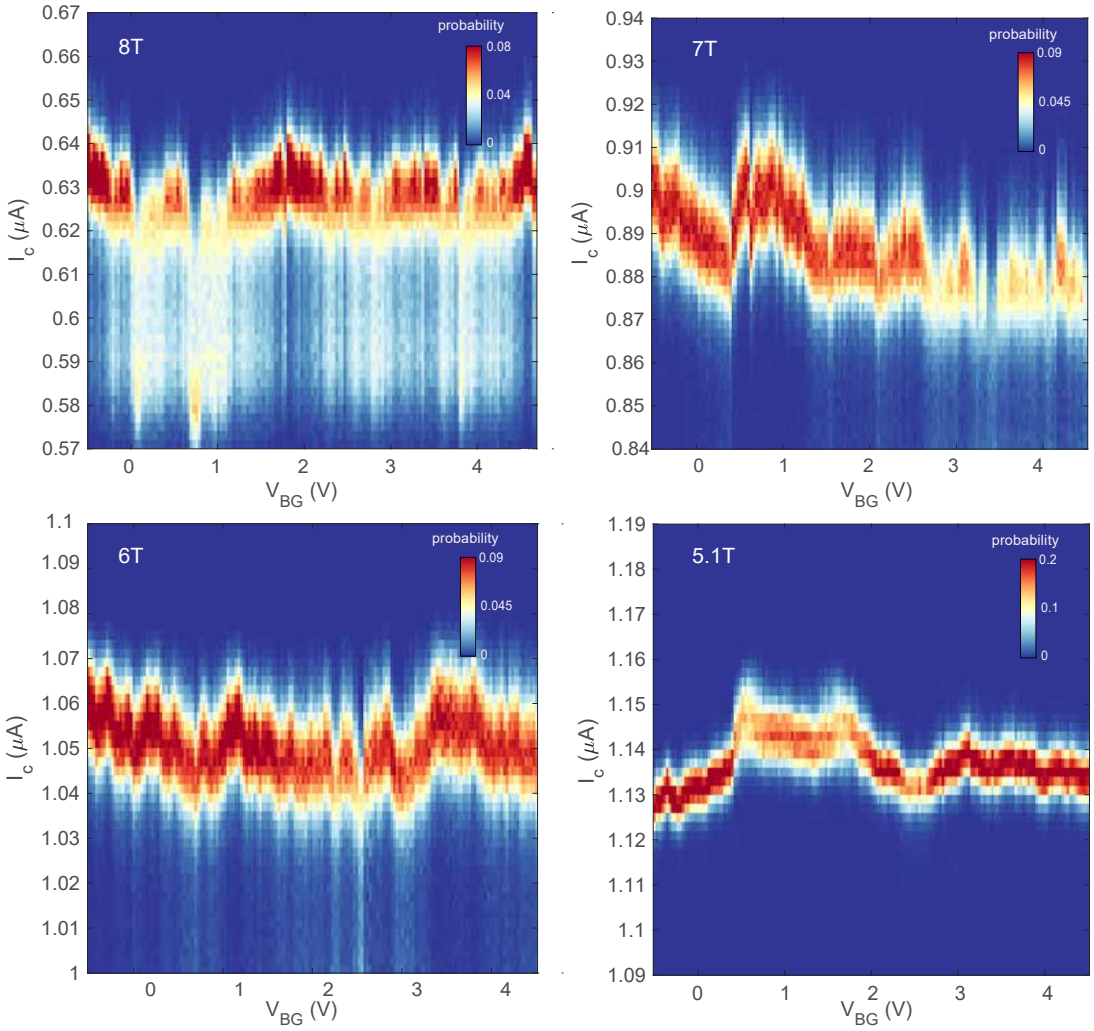

Figure 4.4: Probability distributions of I_c of the wide Josephson junction in the quantum Hall regime. Some modulations were observed but there is no overall increase or any apparent step-like features in I_c.

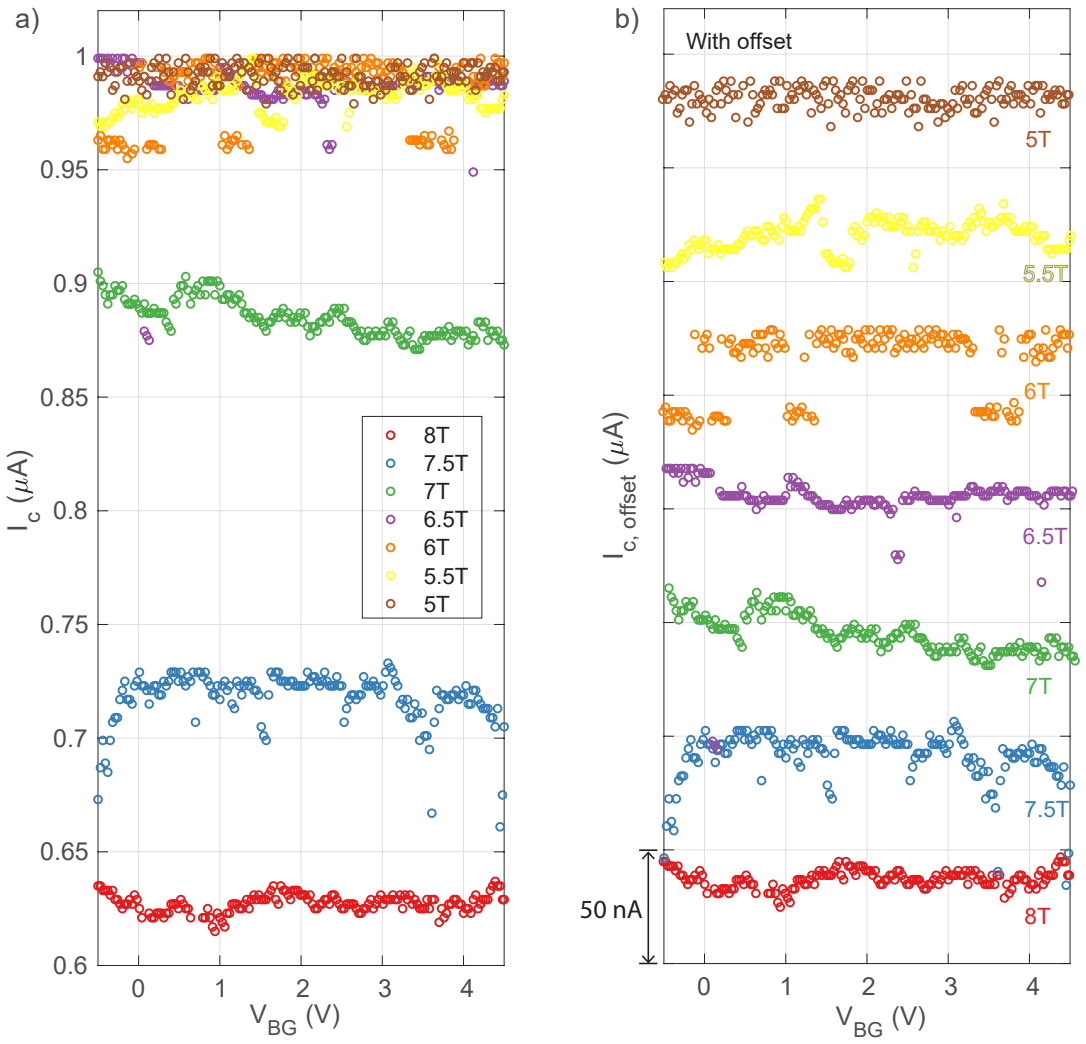

Figure 4.5: Critical current I_c as a function of graphite back gate values at different magnetic fields of the wide junction. **a**, I_c at different magnetic fields. **b**, I_c plotted with an offset, showing the lack of back gate dependence.

measurement artifact as limited by the resolution of the critical current measurement setup.

For narrow junction 1, I_c ranged from 50 nA to 100 nA for every $\nu = 4$ filling factor increment, and for narrow junction 2, an increase in I_c between 30 nA and 60 nA was observed for the same filling factor increment. If there were a similar effect in the wide junction device due to quantum hall states, it would be reasonable to estimate the increment of I_c to be at least 10 nA for every $\nu = 4$ increment in the filling factor. This means that I_c should increase by at least 40 nA for the gate range scanned. Despite this estimate being well within the measurement resolution, no I_c dependence in the filling factor or increase in I_c was observed.

We can perform the same analysis of the I_c by subtracting the critical current at the Dirac point $I_{c,Dirac}$ from the total I_c measured at a particular magnetic field. The ensuing result clearly reveals the lack of back gate dependence, as shown in Fig. 4.6.

The absence of filling factor dependent I_c modulations in the wide junction is consistent with our initial hypothesis that the crossed Andreev reflection is responsible for producing quantum Hall-mediated Josephson current in our devices.

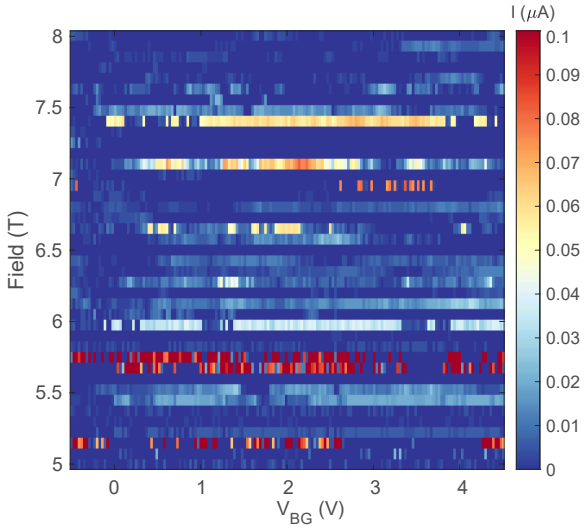

Figure 4.6: I_c - $I_{c,Dirac}$ as a function of back gate and magnetic fields. There was no variation or modulation of I_c when the back gate was varied for a given magnetic field.

Physics is like sex: sure, it may give some practical results,

but that's not why we do it.

Richard Feynman

5

Analysis: Quantum Hall Josephson Junctions

In this chapter, we investigate the origin and characteristics of the quantum Hall critical current, as well as possible spatial distributions of the total Josephson current across both narrow and wide Josephson junctions.

5.1 Decomposition of the Josephson current

As shown in Fig. 3.13 and Fig. 4.5, both the narrow and the wide junctions have a finite I_c in the absence of the quantum Hall edge states at $\nu = 0$. This suggests that the Josephson current must pass through a compressible region of graphene in between the NbN contacts. In addition, the Josephson current must also be carried through quantum Hall states in narrow junction devices, as I_c increases with increasing numbers of edge states when the magnetic field is held constant. More specifically, the total Josephson current I_{total} (Fig. 5.1a) can be decomposed into a non-quantum Hall Josephson current through the compressible bulk I_{direct} (Fig. 5.1b), a Josephson current due to local Andreev reflection I_{AR} (Fig. 5.1c), and a Josephson current due to crossed Andreev reflection I_{CAR} (Fig. 5.1d).

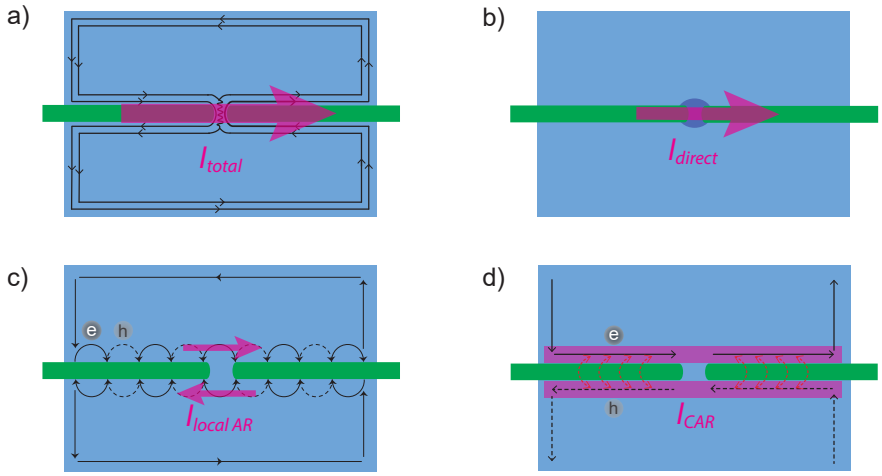

Figure 5.1: Different components of the Josephson current in a quantum Hall Josephson junction, as indicated by magenta arrows. **a**, I_{total}, the total Josephson current. **b**, I_{direct}, the Josephson current through the normal region in between the NbN leads. **c**, I_{AR}, the quantum Hall Josephson current due to local Andreev reflections. **d**, I_{CAR}, quantum Hall Josephson current due to crossed Andreev reflections.

Consequently,

$$I_{\text{total}}(\varphi) = I_{\text{direct}}(\varphi) + I_{AR}(\varphi) + I_{CAR}(\varphi), \tag{5.1}$$

where φ is the superconducting phase difference. The experimental measurable $I_{\text{c, total}}$ of the junction, is the maximum of the stationary current with respect to the phase difference φ, i.e. $I_{\text{c, total}} = \text{Max}_{\varphi}\{I_{\text{total}}(\varphi)\}$.

The local quantum Hall Josephson current I_{AR} is carried by the Andreev bound states formed by quantum Hall edge states on a single side of the NbN leads, as the edge states loop around either the upper or the lower half of graphene. Based on the symmetry in the device, I_{AR} from the upper and lower halves of the graphene are equal in magnitude but opposite in direction. Therefore, the net Josephson current due to the local Andreev process is zero, i.e. $I_{AR}(\varphi) = 0$.

Thus, for narrow Josephson junctions,

$$I_{\text{total}}(\varphi) = I_{\text{direct}}(\varphi) + I_{CAR}(\varphi), \tag{5.2}$$

and for wide Josephson junctions,

$$I_{\text{total}}(\varphi) = I_{\text{direct}}(\varphi). \tag{5.3}$$

The flow of different components of the Josephson current across the junction is illustrated in Fig. 5.2. The blue region in between the green NbN electrodes represents the weak link consisted of highly doped, gate-independent graphene, and possibly a thin NbN film from an imperfect lift-off during fabrication (discussed previously in Chapter 3.4.5). The white space around NbN electrodes in Fig. 5.2 is the rest of the graphene, which is gate tunable and can carry a Josephson current through crossed Andreev reflection of quantum Hall edge states only in narrow junctions.

Therefore, a narrow Josephson junction can be formally regarded as two Josephson junctions, namely $\text{JJ}_{\text{direct}}$ and JJ_{CAR} connected in parallel, whereas a wide junction can be regarded as being equivalent to $\text{JJ}_{\text{direct}}$.

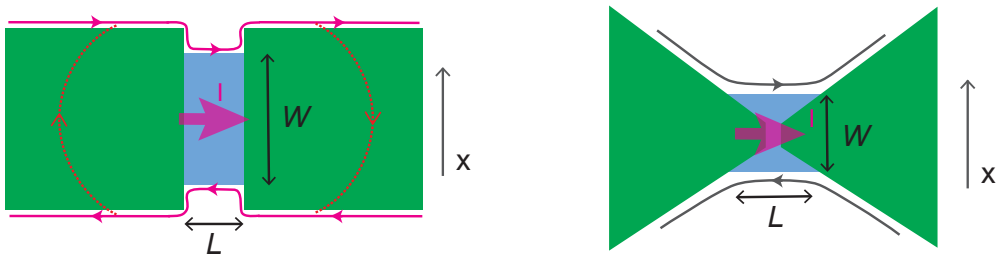

Figure 5.2: The flow of Josephson current across both the narrow and wide Josephson junctions. In the narrow junctions (left), the Josephson current consists of I_{direct} flowing through the middle graphene (light blue) and possibly a NbN thin film from an imperfect lift-off, and I_{CAR} along the edges of NbN leads due to crossed Andreev reflection of quantum Hall states. In the wide junctions (right), the crossed Andreev reflection is suppressed and only I_{direct} contributes to the Josephson current.

5.2 The direct Josephson current I_{direct}

I_{direct} is the Josephson current associated with $\text{JJ}_{\text{direct}}$. In Section 3.4.5 of Chapter 3, we established that the normal conductance of $\text{JJ}_{\text{direct}}$, $G_{\text{n,direct}}$, is gate independent due to the close proximity between graphene and NbN contacts, and verified it with data. Furthermore, the $I_{\text{c}}R_{\text{n}}$ product of $\text{JJ}_{\text{direct}}$ should be a constant at a given magnetic field, as the vortex configuration and the order parameter of NbN leads remain unchanged. As a result, $I_{\text{c, direct}}$ is expected to be gate independent at a given magnetic field. In fact, $I_{\text{c, direct}}$ is equivalent to $I_{\text{c},Dirac}$, the critical current at the Dirac point of graphene, which is a constant offset to $I_{\text{c, total}}$, as analyzed earlier in Chapter 3.

At the same time, because the wide junction only contains $\text{JJ}_{\text{direct}}$, $I_{\text{c, direct}}$ remains constant for a given magnetic field, as seen from Fig. 4.5 of Chapter 4.

5.3 The quantum Hall Josephson current I_{CAR}

I_{CAR} comes from the crossed Andreev reflection of counterpropagating edge states on either side of the NbN contact, its presence in the narrow junctions, as well as its absence in the wide junctions are confirmed in Chapter 3 and Chapter 4, respectively. The data are reproduced in Fig. 5.3 for

easier comparison.

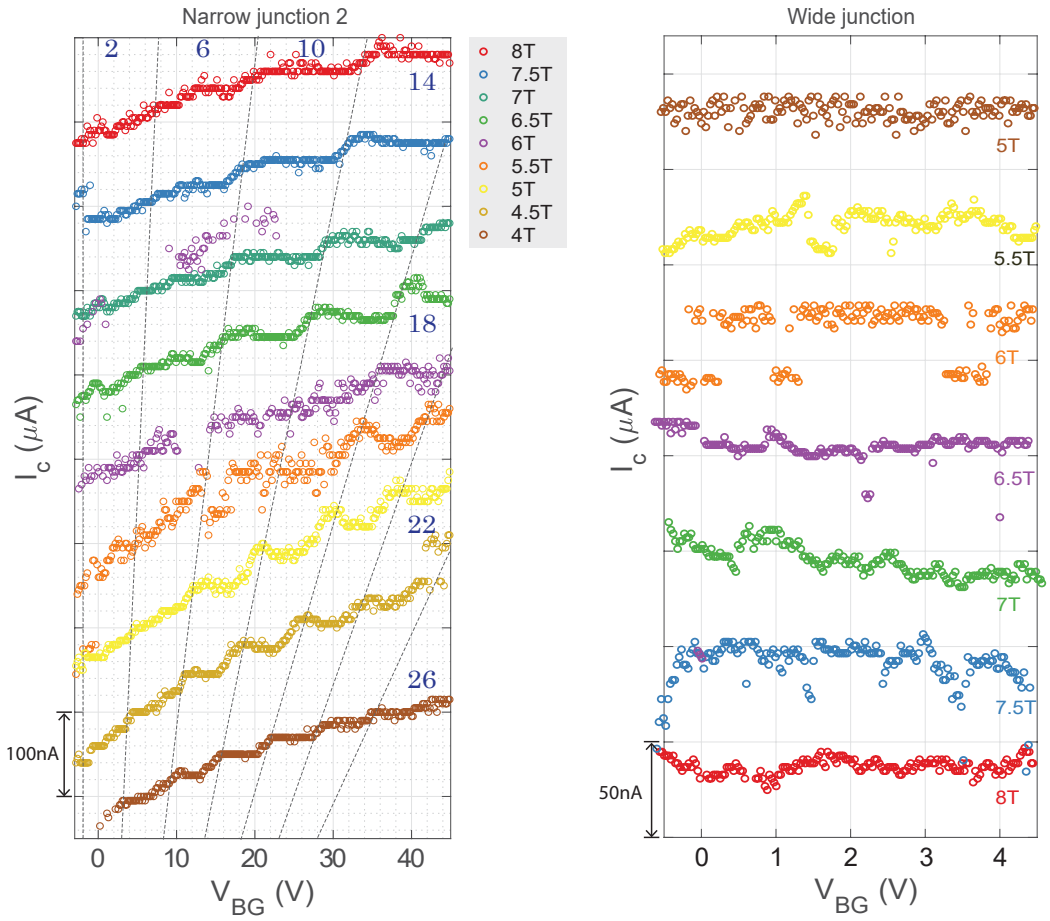

Figure 5.3: Step-wise increment in I_c was observed in narrow junctions but not the wide junction. Left, Critical current of narrow junction 1 (with offset) at different magnetic fields. Right, Critical current of the wide junction (with offset) at different magnetic fields.

Furthermore, in the narrow junctions, I_{CAR} shows a sub-linear dependence on the filling factor ν, or the carrier density in the sample, as shown in Fig. 5.4. This suggests that the superconducting coupling between the quantum Hall edge states and NbN leads through crossed Andreev reflection gets weaker for edge states at higher filling factors.

Although the coupling between different edge states and NbN depends on the potential pro-

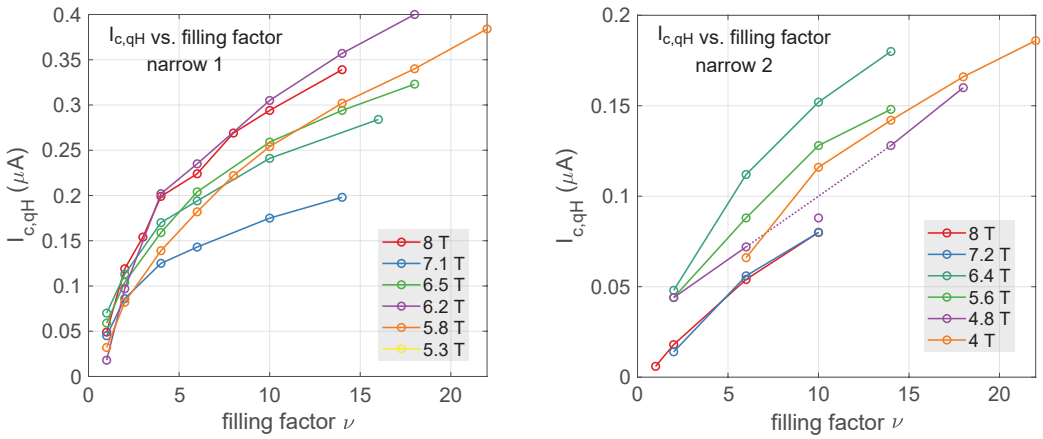

Figure 5.4: Sublinear dependence of $I_{c,qH}$ on carrier density in narrow junctions 1 (left) and 2 (right), suggesting that the crossed Andreev reflection of quantum Hall states weakens at higher filling factors. This trend is less obvious in narrow junction 2 due to the relatively small magnitude of I_c and $I_{c,qH}$.

file at the graphene-NbN interface and thus would require a more careful calculation, the sublinear I_{CAR} dependence on the filling factor can be explained qualitatively as follows. The edge states at higher filling factors are spatially further away from the graphene-NbN interface, as shown in Fig. 5.5. At the same time, the critical current due to a single edge channel decays exponentially with an increasing distance between counterpropagating modes on either side of the NbN lead, i.e. for the Nth quantum Hall edge, $I_{c,N} \propto \Delta_0 e^{-L/\xi}$, with Δ_0 and ξ being the order parameter and the coherence length of NbN respectively. Therefore, higher edge states contribute increasingly less to the total critical current, leading to a sublinear dependence of $I_{c,qH}$ on the filling factor.

More specifically, we can consider a simplified model with adjacent edge states separated by a small constant distance a, corresponding to the situation of a sharp potential profile at the graphene-NbN interface (Fig. 5.5). Consequently, the Nth edge state is at a distance Na from the graphene-NbN interface. For a superconductor of width W_s, the distance L between the Nth counterpropa-

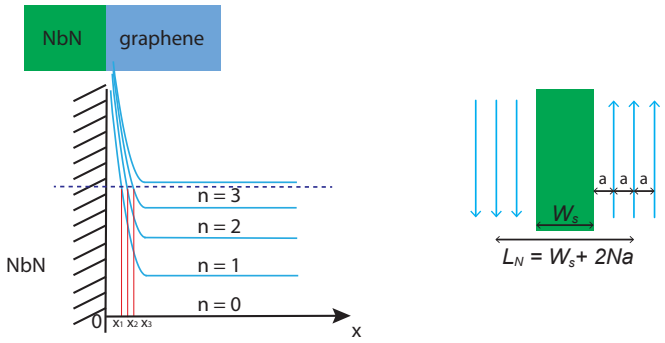

Figure 5.5: Left: Quantum Hall edge states near the graphene–NbN interface. Right: For simplicity, we assume a constant separation a between adjacent quantum Hall edges. With N filled Landau levels, $I_{c,N} \propto \Delta_0 e^{-L/\xi}$.

gating edge states then satisfies $L = W_s + 2Na$. With N filled Landau levels, we have

$$\begin{aligned} I_c(N) &\simeq \sum_{\text{all } x_N} \Delta_0 e^{-(W_s+2x_N)/\xi} \\ &= \Delta_0 e^{-W_s/\xi} \left(\sum_{n=0}^{N-1} e^{(-2na)/\xi}\right) \\ &= \Delta_0 e^{-W_s/\xi} \left(\frac{1-e^{(-2a/\xi)N}}{1-e^{-2a/\xi}}\right). \end{aligned} \tag{5.4}$$

Assuming that both a/ξ and aN/ξ are small,

$$\begin{aligned} I_c(N) &\simeq \Delta_0 e^{-W_s/\xi} \left(\frac{1-\left(1-2(a/\xi)N+2(a/\xi)^2N^2\right)}{1-(1-2a/\xi)}\right) \\ &\simeq \Delta_0 e^{-W_s/\xi} \left(N-(a/\xi)N^2\right). \end{aligned} \tag{5.5}$$

We fitted the data to the quadratic expression $I_c(N) = p_1N^2 + p_2N + p_3$ for both narrow junctions 1 and 2, and the ratio of the coefficients $|p_1/p_2|$ from the fit gives the ratio a/ξ in Eq. 5.5. The results for a few magnetic fields are shown in Fig. 5.6, with a/ξ being around $0.02 \sim 0.03$. Using the coherence length of NbN for ξ(100 nm), then a is about $2 \sim 3$ nm. We note that the magnetic length l_b is about 10 nm (12.8 nm at 4 T, and 9 nm at 8 T), a few times larger than a obtained from

this calculation. As ξ is inversely proportional to the superconducting gap Δ and $\Delta_{qH} < \Delta_{\mathrm{NbN}}$, $\xi_{qH,\mathrm{sc}}$ is likely to be larger than ξ_{NbN}, which would lead to a separation a comparable to the magnetic length l_b.

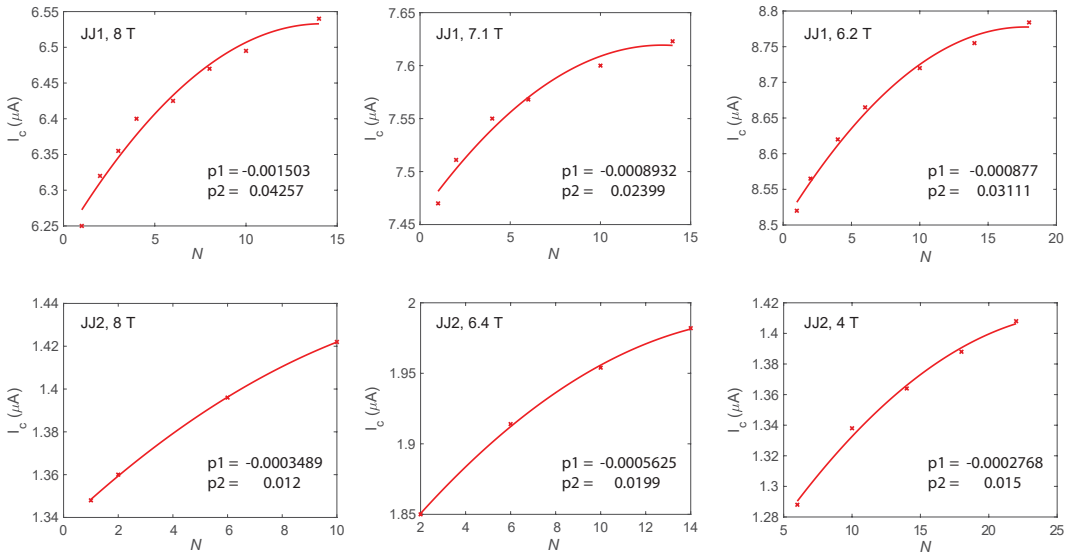

Figure 5.6: Fitting I_c of narrow junction 1 (upper panel) and narrow junction 2 (lower panel) to Eq. 5.5 in the form of $I_c(N) = p_1N^2 + p_2N + p_3$, where N is the Nth Landau level that the system is at. The constant term p_3 accounts for the constant offset due to $I_{c,\,\mathrm{direct}}$ as discussed in the previous section. a/ξ ranges from $0.02 \sim 0.03$. With $\xi = 100$ nm, the separation a between adjacent quantum Hall edges is about $2 \sim 3$ nm.

We note that this is an oversimplification in analyzing the I_c dependence on the filling factor in a quantum Hall Josephson junction. The assumptions that the edge states are spatially separated with an equal distance a, and that the position of each edge state stays fixed even when the filling factor varies, are not realistic. One can conceive other models based entirely on the geometry of the edge states that would correct these issues, but without considering the edge potential and tunneling between the edge states and NbN, such geometry-based models would remain as a crude estimate.

5.4 Relative magnitude of $I_{c,direct}$ and $I_{c,CAR}$

In both narrow junctions 1 and 2, $I_{\mathrm{c,\,direct}}$ is tens of times larger than $I_{\mathrm{c},CAR}$ throughout the gate range scanned. One reason for the large I_{direct} contribution could be due to the residual NbN weak link from the lift-off process. However, even without any NbN weak link, the channel length and width of a quantum Hall Josephson junction affect the relative magnitude of of $I_{\mathrm{c,\,direct}}$ and $I_{\mathrm{c},CAR}$.

Consider two different channel lengths L as shown in Fig. 5.7.

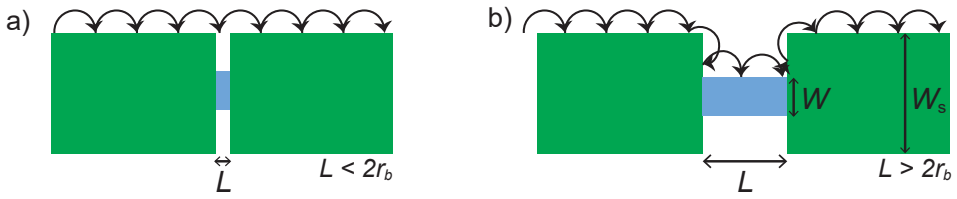

Figure 5.7: Josephson junction channel length L dependence of $I_{\mathrm{c,\,direct}}$ and $I_{\mathrm{c,\,CAR}}$. Green: NbN electrons; blue: Josephson junction weak link. **a**, $L < 2r_b$. $I_{\mathrm{c,\,direct}}$ is the strongest due to the close proximity of the superconducting NbN contacts. **b**, $L > 2r_b$ and $(W_{\mathrm{s}} - W)/2 > r_b$. $I_{\mathrm{c,\,direct}}$ decreases exponentially with increasing channel length. On the other hand, $I_{\mathrm{c},CAR}$ is enhanced because the blue region (weak link) is narrower than the NbN leads, and stronger Andreev bound states can be formed between the edge states travelling above and below the weak link. For **a** and **b**, only quantum Hall edge states along the top edges of NbN contacts are shown for clarity.

In Fig. 5.7a, the NbN electrodes are close together such that $L < 2r_b$, where r_b is the cyclotron radius given by $r_b = \hbar k_{\mathrm{F}}/eB = \hbar\sqrt{\pi n}/eB$ in graphene. In this case, $I_{\mathrm{c,\,direct}}$ is strong due to the close proximity of NbN leads. In addition, edge states do not enter into the white space in between the NbN electrodes.

In Fig. 5.7b, where $L > 2r_b$ and $(W_{\mathrm{s}} - W)/2 > r_b$, the edge states enter the region in between the NbN electrodes. As the width of the weak link region W is smaller than that of the NbN leads W_s, $I_{\mathrm{c},CAR}$ is enhanced in this geometry due to the formation of stronger Andreev bound states in the weak link region. While $I_{\mathrm{c,\,direct}}$ decreases exponentially with increasing L/ξ, where ξ is the coherence length of NbN, $I_{\mathrm{c},CAR}$ is more insensitive to the increase in L, as quantum Hall states can be thought of as having a much longer coherence length than the metal. Thus, Fig. 5.7b is the

preferred geometry for the experimental observation of $I_{c,CAR}$.

Additionally, for the situation depicted in Fig. 5.7b, a smaller channel width W also enhances I_{CAR} and suppresses I_{direct} through a stronger Andreev bound state formation and an increased $R_{\text{n, direct}}$.

In the narrow junctions 1 and 2, $W_s \simeq 100$ nm, $W \simeq 80$ nm, and with $r_b \simeq 15$ nm at a magnetic field of 8 T, which make them somewhat in between the two scenarios illustrated in Fig. 5.7.

5.5 Spatial distributions of the Josephson current

We have established that I_{direct} flows through the region in between the NbN contacts and that I_{CAR} due to the quantum Hall states flows on either side of the NbN contacts as shown in Fig. 5.2. Such a current decomposition suggests that the spatial current distribution consists of a bulk current and an edge current. This can be verified with the critical current vs. magnetic field measurement.

When a magnetic flux Φ passes through a Josephson junction, a position-dependent superconducting phase difference φ parallel to the graphene/contact interface develops[37]. Taking Fig. 5.2 as an example, an out-of-plane magnetic field gives rise to a phase difference $\Delta\varphi(x) = 2\pi\Phi x/\Phi_0 W$, where $\Phi_0 = h/2e$ is the flux quantum. The interference resulting from the phase difference gives rise to modulations in I_c as a function of the magnetic field, also referred to as a Fraunhofer pattern. As an example, a uniform spatial current distribution shown in Fig. 5.8a gives a magnetic field dependence of I_c as shown in Fig. 5.8b.

The experimental results of the critical current as a function of magnetic field for the narrow Josephson junctions and the wide junction are reproduced in Fig. 5.9. As the difference between different gate voltages is minor, data taken in the highly-doped regime of graphene are shown in Fig. 5.9.

In narrow junction 1 (Fig. 5.9a), Fraunhofer oscillations are largely absent, suggesting that the

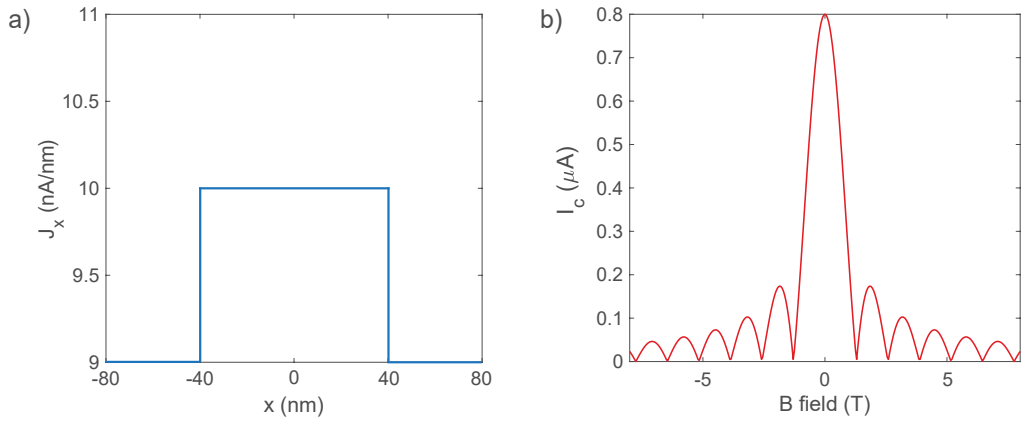

Figure 5.8: Fraunhofer pattern of a spatially uniform Josephson current. **a**, Uniform current density along the direction of graphene–NbN contact. **b**, The corresponding I_c in a finite magnetic field.

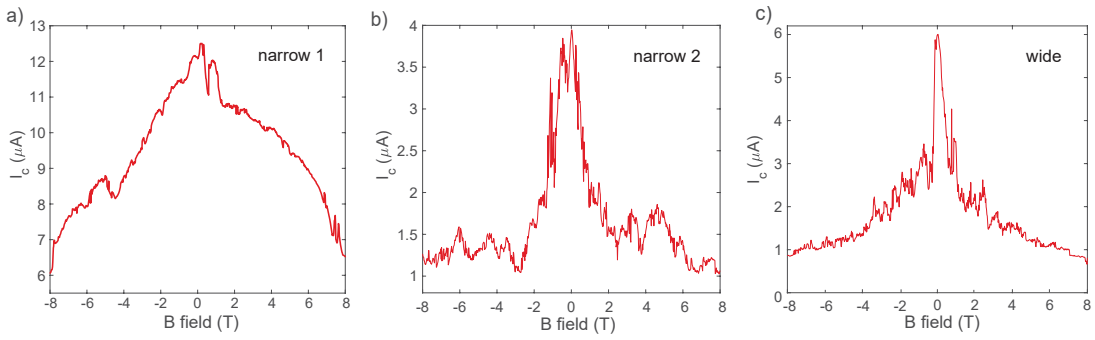

Figure 5.9: A comparison of Fraunhofer patterns of I_c in narrow and wide Josephson junctions. **a**, Narrow junction 1 at a back gate of 40 V, reprinted from Fig. 3.6. **b**, Narrow Junction 2 at a back gate of 40 V, reprinted from Fig. 3.7a. **c**, Wide junction at a back gate of 4 V (graphite back gate), reprinted from Fig. 4.3b.

interference under a magnetic field was not the dominant effect. The slowly decaying critical current profile is consistent with a current distribution in which most of the current goes through the middle of the junction through the NbN weak link as I_{direct}. Consequently, an increased magnetic field causes the I_c to drop as the order parameter of the NbN decreases. Moreover, the asymmetry of I_c with respect to the magnetic field could be a direct result of an asymmetric spatial distribution across narrow junction 1.

For narrow junction 2 and the wide junction (Fig. 5.9b and Fig. 5.9c), I_c is more symmetric, and the oscillations of I_c as a function of magnetic field can be related to the spatial distribution of current via

$$I_c(B) = \left| \int_{-W/2}^{W/2} J(x) \cdot e^{2\pi i L B x/\Phi_0} dx \right|, \tag{5.6}$$

where $J(x)$ is the current density along the direction of the direction of graphene–NbN contact (Fig. 5.2). Eq. 5.6 allows the magnetic dependence of I_c to be deduced from the real space distribution of the Josephson current[9,14,16]. It has also been used to analyze the current distribution in graphene Josephson junctions[4]. Here we test a bulk-and-edge current model with Eq. 5.6 by comparing the expected magnetic field dependence of I_c to the experimental data.

From the SEM images, the narrow NbN electrodes are about 100 nm wide, and we estimate W to be 80 nm. For narrow junction 2, the separation of the NbN electrodes L was estimated to be 20 nm, based on a periodicity of approximately 1.3 T from the measured Fraunhofer oscillations in Fig. 5.9b. The I_c vs. magnetic field data for narrow junction 2 (Fig. 5.10b) can be produced by a spatial current distribution as shown in Fig. 5.10a.

For the wide junction the magnetic field dependence of I_c also exhibits oscillations (Fig. 5.9c), despite the sole contribution of I_c being the direct current I_{direct} through the middle of the junction. Therefore, in the wide junction, I_{direct} itself could have some current concentrated near the edges of the effective Josephson junction area (light blue area in the inset of Fig. 5.11a). A spatial current dis-

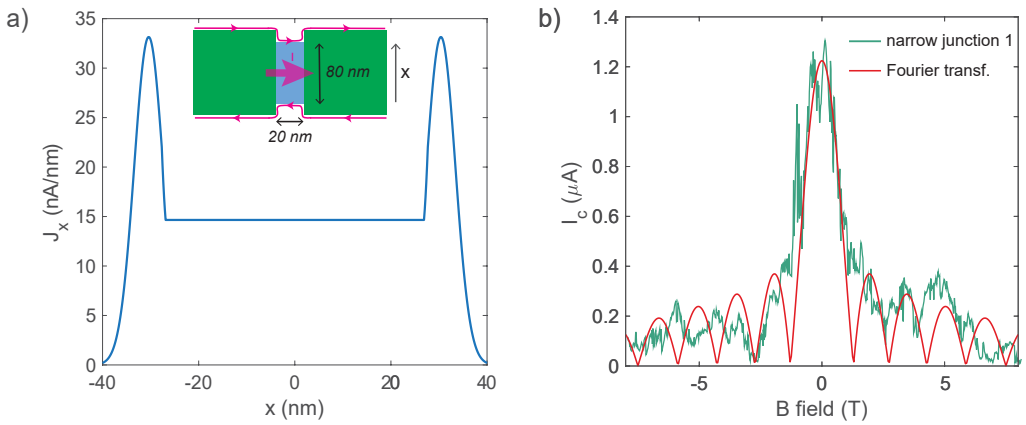

Figure 5.10: With $W = 80$ nm, $L = 20$ nm, and a spatial distribution of Josephson current as shown in **a**, the corresponding magnetic field dependence of I_c calculated with Eq. 5.6 is plotted in red in **b**. The periodicity and relative magnitude of the oscillations of I_c agree with experimental data (green) for narrow junction 2.

tribution as shown in Fig. 5.11a would produce a Fraunhofer pattern similar to what was observed in the experiment shown in Fig. 5.11b.

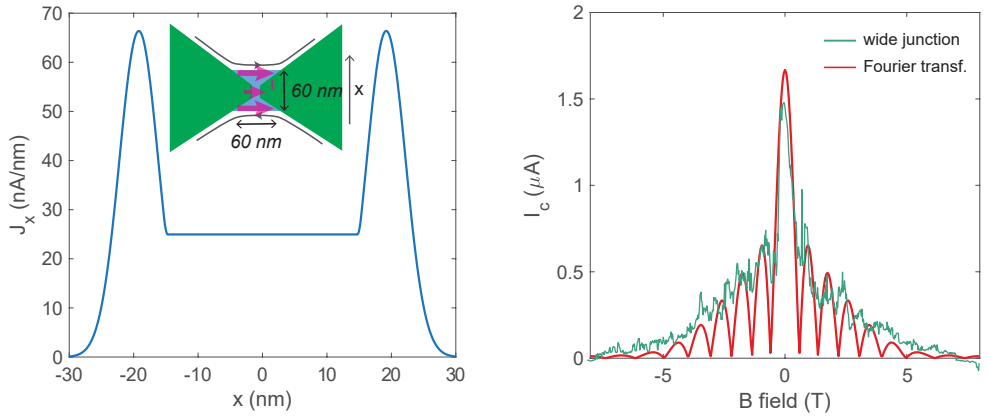

Figure 5.11: With $W = 60$ nm, $L = 60$ nm, and a spatial distribution of I_c as shown in **a**, the corresponding magnetic field dependence of I_c calculated with Eq. 5.6 is plotted in red in **b**. The periodicity and relative magnitude of the oscillations of I_c agree with experimental data (green) for the wide junction.

Comparing with the edge current contribution due to I_{CAR} in narrow junction 2 in Fig. 5.10a, there is more current flowing at the edge due to I_{direct} in the wide junction (Fig. 5.11a), consis-

tent with the conjecture that most of the Josephson current in these Josephson junctions is carried through the bulk via I_{direct}, with a small additional contribution from quantum Hall-mediated Josephson current when crossed Andreev reflection is allowed in the system.

We also attempted to fit a spatial current distribution to the I_c vs. magnetic field data for narrow junction 1 in Fig. 5.12. In this case, an I_{direct} concentrated in the center and some edge current due to I_{CAR} as shown in Fig. 5.12a accounts for the broad features in the data (Fig.5.12b, green).

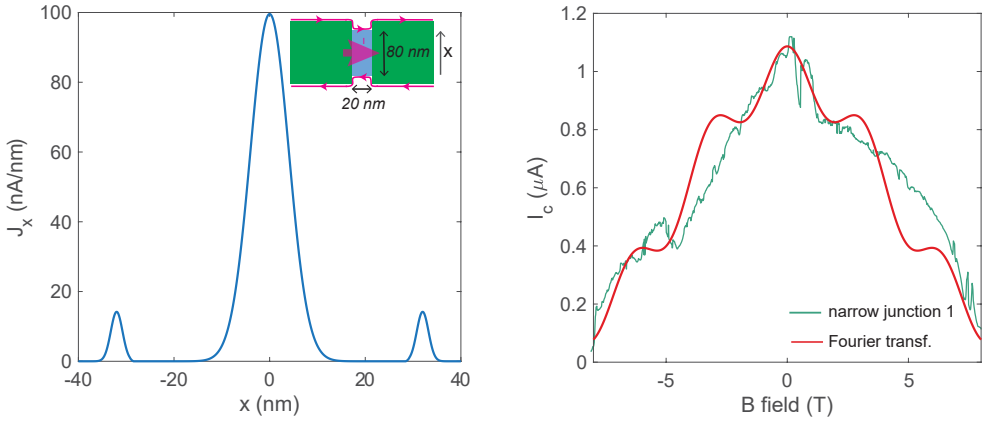

Figure 5.12: a, A possible spatial distribution of Josephson current in narrow junction 1, with most of the current going through the middle of the junction as I_{direct} and I_{CAR} along the edge, for dimensions of $W = 80$ nm, $L = 20$ nm. **b**, The corresponding magnetic field dependence of I_c calculated with Eq. 5.6 (red), which roughly fits the experimental data (green).

One major difference between the expected and the measured magnetic field dependence of I_c is that in expected Fraunhofer patterns, I_c dips to zero or comes very close to zero for certain magnetic field values, whereas experimental data always have a background I_c that prevents the total I_c from reaching zero. We attribute this background I_c to the NbN weak link in the junction, which has a stronger screening effect and experiences a smaller magnetic field compared with the rest of the sample. There is unlike narrow junction 1: even though weak link is dominant such that oscillations are suppressed, Fraunhofer oscillations are still present on top of a background current, as seen from in Fig. 5.9b and Fig. 5.9c .

There are only two ways to live your life. One is as though nothing is a miracle. The other is as though everything is a miracle.

Albert Einstein

6

Tunneling in proximitized quantum Hall 1D wire

As discussed in Chapter 1, the presence of a Majorana zero energy mode at the end of a 1D proximitized superconducting wire gives a distinct tunneling signature. In this chapter, we will discuss tunneling measurement using quantum Hall edge states as a probe.

6.1 Quantum Hall states as a tunneling probe

While the experimental setup for tunneling measurement in proximitized semiconducting nanowires [1,25] is straightforward, in a proximitized $\nu = 1$ quantum Hall hybrid structure (the dotted box in Fig. 6.1) a separate tunneling probe cannot be fabricated because the probe itself would give rise to unwanted gating in the sample. To avoid this problem, tunneling is directly probed using quantum Hall edge states.

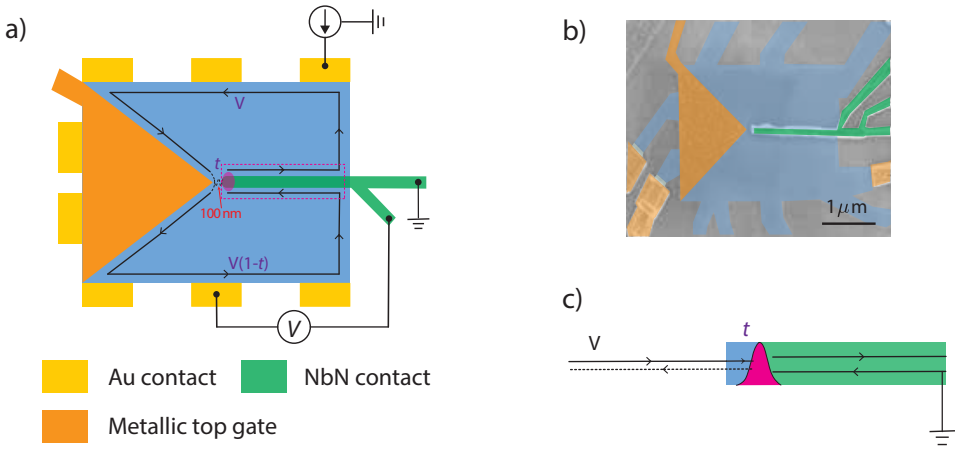

Figure 6.1: Tunneling measurement with quantum Hall edge states. **a**, The measurement schematic with quantum Hall edge states. **b**, A false-colored SEM image of a graphite-gated tunneling device. The darker-blue region is on top of a graphite back gate. Most metallic contacts are not shown because the device is contacted further out from the effective device area. **c**, Side view of the tunneling of the quantum Hall edge state on the left to the zero energy mode at the end of quantum Hall-NbN hybrid structure through Andreev reflection.

As shown in Fig. 6.1a, the devices have triangularly shaped metallic top gates, some devices also have a graphite back gate for the entire device as shown in the SEM image in Fig. 6.1b (fabrication details can be found in Appendix A). The data reported in this dissertation is based on a non-graphite gated device.

The back and top gates are tuned separately, so that the dual-gated region is at $\nu = 0$ and the rest of the device is at $\nu = 1$. A dc current is sourced from one of the top electrodes, with the edge state

being at potential V. The current is subsequently drained through the NbN superconductor. After the edge state travels around the device and comes to the closest distance with the NbN contact (in the middle of the device where the top gate is the closest to the NbN contact), it can tunnel into the NbN contact and get drained. Assuming that this happens with a probability t, then the edge states continue onto the lower part of the graphene with a probability $1 - t$. Consequently, the potential of the edges on the lower part of the graphene will be $V(1 - t)$. Having both a top gate and a back gate allows us to tune the coupling (i.e. the probability t) between the edge states around the top gate and the NbN contact.

The existence of a Majorana zero mode at the end of the quantum Hall-NbN structure will result in an enhanced t when the quantum Hall edge state is at a zero dc bias with respect to the NbN superconductor (Fig. 6.1c), as discussed in Chapter 1. This in turn leads to a depression in the downstream measured voltage. Therefore, in contrast to the case of a proximitized semiconducting nanowire, the experimental signature to look for is a "zero-bias-dip" in a tunneling measurement. In other words, a quantized zero-bias conductance peak in a nanowire translates to the tunneling probability being unity ($t = 1$) in the quantum Hall-NbN setup, which is a consequence of perfect Andreev reflection. As a result, the voltage measured downstream becomes zero.

The actual device has a dimension of 1.8 μm by 1.3 μm, with both the nearest distance between the top gate and the NbN, as well as the width of the NbN finger, being about 100 nm. Given that the crossed Andreev reflection could be important in the formation of Majorana fermions in such a structure [3,10], the width of NbN was designed to be on the same order with the coherence of NbN in graphene.

6.2 Gate dependence of graphene at zero magnetic field

The gate dependence of the sample in the absence of a magnetic field is shown in Fig. 6.2. In Fig. 6.2a, the voltage was measured across the back-gate only region and the dual-gated region. The gate dependence of the dual-gated region are the two diagonal lines in Fig. 6.2a. The lines are doubled due to the charge inhomogeneity in the sample.

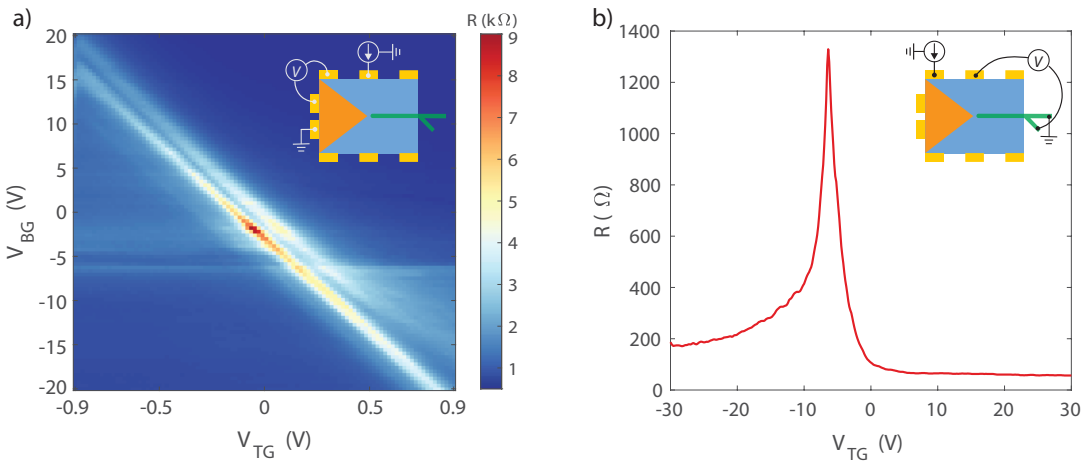

Figure 6.2: Gate dependence of graphene under the influence of **a**, both the top gate and the back gate, and **b**, only the back gate, measured in the absence of an external magnetic field at a temperature of 1.5 K.

In addition, the charge neutrality point of the back-gate only region shows up as horizontal features in the dual-gate scan in Fig. 6.2a, which in this measurement is around $V_{BG} = -6.3$V. This can also be verified by measuring with normal contacts on the back-gate only region (Fig. 6.2b).

Moreover, in the dual-gate scan in Fig. 6.2a, the resistance increases when the dual-gated region and the back-gate only region are tuned to be p- and n- doped respectively, due to the formation of a p-n junction at the interface (upper left-hand corner and lower right-hand corner in Fig. 6.2a).

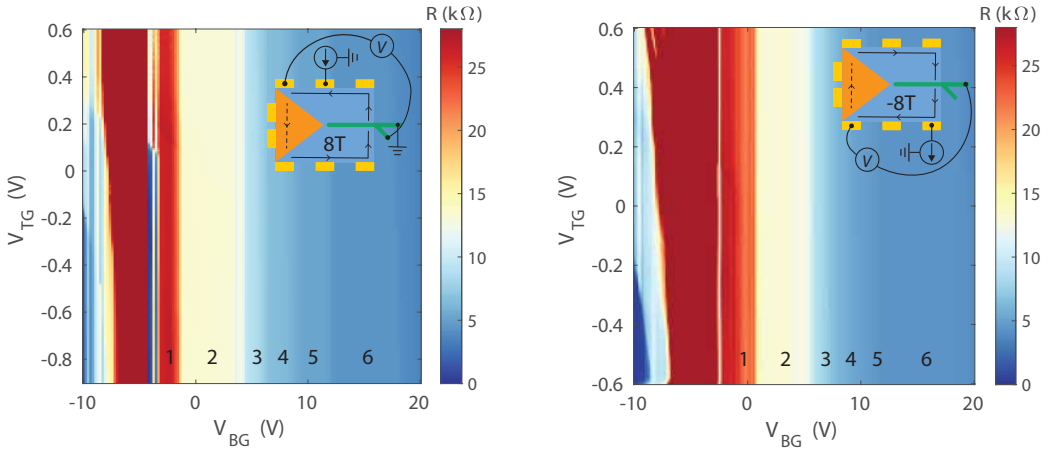

Figure 6.3: Quantum Hall measurement of the back gated region at 8 T (left) and −8 T (right). As expected, there is no dependence on the top gate, and the shift in back gate values at ±8 T shows the charge inhomogeneity in the sample.

6.3 Quantum Hall states inside and outside the dual-gated region

The quantum Hall states in the back-gate only region was measured in a 3-terminal measurement setup, which gives an R_{xy}-like reading when the graphene bulk is in the incompressible state. The results, measured at 8 T with filling factors labelled, are shown in Fig. 6.3. As expected, the filling factors only depend on the back gate, and the charge inhomogeneity is also apparent from the shift in corresponding back gate values because opposite sides of the sample were measured in opposite magnetic fields.

The zero-bias tunneling of the quantum Hall states were studied with both voltage (Fig. 6.4a and Fig. 6.4b) and current measurements (Fig. 6.4c and Fig. 6.4d). The voltage measurement scheme was introduced in section 6.1, and the current measurement follows a similar reasoning: the current is sourced from one of the contacts "upstream" of the quantum Hall states, and drained from both the NbN contact and one of the normal contacts "downstream" of the quantum Hall states with the drained current measured, as shown in the inset in Fig. 6.4. For this particular chirality of quantum Hall states at 8 T, more electron tunneling into the NbN electrode means that there are fewer

electrons reaching the normal contact downstream. As shown in Fig. 6.4b and Fig. 6.4c, the total current measured at the NbN electrode and the normal electrode adds up to a constant of approximately 50 nA, the actual current used in the experiment.

In the most general case, if we do not consider the potential barrier at the boundary between the top gate and the outside graphene, then the edge state from the source will travel along the left edge of the top gate to the downstream contact without coming into close proximity with the NbN electrode, when the filling factor inside the dual-gated region is larger than or equal to the filling factor outside. If the filling factor within the top gate is smaller, or if the inside and the outside of the dual-gated region are doped with opposite types of charge carriers, then there will be one or more edge states going along the slanted edges of the top gate to the contact downstream. As a result, tunneling can happen when the edge states come close to the NbN contact. However, the current flow can be more complicated when graphene bulk is in a compressible state because current would drain through both the NbN electrode and the normal electrode downstream.

Contrary to the ideal situation, there is always some current going directly into the NbN contact without reaching the downstream normal contact. This can be seen from the voltage measurement Fig. 6.4a and Fig. 6.4b where the downstream voltage is always slightly smaller than the upstream voltage, or more directly from current measurement Fig. 6.4c and Fig. 6.4d, showing a non-zero current drained through NbN throughout the measured phase space. This could be due to the presence of graphene compressible states in the bulk, or that the potential barrier at the boundary between the dual-gated region and the back-gate only region is large enough to ensure that a portion of the current does not enter the dual-gated region and gets drained at the NbN contact.

The filling factors outside of the dual-gated region can be identified through the vertical features in a dual-gate scan such as those in Fig. 6.4a and Fig. 6.4b. The filling factors under the top gate manifest themselves as diagonal features. The filling factors are labelled in Fig. 6.4d as $\left(\nu_{\text{back-gate only}}, \nu_{\text{dual-gated}}\right)$. Note that the filling factor of the back-gate only region is taken to be the

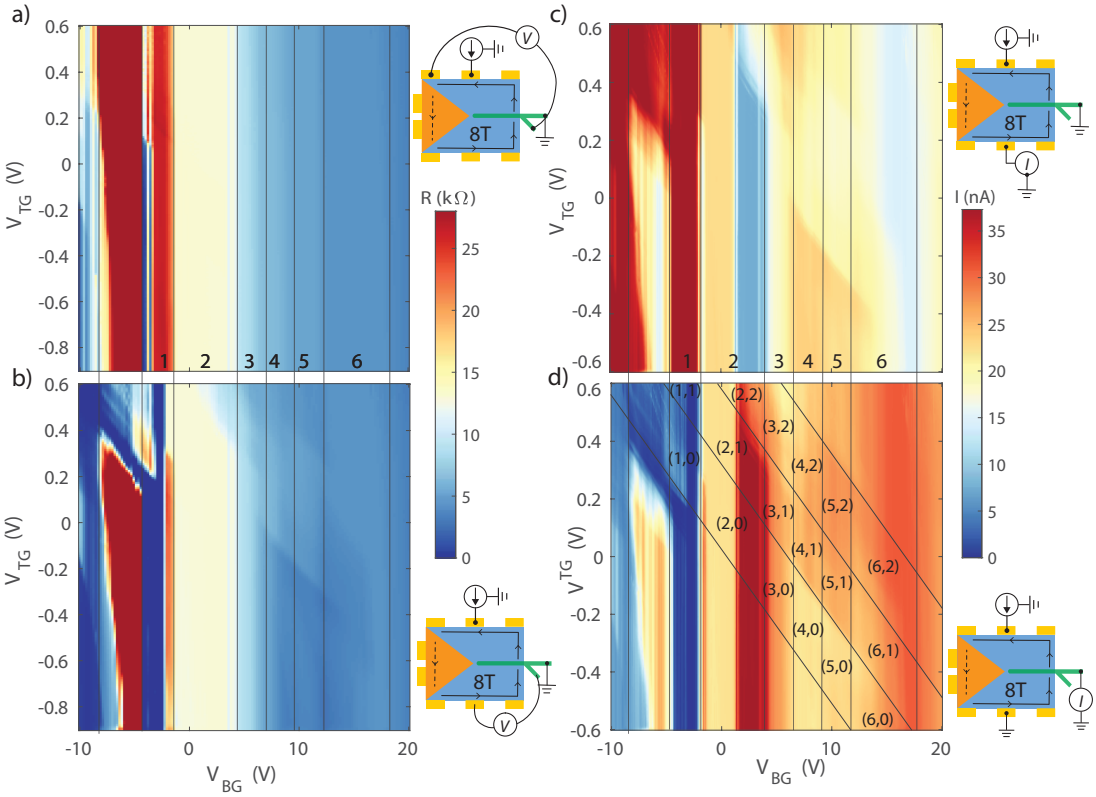

Figure 6.4: Quantum Hall and zero-bias tunneling measurement with voltage probes (**a** and **b**), and current probes (**c** and **d**) at 8 T, 1 K. The quantum Hall edge states flow in a counterclockwise direction. The exact current path in the dual-gated region depends on both top gate and the back gate, which affects the amount of current drained downstream of the constriction, which in turn exhibits itself in both voltage and current measurement. The filling factors in **d** are labeled as $(\nu_{\text{back-gate only}}, \nu_{\text{dual-gated}})$.

filling factor close to the upper normal contact, because the lower part of the graphene has a slightly different filling factor due to charge inhomogeneity in this sample. If we zoom into the region $(2, 0)$ in Fig. 6.4d, then only the right half of the vertical strip with a higher current corresponds to the back-gate region everywhere being at $\nu = 2$, while the left half of the vertical strip is in fact where the upper half of the graphene is at $\nu = 2$ and the lower half at $\nu = 1$, resulting in less current drained through the normal contact downstream.

For consistency, the same measurement was repeated at -8 T, and filling factors identified in Fig. 6.5. Here the nominal filling factor for the back-gate only region is the filling factor of the lower half of the graphene at -8 T.

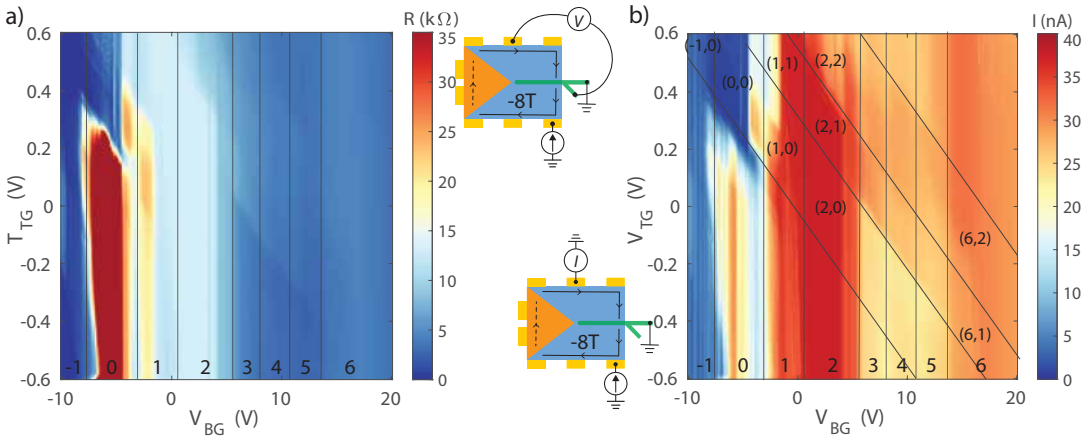

Figure 6.5: Quantum Hall and tunneling measurement at -8 T and 1.5 K. The quantum Hall edge states flow in a clockwise direction. Current is sourced from the bottom-right normal contact, and drained from the NbN contact. **a**, Voltage between a downstream normal contact and the ground. **b**, Current is drained from a downstream normal contact in addition to NbN and measured.

If we disregard the potential barrier for the edge states to enter the dual-gated region from the outside in the measurement setup shown in Fig. 6.5d, then when $\nu_{\text{dual-gated}} \geqslant \nu_{\text{back-gate only}}$, most of the current will be drained through the normal contact, which is what was measured in Fig. 6.5d. However, if we keep $\nu_{\text{back-gate only}}$ fixed and increase $\nu_{\text{dual-gated}}$, i.e. tracing the data in a vertical manner in Fig. 6.5, then we can see that the current going into to the downstream normal contact de-

creases when both regions are positively gated, such as in the case of going from $(1, 0)$ to $(1, 1)$, and from $(2, 1)$ to $(2, 2)$. From this observation, we know that the potential barrier at the boundary between the dual-gated region and the outside is not negligible, so that some current always goes around the dual-gated region, and could get drained through the NbN at the top gate-NbN constriction. Following this reasoning, when there are more edge states on the outside (a larger ν for the back-gate only region), then the inner states get pushed more and more towards the NbN contact at the top gate-NbN constriction and enters the NbN contact more easily. Thus, for $\nu_{\text{back-gate only}} \geqslant 2$, the current reaching the downstream normal drain significantly decreases.

Furthermore, if we examine two of the diagonal sections where $\nu_{\text{dual-gated}}$ is 1 or 2, and $\nu_{\text{back-gate only}}$ increases from 3 to 5, then the current drained through the downstream normal contact decreases, which is consistent with the hypothesis that the additional edge states are drained at NbN due to their proximity with the NbN contact. In addition, for $\nu_{\text{back-gate only}} = 6$, more current is drained from the downstream normal contact compared to when $\nu_{\text{back-gate only}}$ is 3, 4, or 5. This could be due to the fact that $\nu = 6$ is a better developed quantum Hall state (fewer compressible states in the bulk), so that more edge states entered the dual-gated region and reached the downstream normal contact without having to go through the top gate-NbN constriction.

6.4 Bias-dependent tunneling in the quantum Hall regime

After identifying the filling factors inside and outside of the dual-gated regions, we investigated tunneling as a function of an applied dc voltage. The region of interest is $\left(\nu_{\text{back-gate only}}, \nu_{\text{dual-gated}}\right) = (1, 0)$, which corresponds to the scenario illustrated in Fig. 6.1a. If a Majorana zero-energy state appears at the end of the ($\nu = 1$)-NbN 1D hybrid structure, then the downstream voltage measured with respect to the ground will exhibit a zero-bias dip.

The data that we will present in this section were collected at a magnetic field of -8 T (clockwise

chirality for quantum Hall states) and at a temperature of 1.5 K. Note that at this temperature the thermal energy is likely to be dominant and will potentially wash out any experimental signatures given by the Majorana zero energy mode. Nevertheless, it provides a benchmark in assessing similar tunneling devices and also provides hints for future measurements.

Quantum Hall upstream voltage is shown in Fig. 6.6a and Fig. 6.6b, with the corresponding downstream voltage shown in Fig. 6.6c and Fig. 6.6d. During the measurement, the top gate was fixed at 0.2 V while the back gate was scanned over the range of -2.31 V to 0.854 V, such that the outside region was held at $\nu = 1$ and the top gated region at $\nu = 0$.

For such a setup, the quantum Hall state from the outside would not enter the $\nu = 0$ dual-gated region but would instead travel along the slanted edge around it. The downstream voltage normalized by current was about 25 kΩ at zero bias, indicating that the tunneling between the quantum Hall states at the tip of the top gate and the NbN contact was minimal. As the applied bias slightly increases, the downstream resistance starts to drop, as a result of more tunneling into NbN quasiparticle states when the energy of the incoming electron increases. As the applied bias increased further beyond 50 nA, which roughly corresponds to a voltage of 1.3 mV, the $\nu = 1$ quantum Hall state starts to break down (Fig. 6.6a and Fig. 6.6b) as the energy of the incoming electrons becomes comparable to the gap of the quantum Hall states.

For a back gate voltage larger than -1.5 V, the downstream voltage (Fig. 6.6c and Fig. 6.6d) dropped to about 12 kΩ, as the upper half of the graphene transitioned into $\nu = 2$, while the lower half of the graphene was still at $\nu = 1$, consistent with the charge inhomogeneity observed in other measurement of the same device.

The bias was also scanned over a smaller range with a higher resolution, and no signature of any Majorana bound state was detected. Similar tunneling measurement was also performed on filling factors $(1,1)$, $(2,2)$, $(2,1)$, $(1,1)$, with similar results being observed.

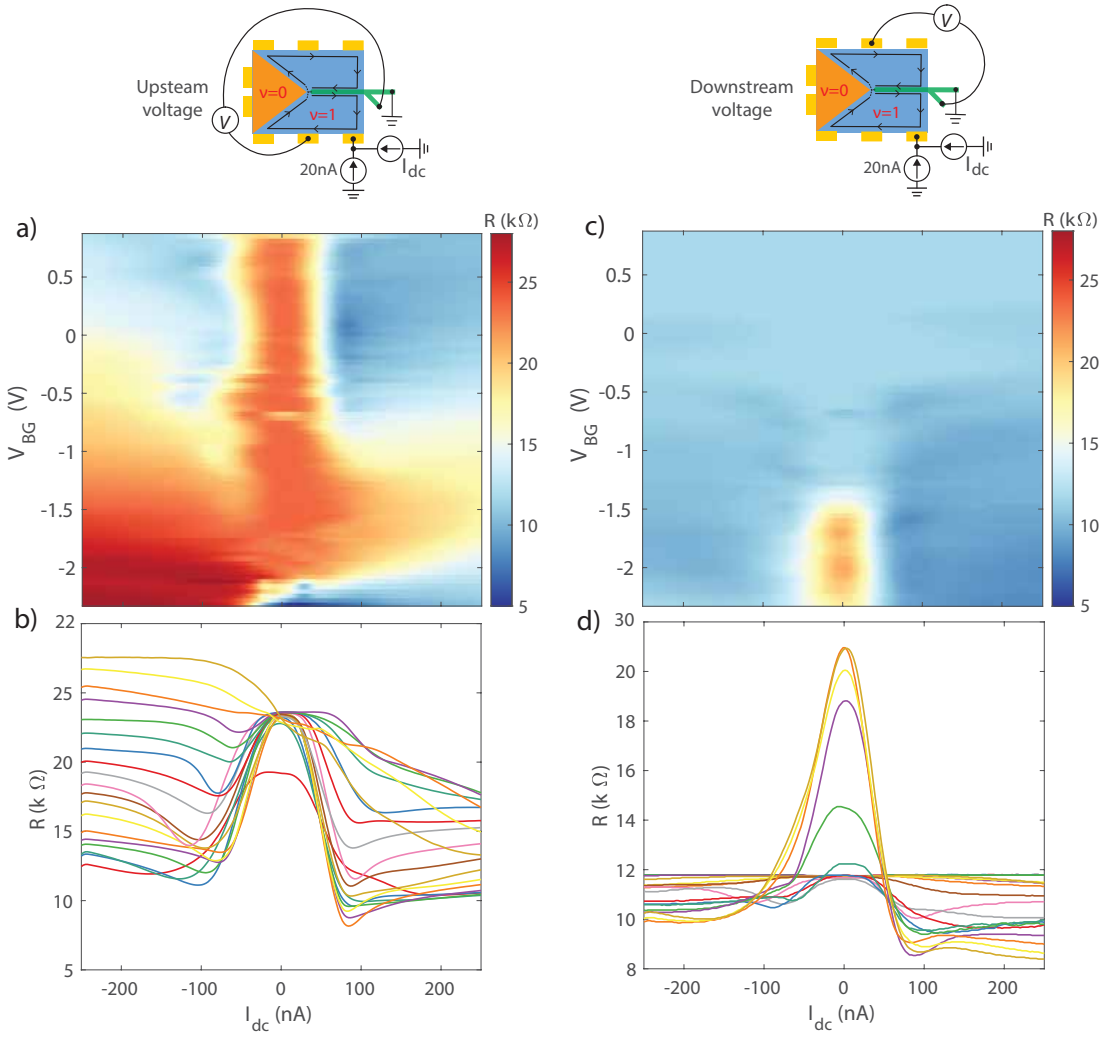

Figure 6.6: Tunneling measurement with $(\nu_{\text{back-gate only}}, \nu_{\text{dual-gated}}) = (1, 0)$ at a magnetic field of -8 T and a temperature of 1.5 K. The top gate was kept constant at 0.2 V during the measurement, and the back gate varied. **a** and **b**, Quantum Hall upstream resistance. **c** and **d**, Quantum Hall downstream resistance. For V_{BG} greater than about -1.5 V, the upper half of graphene becomes $\nu = 2$ while the lower half of graphene remains at $\nu = 1$. The quantum Hall gap is estimated to be about 1.3 meV from the upstream measurement, and no Majorana-like tunneling signature was observed. The line plots in **b** and **d** are sampled from the entire back gate range scanned in **a** and c from -2.31 V to 0.854 V in steps of 0.12 V.

6.5 Magnetic field dependent tunneling at $\nu = 0$

The tunneling data from $(\nu_{\text{back-gate only}}, \nu_{\text{dual-gated}}) = (1, 0)$ in the previous section suggest that the tunneling of $\nu = 1$ from just outside the tip on the right side of the top gate to NbN was not significant. To independently investigate the tunneling behavior between the dual-gated graphene and the NbN, graphene outside of the top gate was kept at $\nu = 0$, while the top gate was kept at 1.5 V (equivalent to a back gate of roughly 33 V and a charge density of 2.4×10^{12} cm^{-2}). The tunneling was measured between one of the contacts in the dual-gated region and the NbN contact.

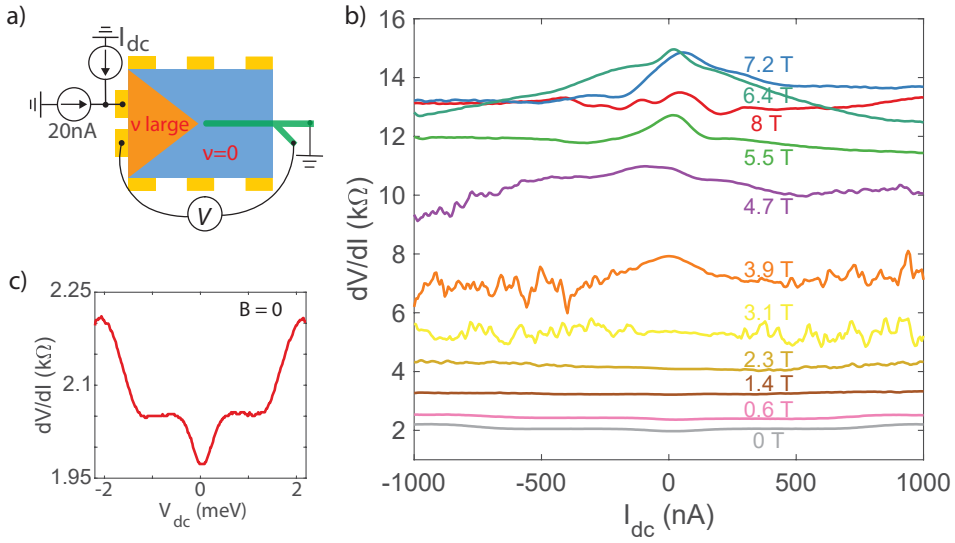

Figure 6.7: Field-dependent tunneling in the absence of quantum Hall edge states. **a**, The dual-gated region is kept at a highly doped regime while the rest of the sample is kept at $\nu = 0$. **b**, The junction resistance as a function of dc current at varying magnetic fields. While resistance peaks were observed at higher magnetic fields, conductance enhancement was seen in **c** as a result of Andreev reflection. The voltage across the junction was also independently measured in Fig. 6.8.

Fig. 6.7 shows the tunneling resistance measured as a function of the applied dc current and external magnetic field. The corresponding voltage difference between the tunneling probes is also measured and shown in Fig. 6.8.

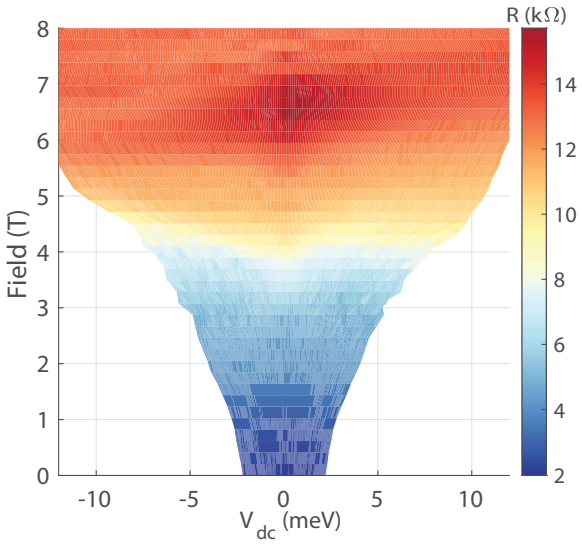

Figure 6.8: Same measurement as in Fig. 6.7, with the voltage across the junction measured.

The results from the field dependent measurement (Fig. 6.7b and Fig. 6.8) can be roughly separated into high-field and low-field regimes. At relatively high magnetic fields, a tunneling resistance peak develops when the dc voltage across the junction is within 1 meV. As the magnetic field decreases, the tunneling resistance peak decreases in height and eventually disappears. This is expected as the probability of Andreev reflection increases with decreasing magnetic field. The enhancement in conductance can be seen in Fig. 6.7c, where 2 meV agrees with the size of the NbN, as one would expect, with a tunneling resistance of about 2 kΩ. The same trend is also evident in the tunneling resistance vs. voltage plot in Fig. 6.8. The relative small value of tunneling resistance can be related to the charge inhomogeneity in the sample, in which conducting channels exist when most of the graphene is at $\nu = 0$.

7

Conclusion

To investigate the coupling between quantum Hall edge states and superconductivity, Josephson junctions and tunneling devices were studied in graphene-NbN 2D systems. The observation of stepped increment in the critical current of narrow Josephson junctions (Chapter 3), and its corresponding absence in the wide junction (Chapter 4), confirmed that the Josephson current can be mediated by quantum Hall edge states through the process of crossed Andreev reflection. In addition, quantum Hall edge states can also be used as a tunneling probe in quantum Hall-NbN

structures to directly verify the existence of a zero energy mode (Chapter 6).

Graphene-superconductor hybrid structures are emerging as an important platform in the creation and manipulation of Majorana zero modes and other anyonic states. With improved fabrication techniques, such as graphite back gate and selective etching, high quality integer and fractional quantum Hall states are being achieved at increasingly lower magnetic fields in graphene devices. We anticipate that this work will inspire more experimental and theoretical studies on the interplay between quantum Hall states and conventional superconductivity in 2D material systems, and the realization of braiding of anyons in such systems.

A

Device fabrication

All of the devices described in this dissertation consist of a basic structure of graphene encapsulated by top and bottom hexagonal boron nitride (hBN) layers. Back gate is applied either from the back side of the wafer with 285 nm of SiO_2 acting as the dielectric, or at graphite with hBN as the dielectric. Top gate is also applied in a similar manner.

A.1 Exfoliation

Graphene and hBN were obtained through exfoliating graphite and hBN crystals with 3M Scotch™ magic tapes (Scotch tape) on clean, untreated Si wafers with 285 nm chlorinated thermal oxide. Monolayer graphene and hBN of appropriate thicknesses were searched and identified under the optical microscope based on their optical contrast. The cleanliness of graphene and hBN were further verified by Atomic Force Microscopy (AFM) to ensure that the flakes are free of glue residues and microscopic folds and creases.

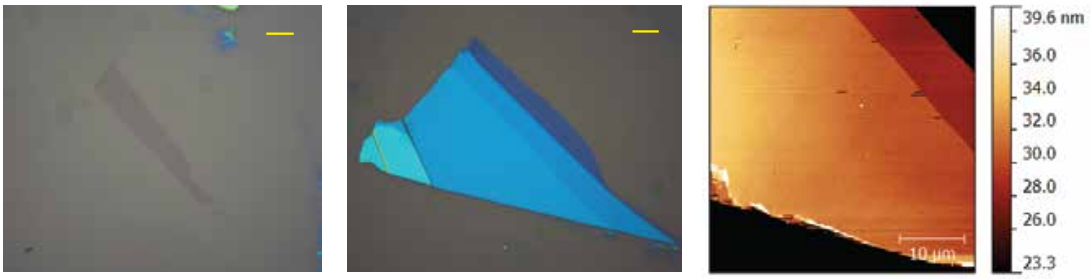

Figure A.1: Optical and atomic force microscope (AFM) images of graphene and hBN. Scale bar: 10μm. Left: An optical image of a monolayer graphene. Middle: An optical image of hBN of a thickness 28μm. Right: An AFM image of a 35μm by 35μm area of the same hBN sample, showing the smoothness of the surface.

Earlier exfoliation processes also included an extra step of cleaning the substrate with pirahna solution (1 part of 30% aqueous H_2O_2 and 3 parts of H_2SO_4), before exfoliating flakes onto the substrate. However, in practice pirahna solution cleaning did not consistently produce cleaner flakes as seen from AFM measurements, nor did it give better quality of quantum Hall measurement in graphene devices. This hazardous pre-cleaning step was therefore abandoned.

Other types of adhesives (blue tape, or dicing tape widely used in semiconductor industry) are also used for exfoliation by other people, with heat being applied at different stages during the exfoliation to alter the adhesiveness of the tape. In general, less adhesiveness in the tape results in less glue residue on the flakes but also a lower yield of flakes per exfoliation, and the author prefers

scotch tapes.

In addition, the surface adhesiveness of the SiO_2 substrate can be enhanced with oxygen plasma before the exfoliation, which generally produces larger flakes from subsequent exfoliation. However, depending on the polymer used for dry transfer, the flake might become very difficult or impossible to pick up when exfoliated onto a oxygen plasma-treated substrate.

A.2 Stacking with dry transfer

The 2D restructures were stacked layer by layer following the method outlined in Wang, 2013[41]. The transfer stamp was made by having a layer of polypropylene carbonate (PPC) on top of polydimethylsiloxane (PDMS), held in place by Scotch tape. PPC was spun on clean Si wafers to produce thin PPC films. These films would later be peeled off from the Si substrate with a piece of Scotch tape (Fig. A.2). The recipes for making PPC and PDMS are listed at the end of this chapter.

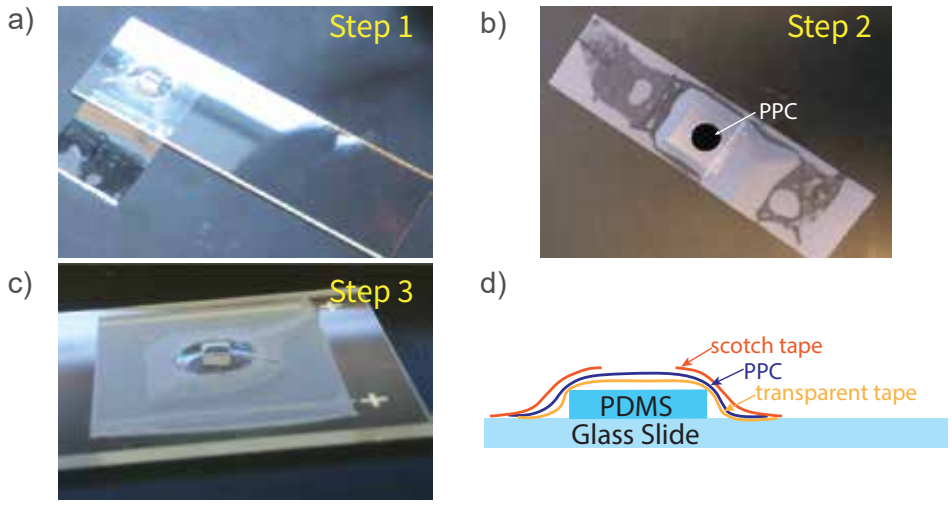

Figure A.2: Steps for making a transfer stamp. **a**, A square piece of PDMS was held in place on one end of a glass slide by a piece of transparent tape. **b**, Pre-spun PPC film was peeled offed from the Si substrate with a piece of Scotch tape with a hole in the middle. **c**, The PPC from **b**, was placed on top of the Scotch tape-PDMS structure assembled in **a**. **d**, a cross section of the transfer stamp; PPC was allowed to contact the flakes through the hole made on the Scotch tape.

The transfer is done on a motorized transfer stage with heating and cooling capabilities (Fig. A.3). The Si substrate is placed on the transfer stage, held in place by vacuum. The transfer stamp is mounted onto the motorized transfer arm, and comes into contact with the first layer (topmost layer of the final stack) at about 29 °C, slightly above the room temperature. To minimize air bubbles trapped in between layers of 2D materials, contact between the stamp and the flake is slow and carefully controlled with a combination of downward mechanical movement of the transfer arm and a slow raise in temperature of the transfer stage.

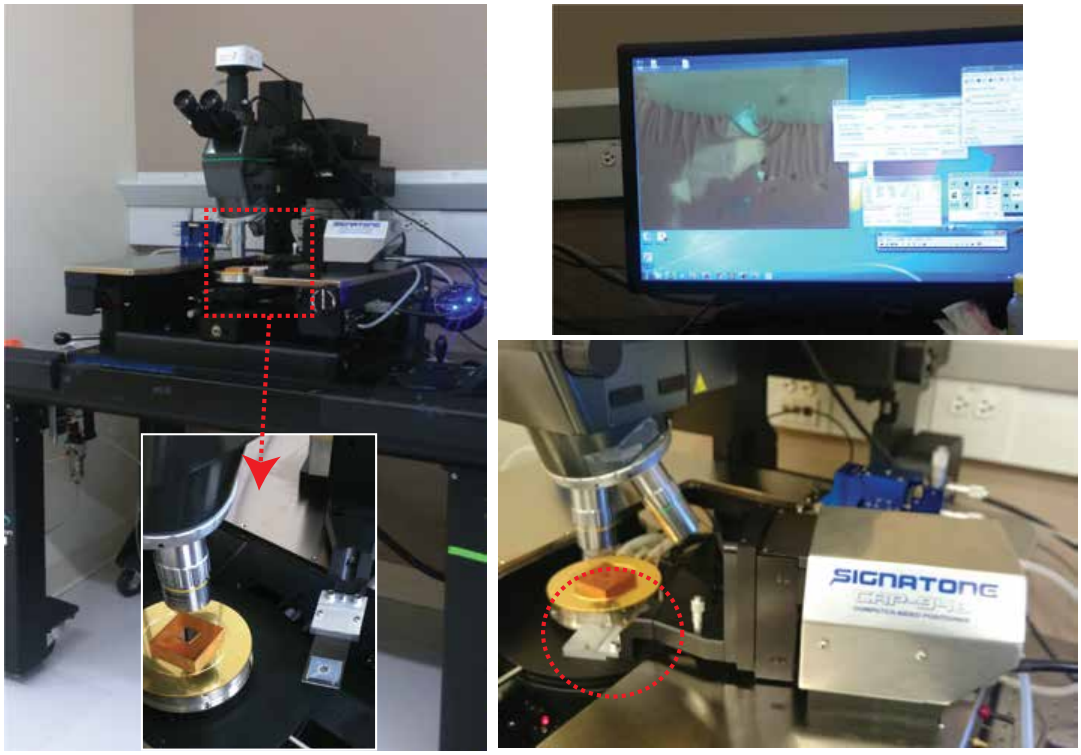

Figure A.3: The transfer stage is placed on an air table for vibration isolation, with the substrate held in place onto a vacuum chuck during the transfer. The transfer arm holding the transfer stamp is a computer-aided, fully motorized positioner used on probe stations, fitted with a metal glass slide holder machined in-house. The entire transfer process can be monitored and controlled from a computer.

Once the PPC (or the bottom most flake already picked up on PPC) has made good contact with

the flake on the substrate, the transfer arm is slowly lifted up to pick up the flake from the substrate. The temperature is either kept at about 50°C for a "hot" pick-up or cooled down to about 29°C for a "cold" pick-up. PPC becomes more fluid-like at higher temperatures and can be disengaged from the substrate at a much slower rate than when it is cold, making "hot" pick-up suitable for a slow pick-up. On the other hand, for a relatively fast pick-up, cold-pick up produces better results. Ultimately, the temperature and the speed one uses during a transfer depend on the material being transferred, and is also largely a matter of personal preference. The author usually used cold pick-up for picking up the topmost layer and hot pick-up for subsequent layers, with exact temperatures adjusted based on the situation.

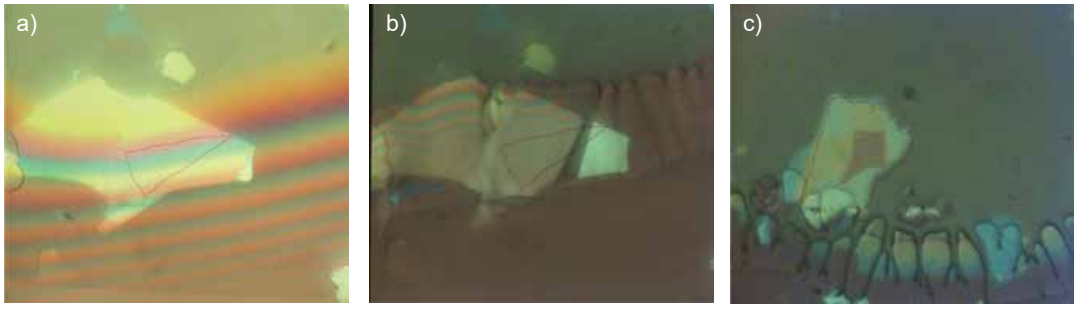

Figure A.4: Dry transfer with PPC. **a**, Thermal contact between the top hBN picked up on the PPC and the graphene on the substrate. **b**, Hot pick-up at 55°C. **c**, Releasing the stack onto the substrate by lifting up the transfer stamp at 95°C.

Once the stack has been assembled in the correct order on the transfer stamp, one has to disengage the stack and the PPC in order to deposit the stack onto the substrate. After the stamp holding the stack is in full contact with the substrate, the temperature is slowly raised to at least 95°C so that the PPC starts to melt. The transfer arm is then very slowly raised up, leaving the stack on the substrate. The stack is then cleaned with acetone and isopropanol (IPA), and vacuum annealed at 350°C for 15 minutes.

Before nanofabrication, the stacks are checked under the AFM to identify areas with folds and bubbles so that these areas can be avoided when making a device.

A.3 Nanofabrication

For fabrication, alignment marks were first deposited around the stack, and the device was then designed in DesignCAD with optical and sometimes AFM images of the stack with alignment marks. Reactive ion etching (RIE) with CHF_3 and O_2 was used to etch hBN while O_2 plasma (oxygen plasma) alone was used to etch graphite. The order of fabrication steps are usually not of critical importance but careful planning of the fabrication is required for more complicated layer structures. Here we outline the fabrication steps for the tunneling device discussed in Chapter 6, with both a top and a bottom graphite gate.

Graphite back gate was first pre-patterned and etched with a poly(methyl methacrylate) (PMMA) mask, followed by vacuum annealing at 350°C for 15 minutes. The previously-assembled top layers of the final stack were aligned and deposited on top of the graphite gate with dry transfer. The graphene was intentionally chosen to be larger than the graphite gate, so that the metallic 1D contact could be made outside of the boundary of the graphite back gate, avoiding the need for selective-etching (i.e. etching through only the graphene for contact but not the bottom hBN, so that the metallic contact would not short onto the bottom graphite gate).

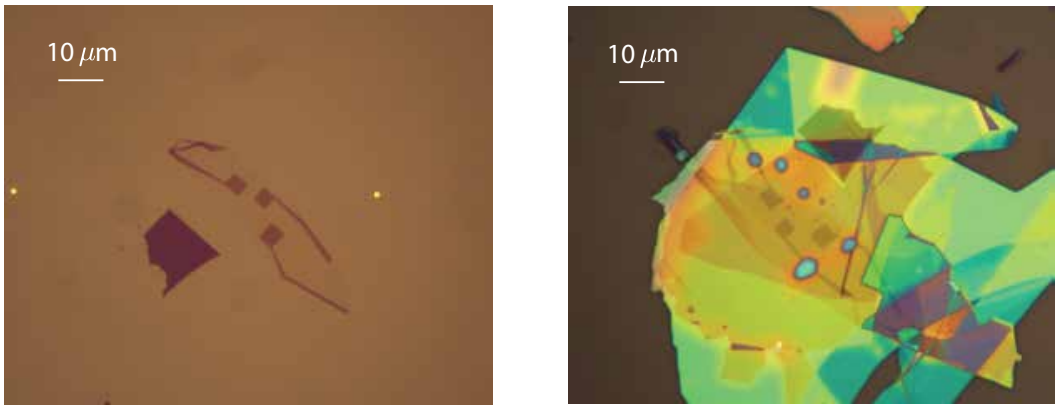

Figure A.5: Transferring a stack onto a pre-patterned graphite back gate. Left: Pre-patterned graphite back gate. The gold squares are alignment marks. Right: The entire stack after transferring the top layers onto the pre-patterned gate.

PMMA mask was used in an O_2 RIE etch to define the graphite top gate. O_2 etches graphite at a much faster rate than hBN; as the etching rate varies in the RIE etcher, gentle etching cycles were repeated as necessary to ensure that the top hBN was not etched through to expose the graphene underneath it. Alternatively, if a metallic top gate was used, chromium/palladium/gold (Cr/Pd/Au) would be evaporated via thermal evaporation as the first fabrication step.

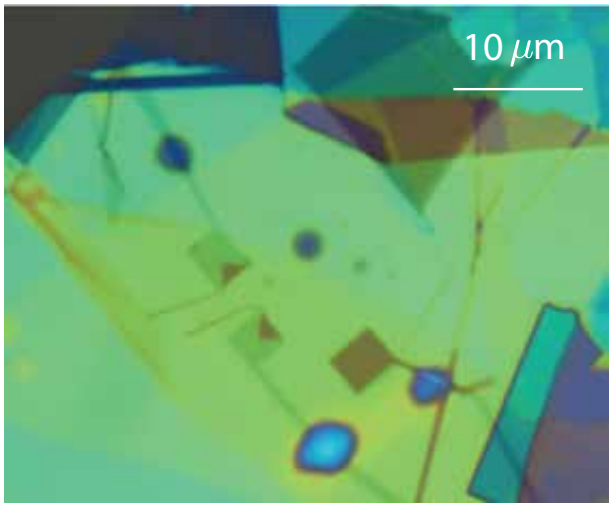

Figure A.6: Selective etch of the graphite top gate. Oxygen plasma was used to etch only the top gate, which is the triangular shaped structures in the two devices on the left, and the rectangular structure on the right. Similar to the graphite back gate, a "leg" extending out from each top gate was left to allow easier metallic contact at a later step.

Next, the NbN contact was made with the same PMMA mask for etching and sputtering. Due to the presence of a graphite back gate, etching has to be controlled so that the graphene would be etched through but not the bottom hBN (otherwise the NbN would short onto the bottom gate and the gate would become useless). In such cases selective etching would usually be done by etching with short bursts of time, with the flake thickness verified under an optical microscope in between etching cycles. However, due to the narrowness of the NbN structure in our devices (100 nm wide), it was not possible to check on rate of etching due to the limited resolution of the optical microscope. Therefore, slightly bigger windows were opened up elsewhere on the stack during the

etch for monitoring the etching rate. However, as the etching rate is non-uniform and tends to be slower for smaller structures, the extra windows only serve as an empirical reference as to how much hBN and graphene might have been etched for NbN contact.

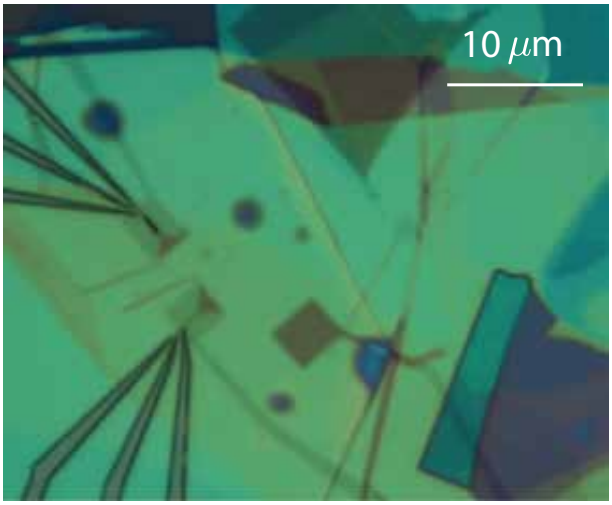

Figure A.7: Sputtering of NbN with *in-situ* etching. The stack was partially etched, exposing graphene edges for 1D contact with NbN, and the bottom hBN preserved to electrically isolate NbN and the bottom graphite gate. Another area of the stack (not shown) was also etched at the same time and used as a reference to monitor the etching rate.

After depositing NbN, the active device area was etched with hydrogen silsesquioxane (HSQ) resist as the etch mask. The boundary of the device was designed to be smaller than the boundary of the graphite back gate, so that after etching through the entire stack including the pre-patterned graphite back gate, the edges of all layers in the heterostructure would end at the same place and automatically be aligned. On the other hand, the places where metallic contacts would be made later were extended out from the main device (Fig. A.8, left), in order to prevent the metallic contact from connecting onto the graphite back gate.

After etching, the metallic contact (including the contact for the top and bottom gate) was deposited in a thermal evaporator. 2 nm of chromium (Cr) and 8 nm of palladium (Pd) were used as the sticking layer, on which gold (Au) was evaporated.

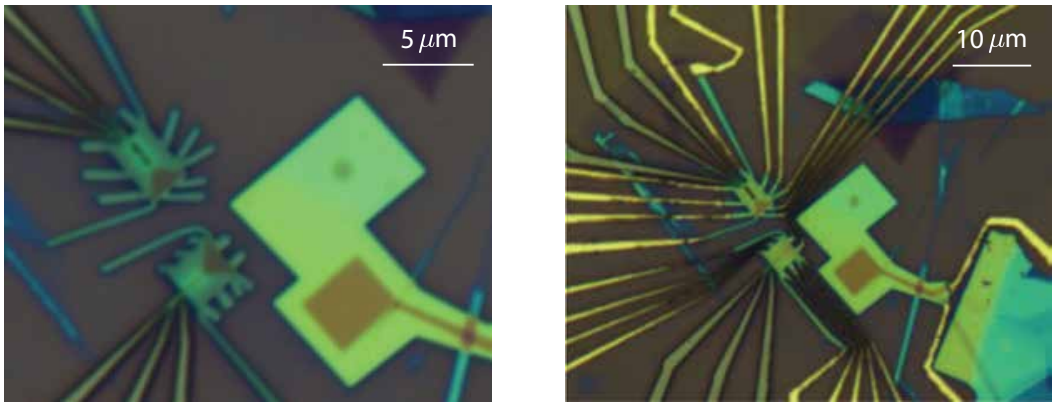

Figure A.8: Device etch and normal contact. Left, two tunneling devices were etched with graphene contact extending beyond the graphite back gate. Right, making metallic contact to both the device and the top and bottom gates.

A.4 Recipes

A.4.1 Polypropylene carbonate (PPC)

PPC solution was made by mixing 15 grams of PPC in 100 mL of anisole, stirring overnight at 160°C in a covered beaker. The solution was allowed to cool to room temperature, then filtered through a syringe containing a 0.2 μm polytetrafluoroethylene (PTFE) membrane with a glass microfiber prefilter.

To make thin PPC films used in dry tranfers, the PPC solution was spun at 3000 rpm on diced Si wafers, and baked at 95°C for 5 minutes. The films were peeled off from the substrate with Scotch tape right before being used, as described in section A.2.

A.4.2 Polydimethylsiloxane (PDMS)

- Prepare a glass petri dish, and lay several glass slides at the bottom
- Cut out smaller squares of glass from additional slides and place them on top and at both ends of the glass slides already laid out in the petri dish. Lay down one more layer of glass

slides at the very top, parallel to the glass slides at the bottom. The smaller pieces of glass squares act as "spacers" so that the top glass slide and the bottom glass slide are always one glass slide thick apart from one another. This would make sure that the PDMS produced in the end would have a uniform thickness throughout.

- Mix the elastomer and curing agent in a 10 : 1 ratio by mass (60 grams and 6 grams for a 100 mm petri dish, or 10 grams and 1 gram for a 60 mm petri dish, respectively).
- Defoam the mixture by centrifuging at 2000 rpm for 1 minute.
- Slowly pour the mixture into the petri dish with glass slides, and avoid forming any bubbles as much as possible.
- Pump on the PDMS mixer in the petri dish in a vacuum desiccator to eliminate bubbles as needed.
- Bake the PDMS mixture in an oven at 65°C for 3 hours
- Slowly and carefully separate the top glass slide from the cured PDMS with a razor blade.

A.4.3 Electron-beam lithography resist

For evaporating metals without *in-situ* etching, a double-layer resist was used to get a better lift-off. A typical recipe is as follows: spin PMMA 495 A4 at 3000 rpm, followed by PMMA 950 A2 at 4000 rpm, with 2 minutes of baking at 180°C after each spin. For processes where reactive ion etching or sputtering is involved, a thicker single layer of PMMA was used.

For etching, HSQ mask was sometimes used as follows: first, spin PMMA 950 A2 at 4000 rpm, bake at 180°C for 2 minutes, then spin HSQ at 4000 rpm.

B

Measurement of the critical current I_c

While almost all of the voltage was measured with a standard lock-in technique, it would be too slow if we want to determine the I_c of the Josephson junctions. In particular, given the small amplitude of the critical current due to quantum Hall edge states, with each increment in step size as small as 25 nA in some cases, we had to take extra care during the measurement.

B.1 Direct DMM or lock-in measurement of I_c

A straightforward way to measure the critical current is to simply measure the voltage drop across the Josephson junction, while applying an increasing dc current (Fig. B.1). The differential resistance dV/dI can also be simultaneously measured with a lock-in amplifier. The advantages of this approach are that: first, the critical current and its dependence on other experimental conditions can be immediately read out; and second, the normal resistance of the Junction is obtained in addition to I_c.

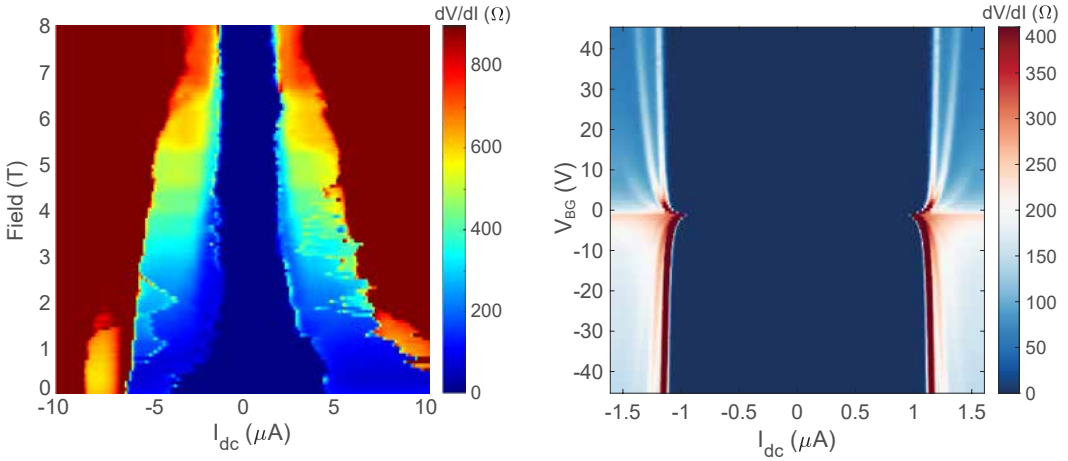

Figure B.1: I_c of narrow junction 2 measured with a DMM and a lock-in amplifier as a function of magnetic field, at a back gate of 40 V and a temperature of 300 mK. The dc current was swept from -10 μA to 10 μA for each measurement. Left: Differential resistance measured with a lock-in. Right: dc voltage drop across the junction measured for selected magnetic fields.

In fact, the modulation of I_c in the quantum Hall regime was first measured with this method (Fig. B.2). However, from Fig. B.2, we can already see the deficiencies in relying on a DMM to measure the dependence of I_c as a function of back gate and magnetic field. First, it is slow, requiring at least one hour to acquire a single plot that only provides information on the critical current as a function of back gate at a single magnetic field. This happens because the voltage across the junction at every value of the dc bias was measured, even though the only important information is the volt-

age just in the vicinity of the switch of the Josephson junction. In addition, the stochasticity in the critical current becomes more prevalent as the magnetic field increases, which makes it increasingly difficult to identify a definite trend from the data (e.g., the 8 T data in Fig. B.2).

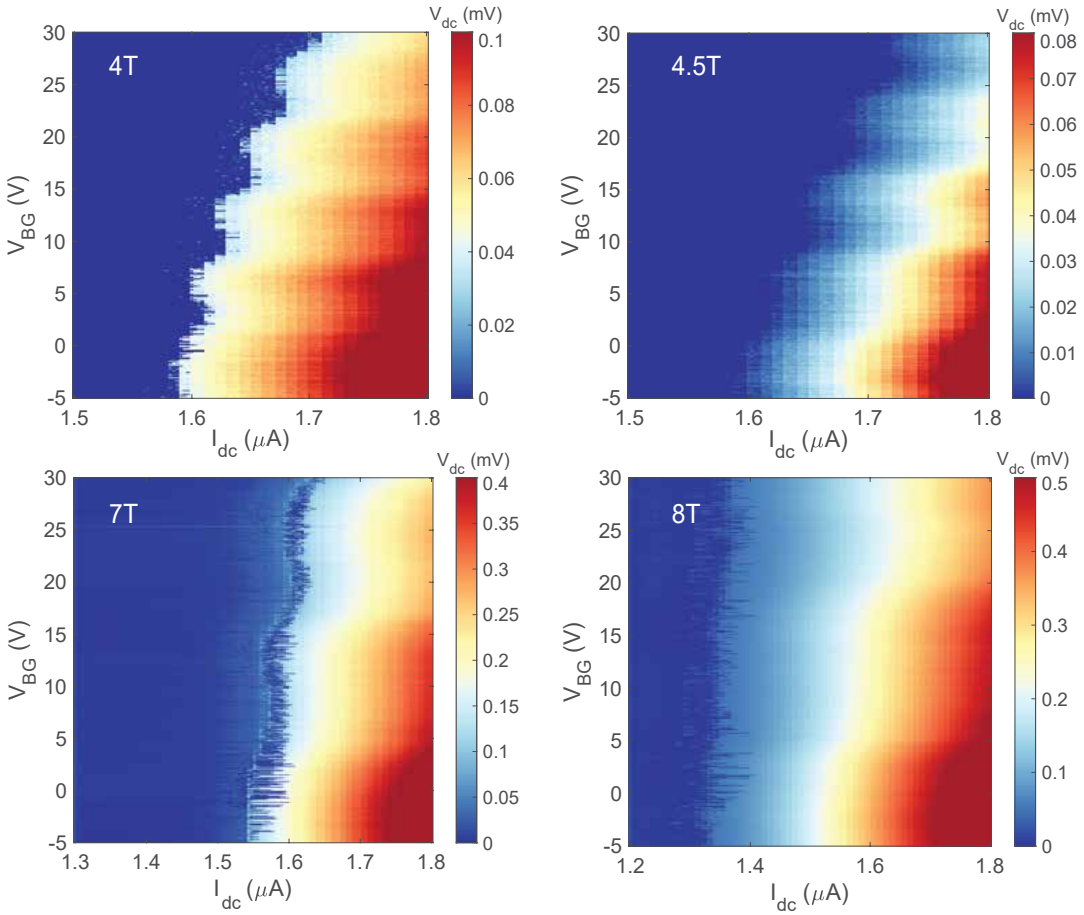

Figure B.2: I_c of narrow junction 2 in the quantum Hall regime, measured with a DMM at selected magnetic fields. While the modulation is clearly visible at lower magnetic fields, the increased stochasticity in I_c makes data interpretation at higher magnetic fields very difficult.

One solution to this problem is to take a several measurements and average the results. However, it turns out that averaging over only a few measurements did not improve the consistency in the I_c measurement. To make a statistically meaningful conclusion, we would need to take thousands of

repeated measurements. Given the prohibitively large amount of time that it would take to obtain the measurement with a DMM, we employed an alternative method to measure I_c.

B.2 A DAQ measurement setup

To perform repeated I_c measurements in a reasonable amount of time, we used a DAQ data acquisition device from National Instruments. The actual sampling rate was about 270000/s limited by the measurement computer, which is about 27k times faster than using a lock-in amplifier with a sensitivity of 0.1 s. Despite being noisier than a lock-in measurement, the DAQ was indispensable in the critical current measurement in our experiment.

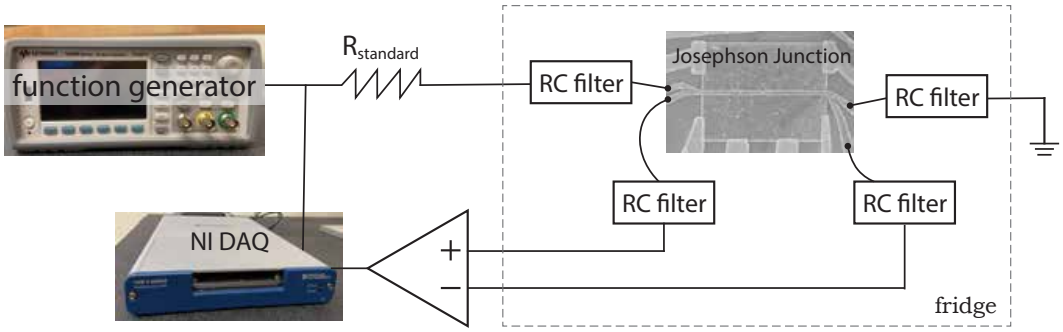

Figure B.3: Measurement scheme with a data acquisition (DAQ) device.

The measurement scheme is shown in Fig. B.3. The function generator outputs a sawtooth voltage signal, which is supplied to the sample through a standard resistor. The dc current going through the sample is thus directly proportional to the voltage generated at the function generator. The DAQ device measures two channels simultaneously: the voltage output of the function generator, and the voltage difference developed across the Josephson junction. The measured voltage would be zero when the dc current is small and switch to a finite value at some dc current. The critical current is then obtained by dividing the voltage read from the function generator with the standard resistor (Fig. B.4a and Fig. B.4b).

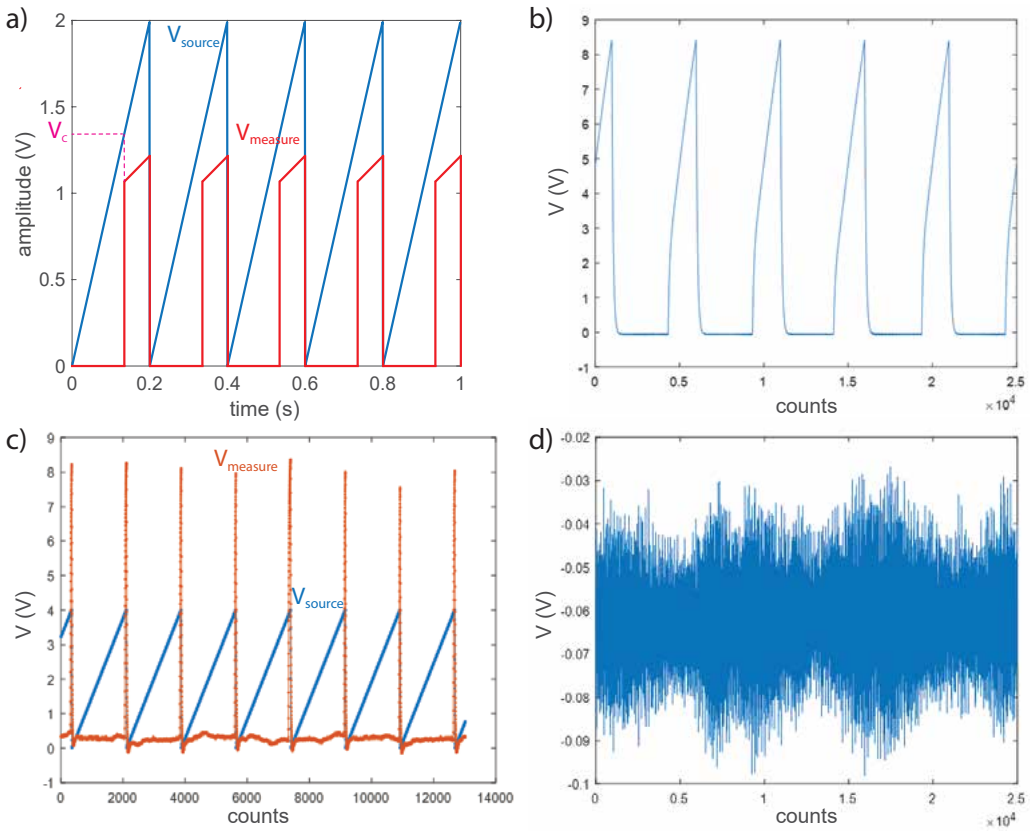

Figure B.4: Voltage profile measured with a DAQ. **a**, Bias voltage and voltage that would develop across the Josephson junction in the ideal situation. **b**, An example of the actual voltage measured across the junction. **c**, Dual-channel voltage signal measured with a DAQ. **d**, Voltage difference (after being amplified) across two terminals that are floated, showing the noise profile.

In reality, the voltage measured across the junction fluctuates due to noise, and experiences loss of signal and measurement artifacts near edges of the sawtooth wave form (Fig. B.4c). The measurement also picks up 60 Hz mains hum from the electrical mains, as shown in the signal measured between the two floated electrodes in Fig. B.4d.

The USB-6351 model of the DAQ supports several measurement modes, and we opted for a differential measurement scheme that measures the voltage difference between the positive and negative inputs, instead of measuring with respect to a common ground. The connection to the DAQ is shown in Fig. B.5, and the positive and negative ends are soldered onto the shell and the core of a BNC connector respectively. The DAQ is then connected to the computer via a USB isolator, ready to be used for measurement.

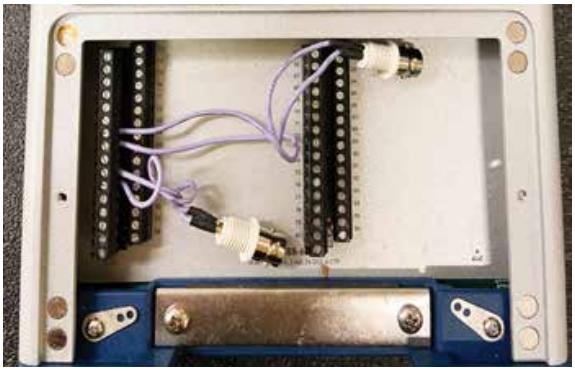

Figure B.5: Wiring connection in the DAQ. Two channels, namely sourced voltage from the function generator and the voltage developed across the Josephson junction were each measured through a differential scheme, where the voltage different between the shell and the core of the BNC cables were recorded by the DAQ.

B.3 Measurement of I_c with DAQ

The DAQ data were acquired through MATLAB, and the other instruments controlled via special measure interface [12].

B.3.1 Frequency, sampling rate and amplitude

The frequency of the sawtooth wave function determines how fast the voltage is swept, and the sampling rate is the number of data points that the DAQ collects every second. The amplitude is that of the sourced voltage. As the sampling rate is hardware limited, a higher frequency speeds up the measurement at the expense of a reduced resolution. In a similar manner, an unnecessarily large amplitude compromises the resolution.

The measurement was performed at either 277 Hz or 447 Hz. The sampling rate was set to 260k – 270k/s. If we take 447 Hz as an example, there are 447 voltage sweeps in each second, which means that there would be 582 data points for each sweep. If we further assume that an amplitude of 5 V from the function generator was used, then we would have a resolution of $5/582 = 9\,\mu$V for this measurement. The resolution in terms of current can then be determined by simply dividing the voltage resolution with the standard resistor that we use.

B.3.2 Sampling time

Another parameter in the measurement is the sampling time, which is simply the time we spend on each data acquisition session. For instance, if a 1 Hz signal is supplied and the sampling time is 10 s, then we would expect to have collected 10 different measurements of the critical current. To get a better sense of the optimal number of repeats for each I_c measurement, about 15000 I_c points were collected. The average I_c and the most probable I_c were then computed for a subset of randomly chosen n measurements out of the total 15000 I_c collected, for n ranging from 1 to 15000 (Fig. B.6).

Fig. B.6a shows that for $n > 6000$, the average I_c already comes within a 15 nA window, about the minimum necessary for our experiment. To get a better statistical distribution of I_c, measurements would be repeated 10000 times or above. Another interesting observation is the dependence of the most probable I_c as a function of the number of repeated measurements (Fig. B.6b

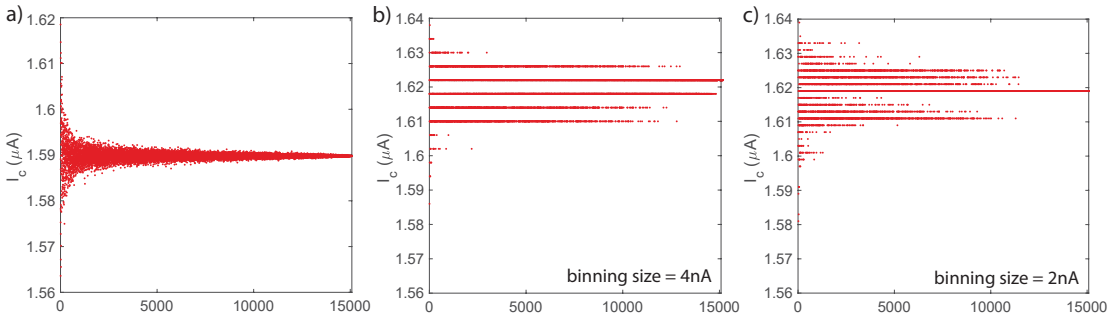

Figure B.6: Average and most probable critical current as a function of total number of measurements (x-axis), measured at a magnetic field of 6.92 T and a back gate of 0 V. **a**, Average critical current. **b**, Most probable critical current with a binning size of 4 nA. **c**, Most probably critical current with a binning size of 2 nA.

and Fig. B.6c). There is no strong convergence towards one fixed I_c value, confirming the intrinsic nature of the multiple switching currents present in these junctions. However, it is apparent that for larger n, I_c settles into fewer values.

In reality, we do not want to take too long to complete a single measurement sequence to get the best data possible, not only because the ^{3}He fridge has a finite condensation time, but also because the zero offset of the operational amplifier (op-amp) used to measure the voltage across the junction naturally drifts over time. Therefore, for a two-dimensional scan that involves varying the magnetic field and the back gate, a smaller n was used. Meanwhile, for linear scans (only varying back gate at a constant magnetic field, for instance), more time is dedicated to each I_c measurement.

B.3.3 Determining I_c and saving the data

At a sampling rate of 26000/s with two active channels, it would not be possible to save all of the voltage data onto the hard drive. Thus, a decision has to be made on what the I_c is, and only this I_c data would be saved.

Although it is possible to measure with a trigger with the DAQ (for example, to save a few data points before and after certain threshold is crossed), we opted to temporarily save the I-V data for

one measurement instance, identify the critical current in MATLAB, and continue with the next measurement instance, which overwrites the already saved I-V data. This "manual" identification of I_c gives us a better idea of the kind of noise present in the measurement and the reliability of the results.

One criterion that we can use to identify the I_c is to search for the largest jump in the measured voltage in a single sweep, because the most striking feature about a superconducting transition is that the voltage across the junction suddenly changes from zero to some finite value. Alternatively, we can also simply set a voltage threshold that indicates a superconductor-normal transition when crossed from below. Due to the signal fluctuations introduced by the noise, the threshold method was found to be be more consistent and was used instead.

In setting the voltage threshold, we would like to set it tight so that we are only sensitive to the first transition in the I-V scan, because there are always a multitude of transitions once the first critical current is exceeded (Fig. B.2). In addition, we have to allow some tolerance for noise as shown in Fig. B.4d and the drift of zero offset from the op-amp over the course of the experiment. A minimum of I_c is also hard-programmed to reject any I_c computed by the program that is too small. For example, if the I_c for a particular set of gate and magnetic field parameter space is generally above 5 μA, then a rejection threshold of 5 μA can be set so that anything less than that would not be saved as an I_c.

Despite this rejection threshold, electromagnetic noise from the electrical mains gives rise to unexpected "bumps" that cross the rejection voltage threshold and trigger the program to save false I_cs. While we are unable to correct this problem during the course of the measurement, we can nevertheless gain a sense of the reliability of the data collected by comparing the number of I_cs the program saves to the number of dc voltage sweeps actually performed. For instance, if there are 10 periods in a single measurement, then there should be 10 I_cs identified in the ideal case. However, with false I_cs, the saved data would have a larger number of I_cs saved than the number of cycles (periods)

of voltage sweeps. If the ratio of the number of saved I_cs to the number of voltage cycles is much larger than 1, then this indicates that some systematic problem is present in the measurement, either due to a sub-optimal selection of voltage threshold, amplitude of the voltage from the function generator, or amplitude of the the magnification of the op-amp. The data acquisition program saves a maximum of 1.6 to 1.8 times of the expected numbers of I_cs.

A single set of measurements running through a set of back gate and magnetic field usually takes somewhere between a few hours and up to 2-3 days. During data acquisition itself, a subset of the critical current is plotted to allow any abnormality to be quickly identified during the measurement (Fig. B.7). The top panel in Fig. B.7 monitors the two voltage input channels, and the bottom panel is the I_cs identified.

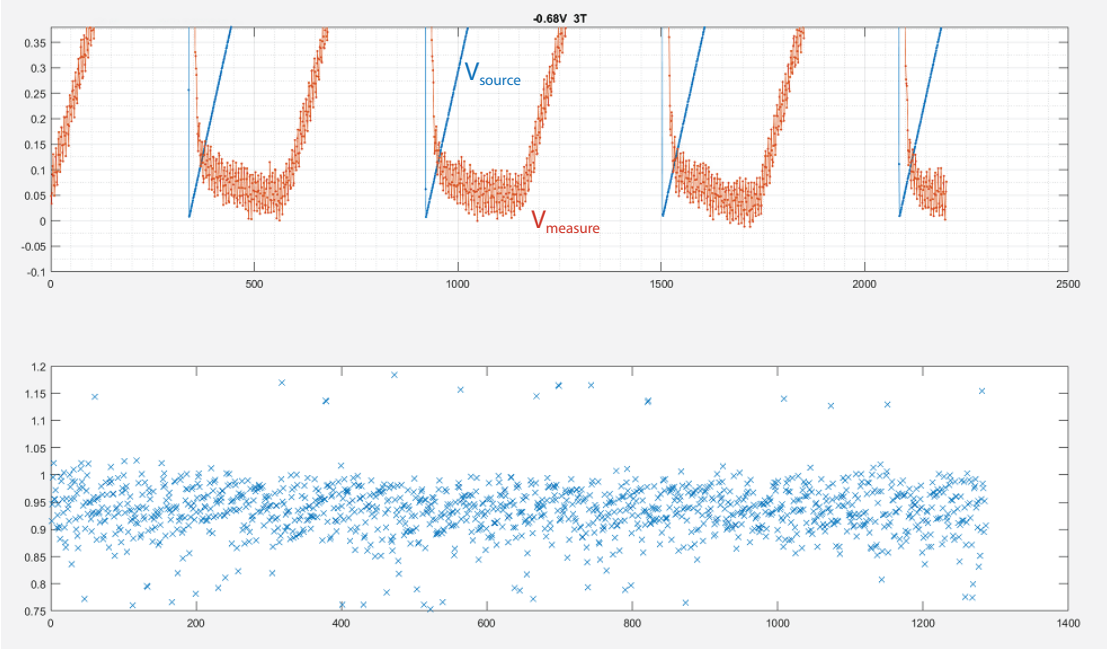

Figure B.7: A screenshot of data acquisition for a critical current measurement session. Upper panel: Sourced voltage V_{source} (blue) and voltage across the junction $V_{measure}$ (orange-red), both measured in volts. Lower panel: A subset of I_c identified during the same measurement session. Note that the actual measurement collects data points that are significantly more dense.

Given that the data were acquired at a rate around 270k/s, with thousands of I_c collected for one measurement, only the first few cycles of voltage acquired were plotted, and that only every 8th I_cs were plotted. This is sufficient for us to monitor the presence of noise, and the signal drift due to the op-amp to assess the overall effectiveness of the threshold voltage set at the beginning of a measurement (from the upper plot). Moreover, in the case of a larger-than-usual noise, the I_c in the bottom plot would display a periodic pattern, for which the measurement would be terminated prematurely and its parameters adjusted.

B.4 Post-acquisition analysis

As explained in the previous section, the I_c for each voltage sweep was identified and saved, including any possibly incorrect I_c values. Initially, we simply computed the average of I_c, after discarding I_c values from the top and bottom few percent, but we soon realized that there would be strange discontinuities in the results. An examination of the probability distribution of I_cs reveals that it is sometimes bimodal or even trimodal, with the I_c distribution centered around more than a single value. Finally, the I_c for a given magnetic field and back gate presented in this thesis was the "most probable" I_c, namely the I_c with the largest count number after binning the raw I_c data with a binning size of either 2 nA or 4 nA.

Although I_c determined this way could be jumping between different "branches" (from one mode to another) in its distribution, this method is more robust against false I_cs due to random noise, because they would have a low probability count and drop out naturally. In the probability distribution plots presented throughout this dissertation, the I_cs would be those on the red end of the spectrum of a blue-red color scale (i.e. the highest probability).

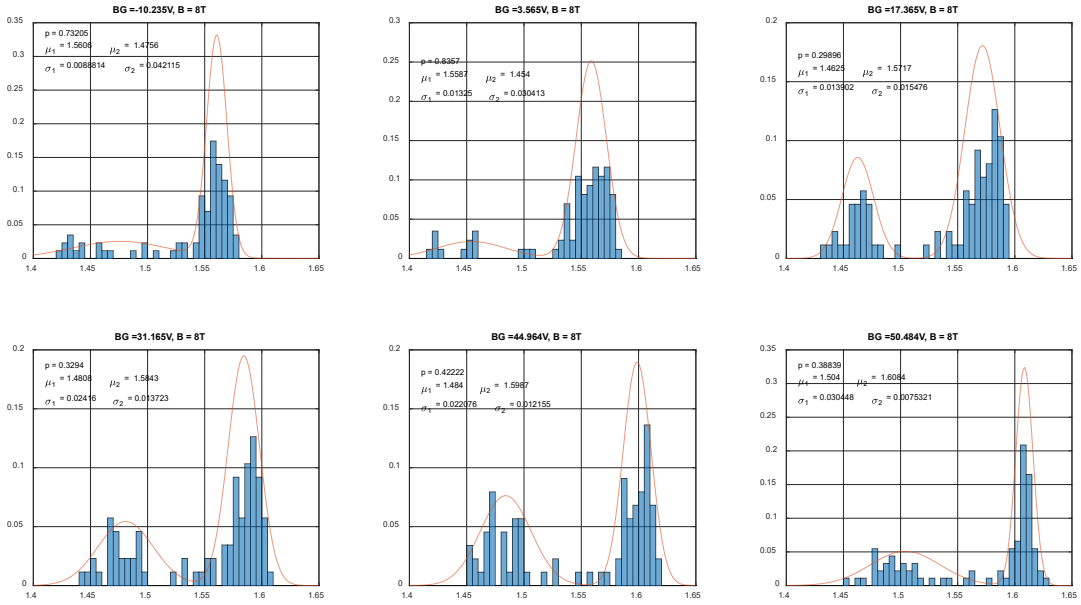

Figure B.8: Fitting I_c data to a weighted sum of two normal distributions at a magnetic field of 8 T for selected back gate values (y-axis: probability, x-axis: critical current I_c in μA). The blue bars are the histogram of the measured I_c while the red curve is the fitted distributions. Parameter p is the weight of the normal distribution with the higher mean. The data fit to a sum of weighted normal distributions reasonably well.

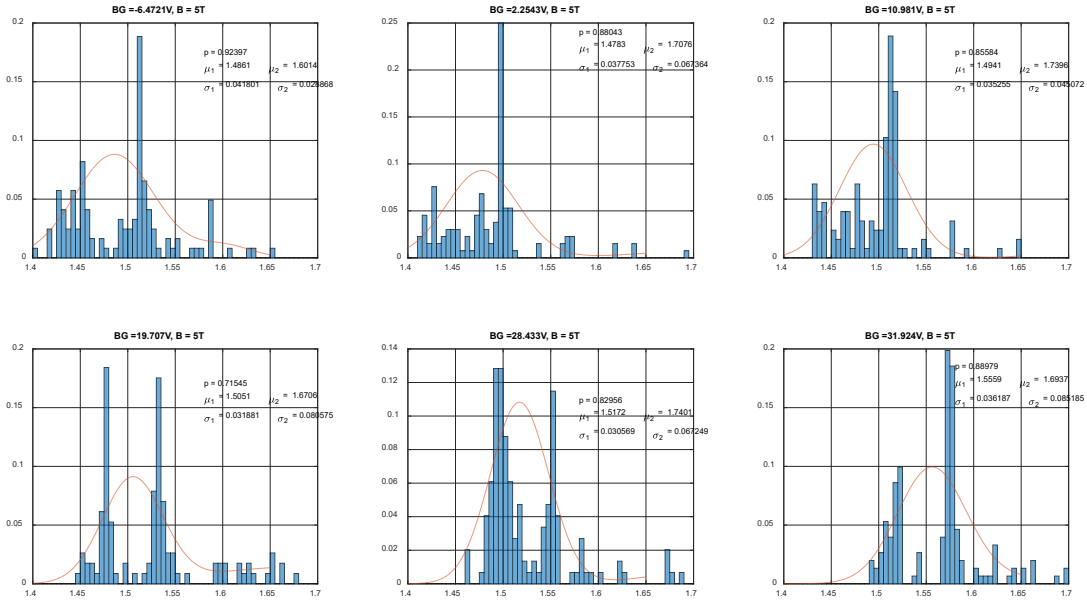

Figure B.9: Fitting I_c data to a weighted sum of two normal distributions at a magnetic field of 5 T for selected back gate values (y-axis: probability, x-axis: critical current I_c in μA). The data fit was poor.

B.5 Statistical distributions of I_c

Because the distribution of I_cs tends to have more than one most probable value, could it be a bi-modal normal distribution, with each mean I_c corresponding to a particular micro-structure in the physical Josephson junction? To answer this question, we attempted fitting the distribution to a sum of two weighted normal distributions. While the fitting was good in some cases (Fig. B.8), it failed to capture the features of the data in others (Fig. B.9). Thus, we conclude that the switching event is indeed stochastic, and the variance we observed in I_c measured under the same condition is not just due to uncertainties in the measurement, but is instead an intrinsic nature of the device itself.

B.6 Other considerations

B.6.1 Low-pass filters and the operational amplifier

As Josephson junctions are sensitive to high-frequency noises, a two-stage RC (low-pass) filter was used in all measurements (Fig. B.10). The sample holder was mounted onto the RC filter, which was subsequently loaded into either the ^{3}He fridge (300 mK) or a dilution fridge (about 50 mK). We used an RC filter with a frequency about 1 kHz in our experiments.

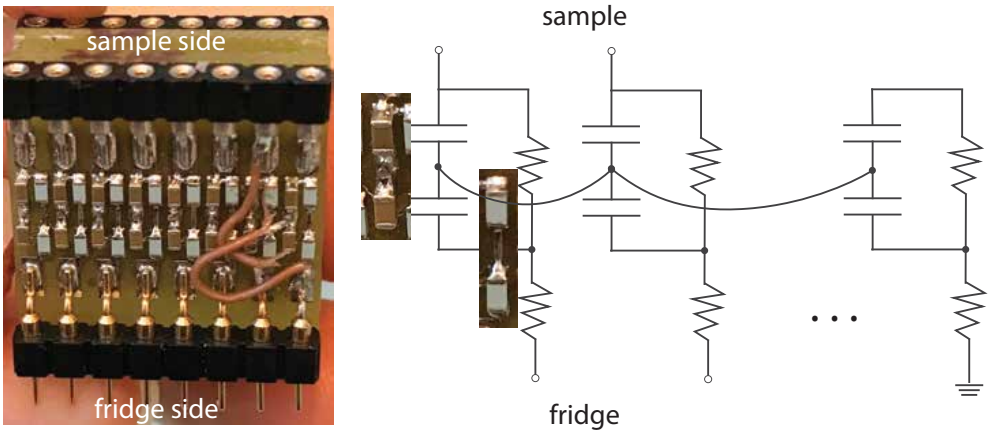

Figure B.10: The RC filter, a.k.a the low-pass filter used in the experiment. The sample is plugged into the RC filter from the top, which is mounted onto the fridge via the pins at the bottom. It is a two stage-filter with the wiring diagram on the right. Pin 16 (the right most pin in both the photo and the schematic) is the ground of the RC filter and not connected to the sample. Pin 15 is by-passed (i.e. connected to the ground directly without any resistor or capacitor components), and used as the connection for back gate. Because the capacitors have a finite breakdown voltage, by-passing the back gate allows us to apply a high gate voltage.

As shown in Fig. B.3, the sample is connected to a two-stage RC filter as shown in Fig. B.10, and to an op-amp, from which the voltage is measured with the DAQ. The low-pass filter on the op-amp was set to 1 kHz or lower and we find that the signal loss is not a significant problem for us with these settings.

The amplification on the op-amp was set to the maximal possible value to enhance the sensi-

tivity of our measurement. The maximal output possible for the op-amp is 10 V, but the normal resistance of the junctions varies significantly across different magnetic fields and back gate values. A good amplification would be one that is large enough to allow detection of the smallest normal resistance without overloading the op-amp and DAQ for a prolonged period of time, because the DAQ could be damaged with persistent overloading, especially in differential mode that we were using. Another consequence of persistent overloading is that it causes a larger drift in the zero offset of the op-amp in given time period, which drastically decreases the reliability of the measurement. In the worst case scenario, it can halt a measurement if the zero offset had drifted beyond the rejection threshold voltage.

Therefore, at the beginning of each measurement, a pre-scan is usually necessary to set an optimal threshold voltage and amplification of the op-amp, to make sure that the maximum and minimum I_c in the measurement can be measured correctly. At the same time, the amplitude of the voltage sourced from the function generator should also be optimized to allow the largest I_c in a measurement to be determined with maximum resolution possible.

B.6.2 Reproducibility of the critical current

The critical current is reproducible in the same thermal cycle. However, the switching current also depends on the speed at which the voltage is ramped. Because the junction always has a finite probability of switching even at a low temperature, the faster we ramp the voltage, the larger the critical current we would obtain. Therefore, if we want a consistent comparison of critical current measured across different magnetic fields and back gate values, then the frequency and amplitude set on the function generator, the amplification on the op-amp, as well as the threshold voltage in the data acquisition program should all be kept constant during a single measurement. For the same reason, if the critical current from different measurements were to compared, then they would not be exactly the same, even if they were measured under the same conditions.

B.6.3 Circumventing noise

With a dc measurement, we lose protection against noise from the conventional lock-in measurement. The most prominent noise source is the 60 Hz mains hum and its higher harmonics. Besides carefully checking and eliminating any ground loops in the measurement, the following steps also significantly decreased the noise in the measurement.

1. Twist pairs of BNC cables as tightly as possible. This is especially important in this measurement to choose BNC cable of the same length, and twist them to minimize the area of a wired loop as far as possible. Adjusting the orientation of the "loop" might also help.

2. Avoid stacking the DAQ directly on top of any lock-in amplifiers (or other measurement instrument), which was found to generate more noise in the measurement.

The 60 Hz noise would most likely still be present after removing other sources of noise that one could think of. Depending on the signal, one common practice is to Fourier transform the measured signal and manually delete the components due to 60 Hz and its higher fundamentals. However, the actual signal necessary for determining I_c convolutes strongly with the 60 Hz noise such that removing the 60 Hz noise irreparably distorts the signal. Therefore, we tune the frequency of the bias voltage used for the measurement to minimize the effect of the 60 Hz noise.

Similar to a lock-in measurement, the frequency of the dc voltage should be away from harmonics of 60 Hz. In earlier measurements where the cutoff frequency of the RC filter was only 100 Hz, 1 Hz was used for measurement to mitigate noise. However, with a cutoff frequency at about 1 kHz, a measurement frequency of around 200 Hz to 450 Hz yielded reasonably good results.

B.7 Code sample: DAQ data acquisition

The data acquisition program used to measure I_c in Fig. 3.13 follows.

1. Establishing connection between DAQ and MATLAB and configure the input channels:

```
s = daq.createSession('ni');
ai2 = addAnalogInputChannel(s,'Dev1',2,'Voltage');
ai3 = addAnalogInputChannel(s,'Dev1',3,'Voltage');
ai2.TerminalConfig = 'Differential';
ai3.TerminalConfig = 'Differential';
ai2.Range = [-10 10];
ai3.Range = [-10 10];
```

2. Setting up the scanning parameters:

```
freq = 277.777777;
samplingrate = 260000;
samplingtime = 12;

ncycle = floor(freq*samplingtime);
% ncycle is the number of voltage sweeps, i.e. number of true Ics
n = samplingrate*samplingtime;
% n is the total number of data points for one measurement instance
s.DurationInSeconds = samplingtime;
s.Rate = samplingrate;
nn = 1200;    % used for real-time plotting

backgate = -5:0.3:45;
backgate = [backgate 45];  % the back gate values to be scanned, 168 points
```

```
bfield = 8:-0.075:5;  % the magnetic field values to be scanned, 41 points

Vth = 0.015;  % thrshold voltage to trigger an Ic idenfitication
Icmin = 5;  % Ic rejection threshold; Ic discarded if it is smaller than Icmin
nIcsave = floor(ncycle*1.8);
% 1.8 times the actual number of Ic are saved to allow space for false Ics
folder = 'Ic1105_2D\';
```

3. Data acquisition:

```
for fieldindex = 1:length(bfield);
    % ramp the magnetic field with special measure
    fieldset = bfield(fieldindex);
    smset('Field',fieldset);

    % initialize a data matrix for Ic measured at all gate values
    % for one magnetic field
    Icmat_unsorted = zeros(length(backgate), nIcsave);

    for gateindex = 1:length(backgate)
        % ramp the back gate to the target value
        gate = backgate(gateindex);
        smset('BG',gate);

        % start data acquisition with DAQ
        data = s.startForeground();
```

```
Vstemp = data(:,1);   % voltage sourced from the function generator
Vmtemp = data(:,2);   % voltage measured across the Josephson junction

% Critical current at the current back gate and magnetic field
Ic = zeros(nIcsave,1);

k = 1;   % counts the number of critical current being saved (kth Ic)
% j scans through all data points collected during sampling time
% Ic is idenftied if the measured voltage Vm crosses the Vth
% from below, and if the voltage is larger than the rejection voltage
% value set. Only voltage value is saved and the conversion to current
% is done during data analysis
for j = 1:n-1
    if (Vmtemp(j+1) > Vth)&& Vstemp(j)> Icmin && (Vmtemp(j) < Vth)
        Ic(k) = (Vstemp(j)+ Vstemp(j+1))/2;
        k = k+1;
    end
    if k > nIcsave
    break
    % if for some reason the program identifies many false Ics and
    % exceeds the maximum number % we want to save (nIcsave), Ic
    % search stops with the rest of the voltage data points unscanned
    end
end
```

```
        % Ic for a partiular gate and magnetic field is saved into the larger
        % Ic data matrix
        Icmat_unsorted(gateindex,:) = Ic;

        % real time plotting to show both voltage measured and Ic identified
        subplot(2,1,1)
        plot(data(6*(1:nn),:),'.-'); grid on
        ylim([-0.1 0.1])
        title([num2str(gate) 'V  ' num2str(fieldset) 'T'])
        subplot(2,1,2)
        plot(Ic(8*(1:floor((ncycle-10)/8))),'x')
    end
        % after the measurement is done for a particular magnetic field, it is
        % saved to a file, so Ic measured at any magnetic field would have a single
        % file, containing all Ic meausred  at all back gate values
        dlmwrite([folder 'Icmat' num2str(fieldset) 'T_277Hz'],...
            Icmat_unsorted);
end
```

4. Saving back gate and magnetic field information:

```
dlmwrite([folder 'backgate_1105_277Hz'], backgate);
dlmwrite([folder 'bfield_1105_277Hz'], field);
```

C

Supplementary data on narrow Josephson junctions

C.1 Temperature dependence of I_c

The temperature dependence of the resistance measured across the junction shows two transitions (Fig. C.1), corresponding to the superconductor-normal transition of the Josephson junction (~ 9

K) and that of the NbN contacts ($\sim$ 12 K). The critical current of this junction is larger than 10 μA at low temperatures. Throughout the measurement, the graphene was gated at 40 V away from the Dirac point.

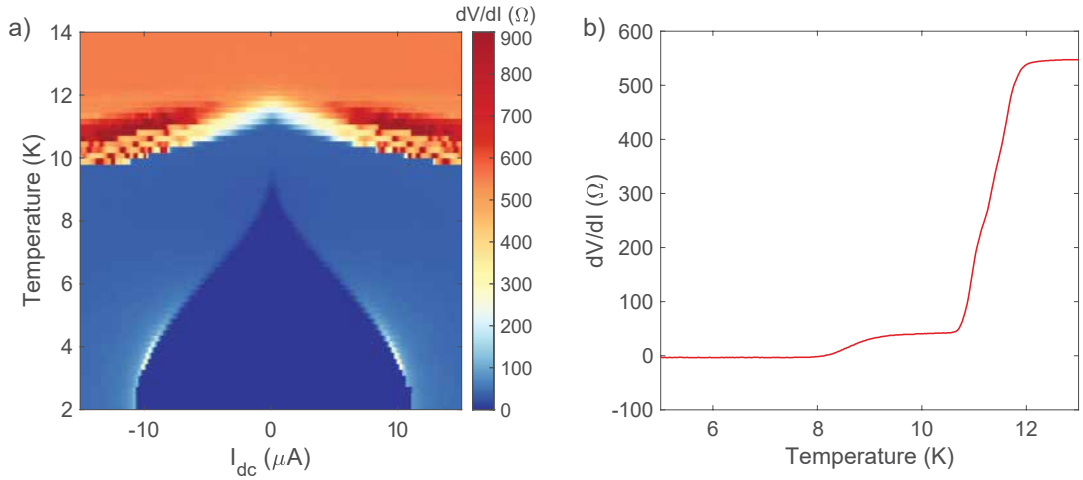

Figure C.1: Temperature dependence measured across narrow junction 2. **a**, Junction resistance measured as a function of dc current and temperature. **b**, Temperature dependence of the junction resistance with zero dc bias current.

C.2 I_c AND R_n AT ZERO MAGNETIC FIELD

We take a closer look at Fig. 3.3 presented in Chapter 3 by plotting the differential conductance versus the voltage developed across the junction measured with a digital multimeter, as a function of back gate (Fig. C.2a). In this measurement, the junction was never biased above the NbN superconducting gap ($\sim$ 2 meV), which confirmed that the superconducting-resistive state transition observed in Fig. C.2b was due to the critical current of the junction being exceeded.

Furthermore, Andreev processes are present when the energy of the incoming electrons is below the superconducting gap. Therefore, the normal resistance R_n of the junction cannot be determined from this particular measurement and we only provided an estimate in Chapter 3. In fact, a better estimate for R_n could be extracted from a temperature dependent measurement, such as that in

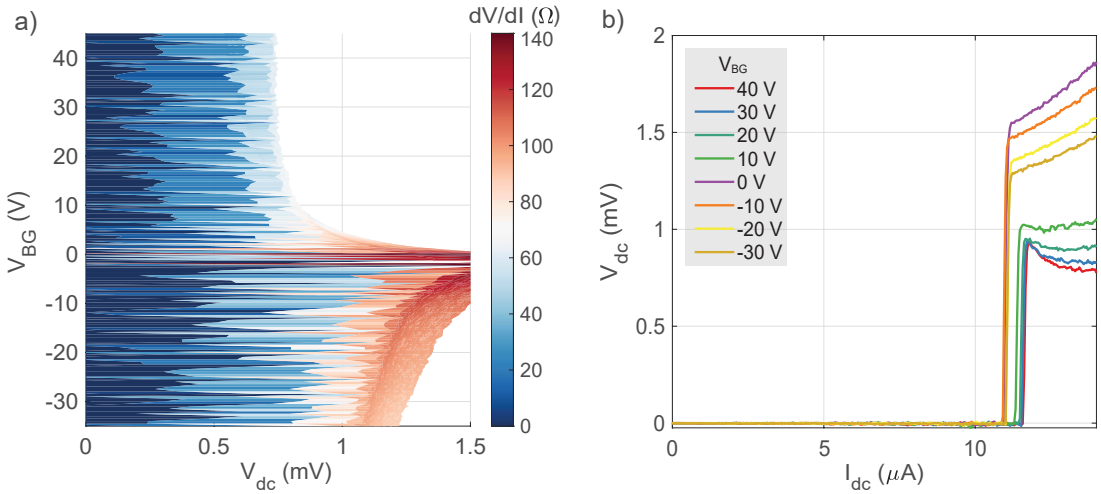

Figure C.2: **a**, Differential resistance versus measured voltage across the junction (V_{dc}), at different back gate voltages (V_{BG}). **b**, Measured voltage across the junction (V_{dc}) as a function of dc current (I_{dc}), at selected back gate values.

Fig. C.1b. A detailed discussion of the determination of R_n in narrow junction devices and related measurements can be found in Appendix D.

C.3 I_c IN THE HOLE-DOPED REGIME AT FINITE MAGNETIC FIELDS

In Chapter 3, we presented I_c measured in electron-doped regimes at finite magnetic fields. In fact, as the quality of NbN-graphene contact tends to be better on the electron-doped side, most of the measurements were performed when the sample was positively gated. For completeness, Fig. C.3 shows the critical current of the narrow Josephson junction when the sample was hole-doped. The most prominent feature is the plateau between -20 V and -10 V, which corresponds to a filling factor of $\nu = -6$. There is also a small plateau on the rightmost side of all of the plots, which corresponds to a filling factor of $\nu = -2$. This is cut off in this series of measurements because the back gate was only scanned until -5 V, while the Dirac point was around 0 V. However, part of the $\nu = -2$ critical current plateau can be seen in Fig. 3.11 and other plots in Chapter 3, where the back gate was varied between -5 V and 45 V.

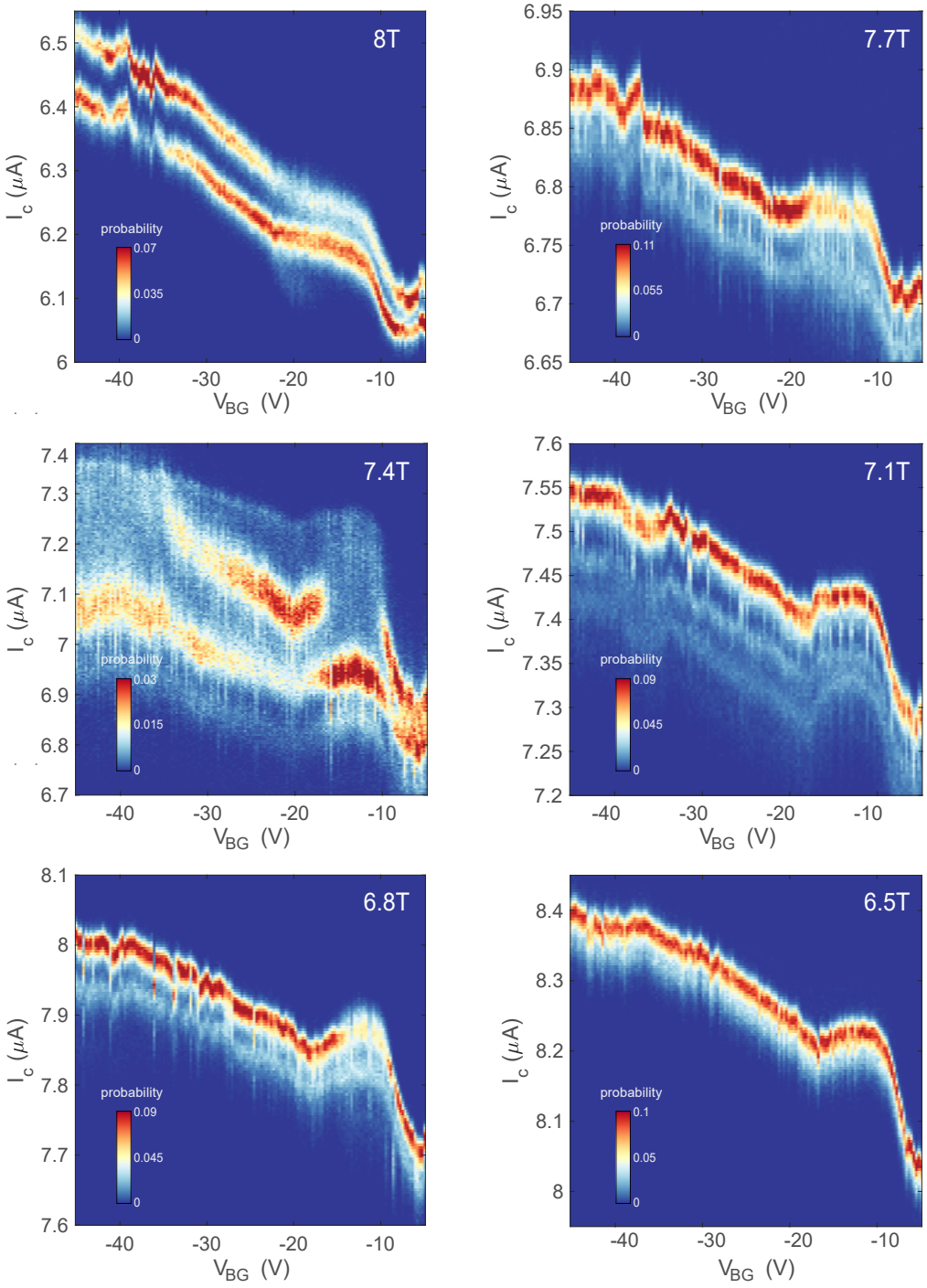

Figure C.3: Critical current I_c when the graphene is hole-doped (negatively gated). All I_c steps are lost except for $\nu = 2$ (the rightmost step), and $\nu = 6$ (the most prominent plateau-like feature in these measurement).

C.3.1 I_c AS A FUNCTION OF MAGNETIC FIELD AT A CONSTANT BACK GATE

In Fig. 3.6b in Chapter 3, we presented the critical current I_c as a function of magnetic field at a few selected back gate values and noted that the magnitude of I_c is similar across different gates. If we decompose the Josephson junction into two Josephson junction $\mathrm{JJ}_{\mathrm{direct}}$ and JJ_{qH} connected in parallel as outlined in Section 5.1 of Chapter 5, then it would be meaningful to examine the evolution of $I_{c,qH}$ with the magnetic field while keeping the back gate constant. This analysis is equivalent to taking vertical line cuts from Fig. 3.13c, and we expect to see steps similar to those in Fig. 3.13d.

However, given a lack of I_c data measured at the Dirac point, we attempted to subtract I_c at a back gate of 2 V from that measured at 40 V and 2 V respectively (Fig. C.4). We note that well-defined $\nu = 1$ quantum Hall plateau only starts to develop at high magnetic fields.

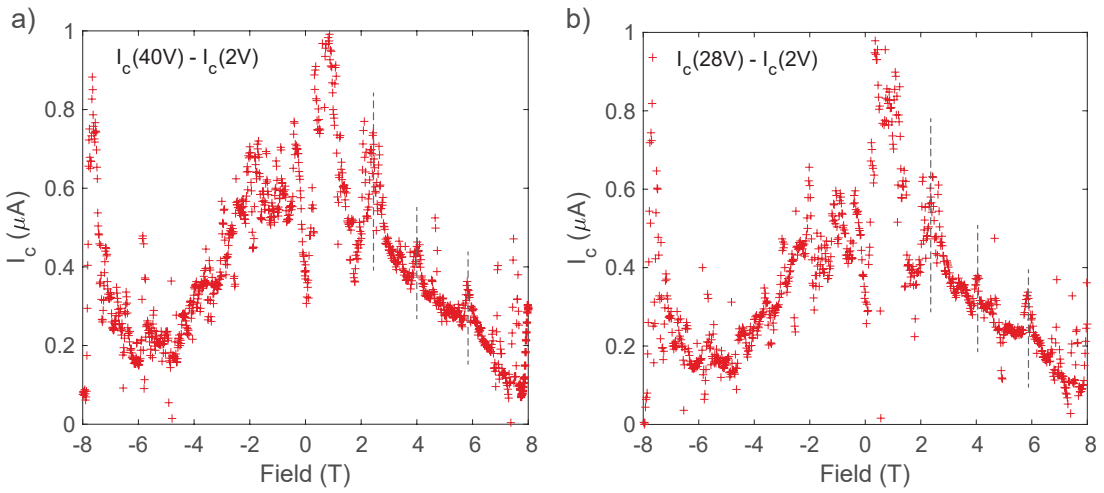

Figure C.4: **a** I_c measured at a back gate of 40 V with I_c measured at 2 V subtracted. **b** I_c measured at a back gate of 28 V with I_c measured at 2 V subtracted.

While the 28 V data (Fig. C.4b) provide some evidence for the formation of steps in positive magnetic fields, the majority of the data for both 40 V and 28 V did not exhibit clear step-like features. As we can already tell from Fig. 3.13c, the sample does not go through many quantum Hall

transitions at either of the back gate values. Moreover, changing the magnetic field moves the vortices around in these 80 nm wide type-II superconducting fingers, making the observation of the step-like modulation presented in Chapter 3 more difficult.

C.3.2 More on crossed Andreev reflection measurement

In Section 3.4.4 of Chapter 3, the efficiency of the crossed Andreev reflection at a magnetic field of -8 T was found to be about 1% (Fig. 3.19). However, when we measured at the opposite magnetic field of 8 T, the crossed Andreev reflection was negligibly small, as shown in Fig. C.5.

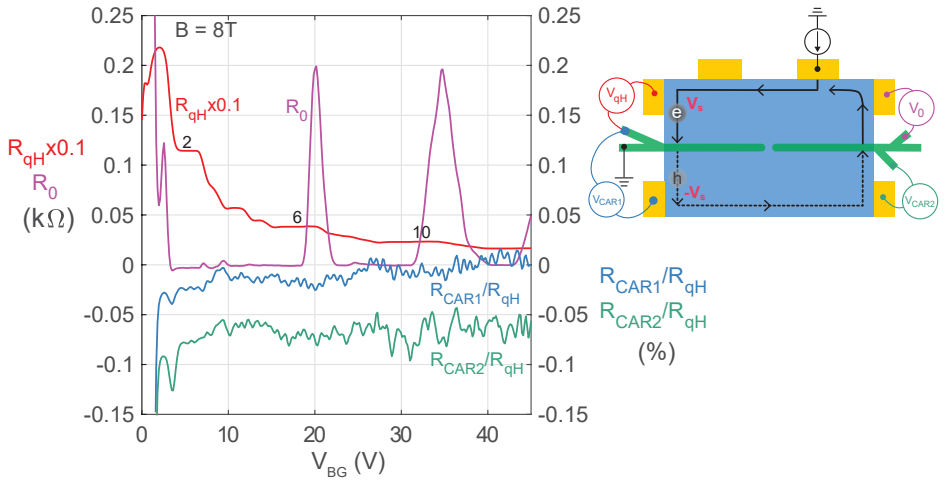

Figure C.5: Crossed Andreev reflection of the narrow junction 2 at 8 T and 300 mK. Left: 3-terminal R_{qH} (red) and R_0 (purple) (refer to the measurement schematic). Right: normalized crossed Andreev voltage measured closer to the first graphene-NbN interface, R_{CAR1} (blue), and further away from the first graphene-NbN interface, R_{CAR2} (green).

We also note that the voltage further downstream (V_{CAR2}, green curve in Fig. C.5) is slightly more negative then the voltage closer to the superconductor-normal interface where crossed Andreev reflection happens (V_{CAR2}, blue curve in Fig. C.5), at both 8 T and -8 T. This indicates that processes other than crossed Andreev reflection of either the quantum Hall edges states or the bulk are happening in this device.

In fact, the temperature dependent measurement of the crossed Andreev reflection also reveals some spurious effects. In Fig. C.6, the resistance curves measured at different temperatures clearly separate into two bundles at the NbN transition temperature of about 11 K (Fig. C.1). However, for filling factors $\nu \leqslant 2$, more negative R_{CAR} signals were measured, even as the temperature increased above the T_c of NbN (Fig. C.6, lower panel), indicating the presence of additional processes unrelated to superconductivity.

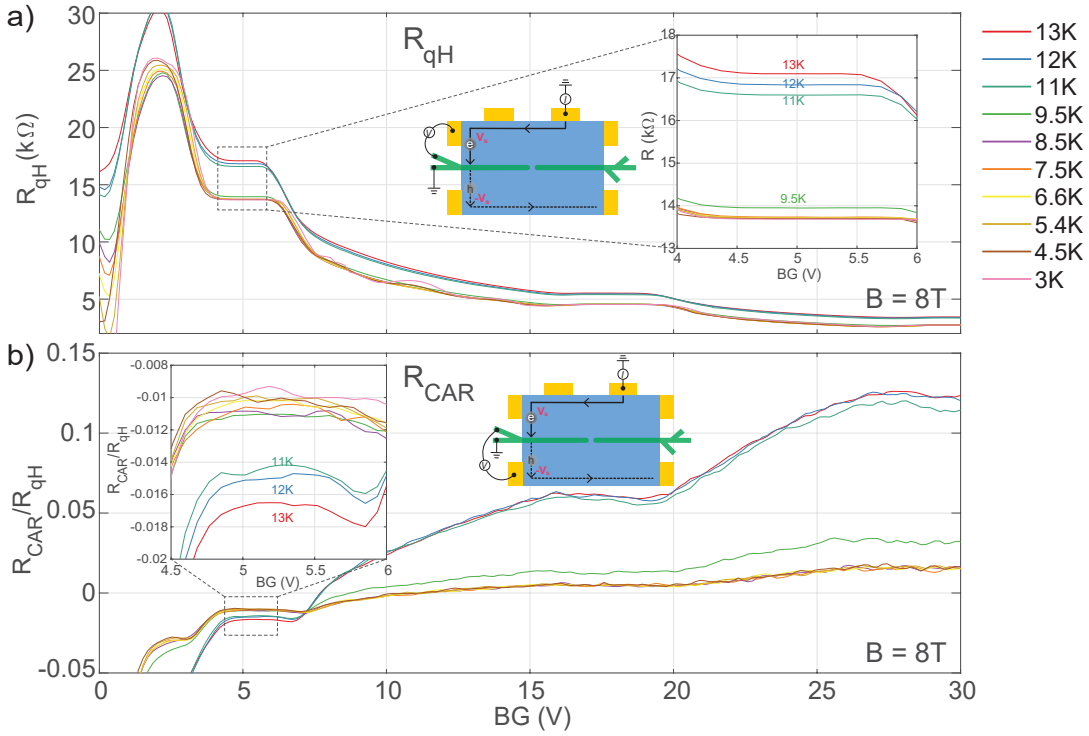

Figure C.6: Temperature dependence of the crossed Andreev reflection. **a**, Temperature evolution of 3-terminal R_{qH}. The jump in resistance between 9.5 K and 11 K is due to the NbN resistance as it turns normal above T_c. **b**, Temperature evolution of the normalized crossed Andreev voltage. The measured voltage became negative as temperature was raised.

C.3.3 Additional data of Shapiro step measurement

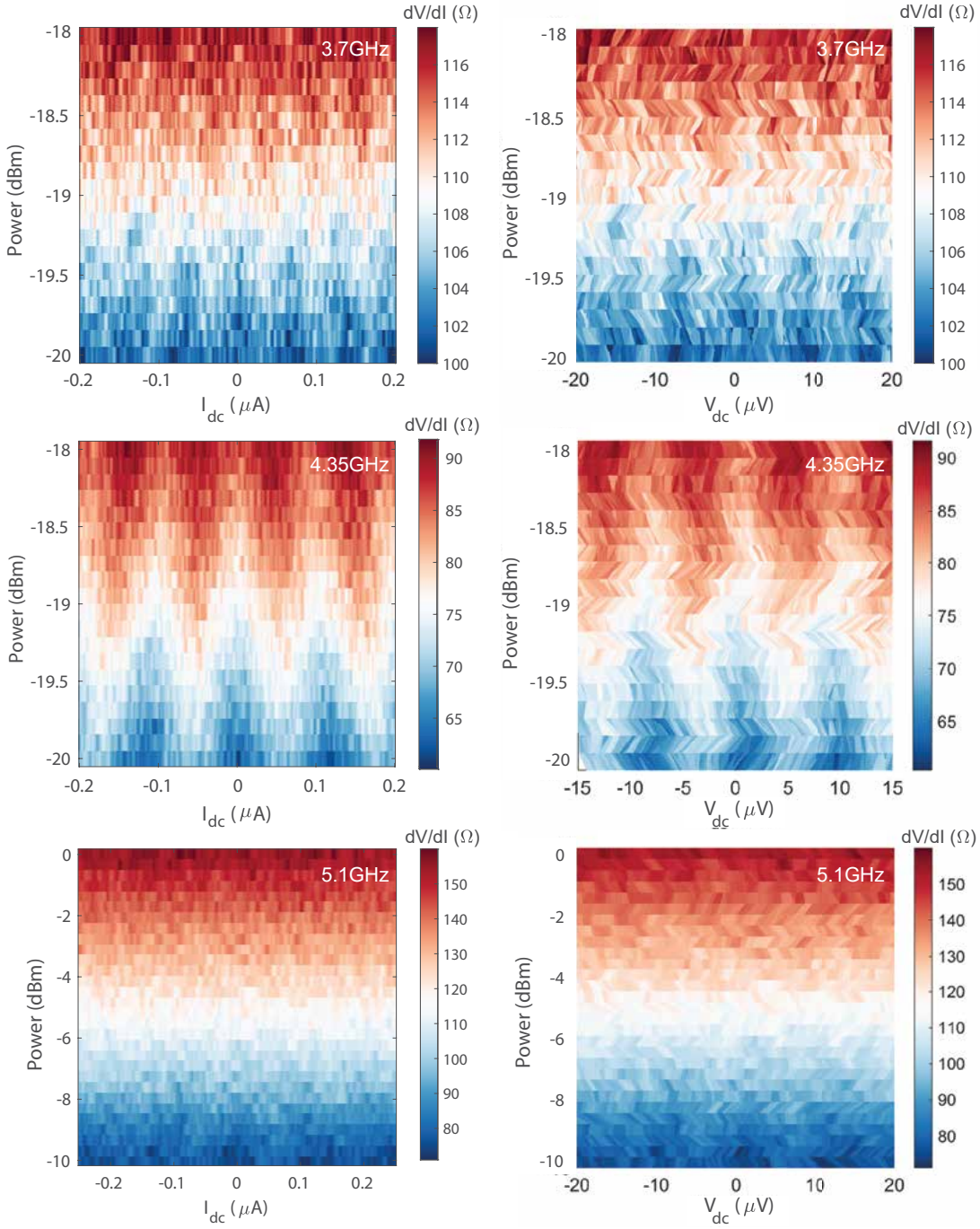

Figure C.7: Additional Shapiro steps measurement on narrow junction 2, at microwave powers of 3.7 GHz, 4.35 GHz and 5.1 GHz. The differential resistance is plotted as a function the dc current and voltage across the junction.

D

Determining the normal resistance R_n

In this chapter, we discuss the determination of the normal resistance R_{n} with two different approaches, namely the finite bias method and the finite temperature method, with data from narrow Josephson junction 1.

The product of the critical current I_{c} and the normal resistance R_{n} gives an estimate of the size of the induced gap of the Josephson junction, which in turn tells us on how well the normal region in an S-N-S junction is proximitized. However, caution has to be exercised in the measurement and

interpretation of R_n for narrow Josephson junction devices.

The finite bias method of measuring R_n is to bias the junction well above $2\Delta_{junction}$ (the gap of the Josephson junction), while maintaining the superconductivity of the superconductor, so as to measure only the normal state resistance of the junction. Meanwhile, the finite temperature method achieves the same measurement by bringing the Josephson junction to its normal state with an elevated temperature. In an ideal Josephson junction, these two schemes would be equivalent. However, there are three complications in our Josephson junctions:

1. While the supercurrent only passes through graphene in the immediate vicinity of NbN below the transition temperature of the Josephson junction, this part of graphene cannot be measured independently above the transition temperature. A two terminal measurement always measures both the R_n due to this small part of graphene, and other parts of the graphene connecting NbN contacts.

2. In the finite dc bias measurement scheme, additional transitions usually occur after Josephson junction first turns normal. Because we do not fully understand these transitions, they are difficult to keep track of, especially under a finite magnetic field and in the presence of quantum Hall states.

3. In the finite temperature measurement scheme, the non-sharpness of the transition temperature T_c of the Josephson junction also introduces some uncertainty.

Due to these reasons, it is challenging to pin down an R_n from these devices that is equivalent to that of a Josephson junction with a more straightforward two-terminal geometry. Nevertheless, we present and discuss R_n obtained using these methods.

We note that the finite temperature R_n is always used in other parts of this dissertation, unless otherwise stated.

D.1 Finite bias measurement of R_N at zero magnetic field

At zero magnetic field, the narrow Josephson junction undergoes two major transitions as the applied dc current through the junction increases (Fig. D.1), which indicates how the Josephson junction and the two NbN fingers subsequently turn normal. The voltage drop across the junction is also monitored, as shown in Fig. D.1b, to compare the energy of the incident electrons with that of the gap of NbN ($\sim$ 2 meV).

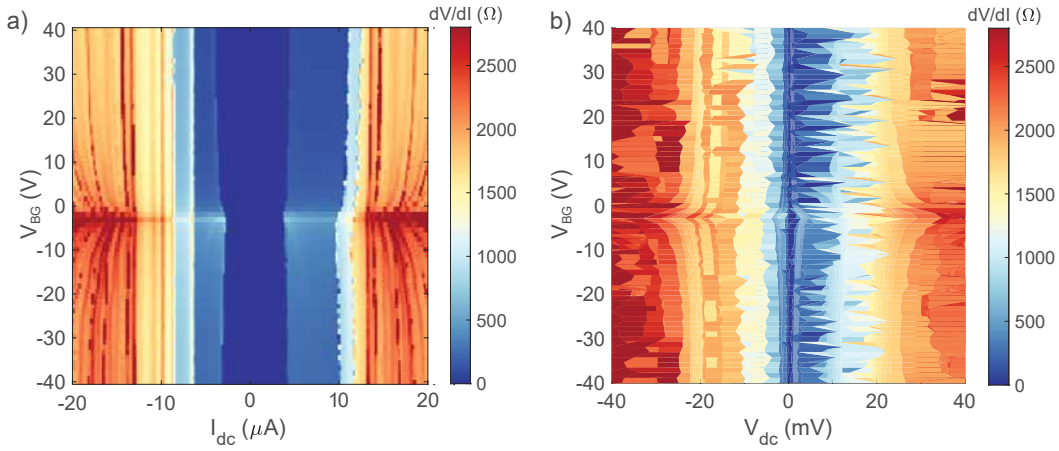

Figure D.1: Differential resistance of the junction at zero magnetic field and 300 mK. A dc current was ramped from -20 μA to 20 μA. **a**, The junction goes through three transitions, likely to correspond to the superconductor-normal transitions of 1. the Josephson junction; 2. one of the NbN finger; 3. the other NbN finger. **b**, Differential resistance dV/dI of the junction as a function of measured voltage drop across the junction.

The normal resistance R_n would be the R of the junction with the incident electron energy well above the gap of the superconducting electrodes (usually $> 2\Delta$), while the superconducting electrodes are still superconducting. Unfortunately, this regime does not exist in our devices: before a voltage drop larger than the gap could be developed across the junction, the critical current of the junction would be exceeded and the junction turns normal.

Nevertheless, we can estimate the normal resistance R_n of the junction at zero magnetic field in the following manner:

1. Read off the R for one of the fingers from the dV/dI measured after the first transition: $\sim 700\ \Omega$.

2. Assuming that two fingers have comparable resistance, the combined resistance of the two fingers would be $\sim 1400\ \Omega$.

3. The dV/dI measured at a high dc current/bias ($\sim 2200\ \Omega$) would contain R_{n} of the junction, as well as the resistance of the two NbN fingers combined. We then estimate R_{n} by subtracting the finger resistance from the total resistance:

   $R_{\mathrm{n}} \simeq 2200\ \Omega - 1400\ \Omega = 800\ \Omega$.

Because the critical current I_{c} of the junction is about 4 μA at a temperature of 300 mK, $I_{\mathrm{c}}R_{\mathrm{n}}$ product is about 3 meV, which is comparable to the gap of the NbN.

D.2 Finite temperature measurement of R_n at zero magnetic field

Fig. D.2 shows the temperature dependence of the junction. The R_{n} of the junction can be estimated by reading off the resistance around the point of inflection in the temperature sweep, which is about 750 Ω, quite close to that obtained with the finite bias method.

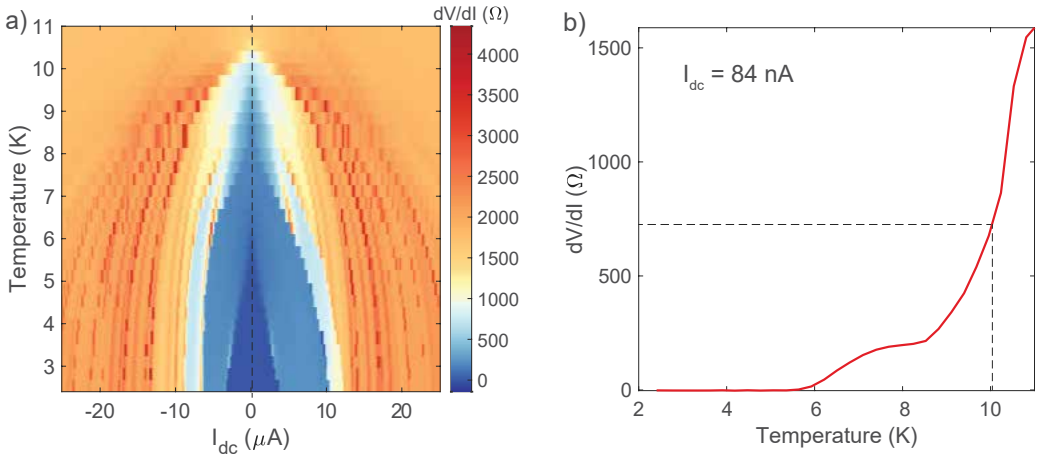

Figure D.2: **a**, Temperature and finite bias dependence of dV/dI across the narrow Josephson junction at a back gate of 40 V. **b**, A vertical slice from **a** at I_{dc} = 84 nm, showing the temperature dependence of dV/dI with a close to zero dc current.

D.3 Finite bias measurement of R_N in quantum Hall regime

The finite bias measurement gets more complicated in a finite field. On the one hand, we would like to pick a bias voltage as large as possible while NbN remains superconducting; while on the other hand, because I_c of NbN and contact resistance between NbN and graphene also change with magnetic field, it is hard to optimize the best bias voltage at which the measured resistance should be called R_n. Moreover, as a finite bias is applied, the energized electrons are likely to access higher quantum Hall states, which reduces the resistance and complicates the measured R_n.

We do not yet know how the resistance evolves with an applied dc voltage *a priori*, therefore we performed a three-dimensional measurement of the differential resistance as a function of applied dc current (voltage), back gate value, and magnetic field. In Fig. D.3 and Fig. D.4, we present the differential resistance across the Josephson junction in a few magnetic fields.

Similar to the zero magnetic field measurement in Fig. D.1a, we could identify two to three major transitions as more current is passed through the junction. Curiously enough, as the dc current

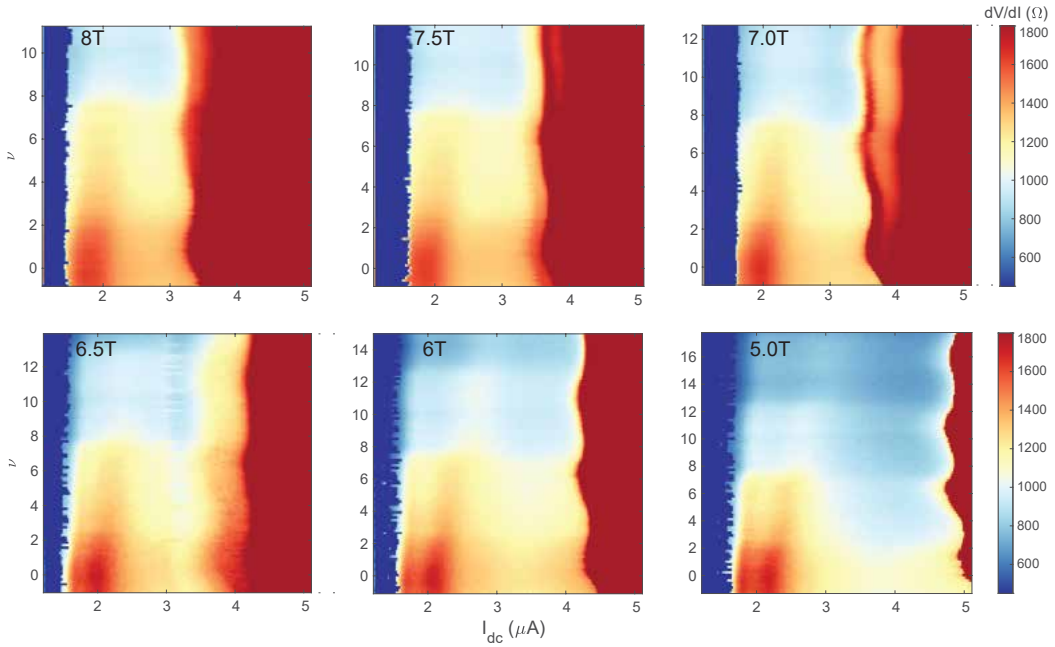

Figure D.3: Differential resistance dV/dI as a function of filling factor ν and dc current I_{dc} across the narrow junction for selected magnetic fields.

increases, the differential resistance first increases, and then decreases, before it goes through another transition where it increases again. We speculate that the decrease in resistance is a result of the increased availability of more conducting channels made possible by accessing higher quantum Hall states at an increased dc bias.

In identifying R_{n}, we want to avoid the far right of the spectra, where the resistance likely includes both the excited quantum Hall transport and NbN electrode. Consequently, we are constrained in our choice for V_{dc}, as seen from Fig. D.4. To avoid having to choose a different V_{dc} for each filling factor and magnetic field, a V_{dc} of 1.3 mV was chosen, at which resistance values are extracted (Fig. D.5). At a bias voltage of about 1.3 mV, the junction is at its a local resistance peak for a range of filling factors in different magnetic fields.

Unsurprisingly, the estimated normal resistance R_{n} exhibit steps that coincide with the quantum

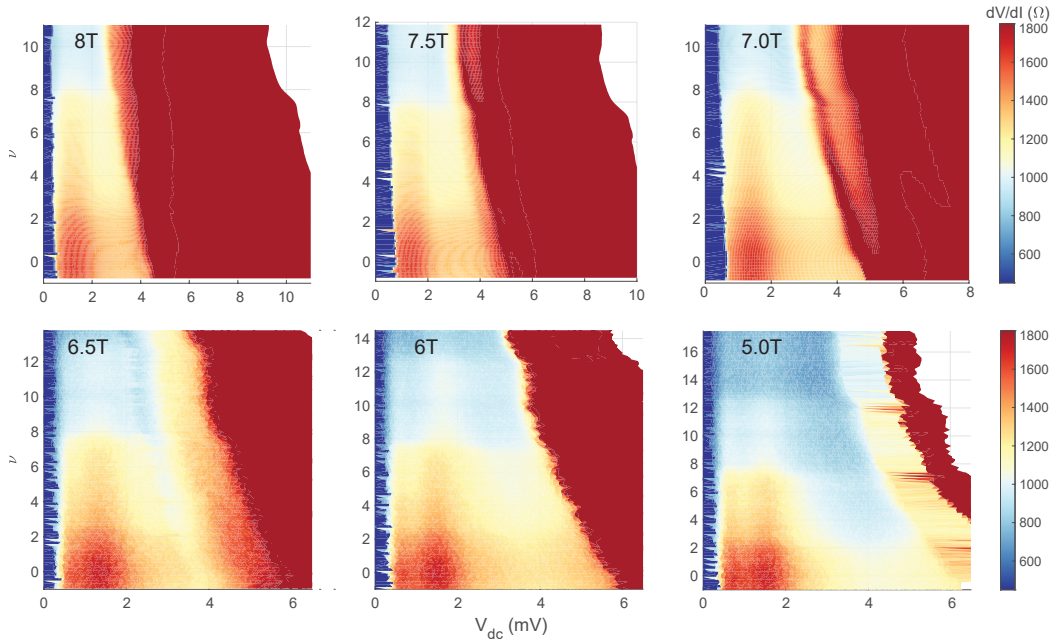

Figure D.4: Differential resistance dV/dI as a function of filling factor ν and dc voltage across the Josephson junction as measured by a digital multimeter, for selected magnetic fields.

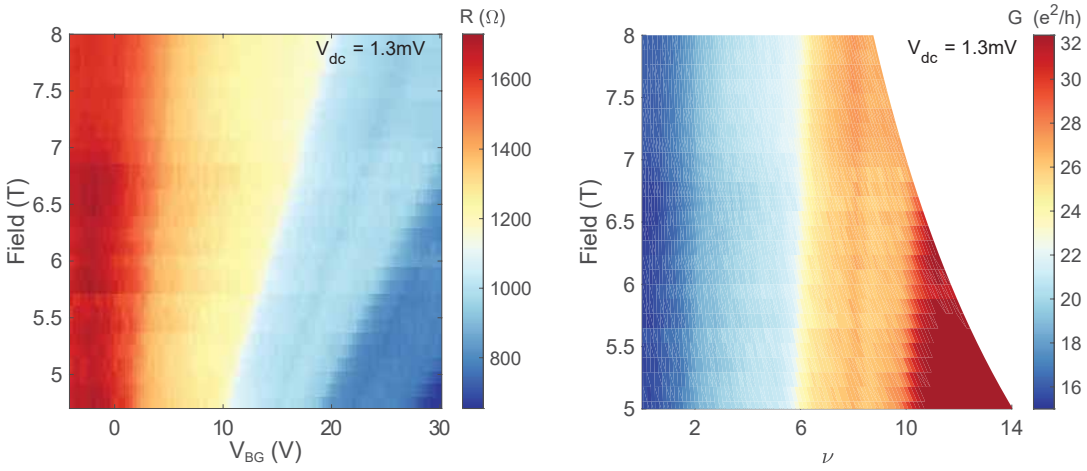

Figure D.5: Resistance across the narrow Josephson junction measured with dc bias voltage of 1.3 mV applied, at various doping and different magnetic fields. Left, as a function of back gate values (V_{BG}). Right, as a function of graphene filling factor ν.

Hall resistance steps.

In conclusion, the bias voltage measurement outlined in this section is rather labor-intensive, because it requires a preliminary three-dimensional scan over the phase space of dc current or voltage, back gate value, and the magnetic field. Despite the intensive effort, the R_n we obtain would still merely be an estimate of the "true" R_n in our junctions. Consequently, a finite temperature measurement of R_n is preferred in this dissertation.

D.4 Finite temperature measurement of R_N in quantum Hall regime

As the transition temperature of the Josephson junction decreases with an increasing magnetic field, we first identify the temperatures at which we would take our measurement. This is done by first fixing the magnetic field and measuring resistance as a function of temperature (Fig. D.6).

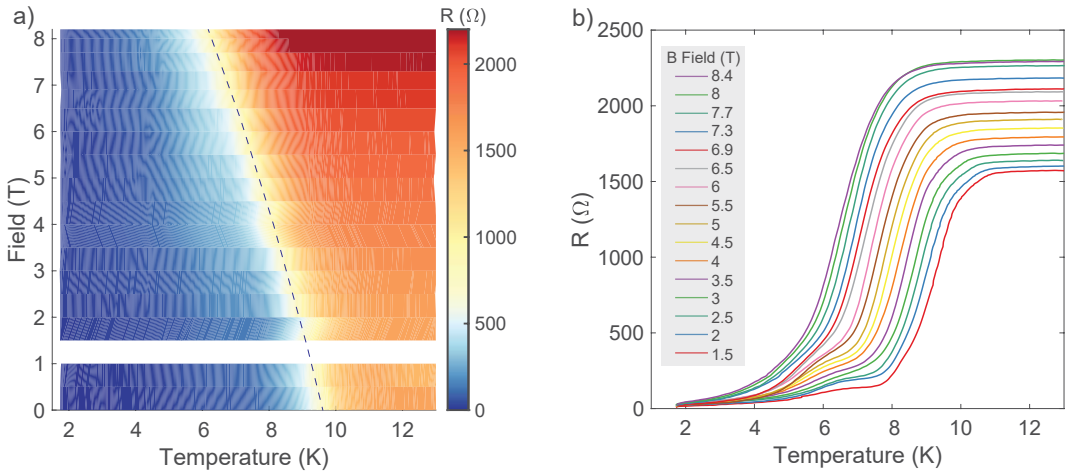

Figure D.6: Resistance across the narrow junction as a function of magnetic field and temperature. **a**, A 2D plot showing the field-temperature curve useful in subsequent R_n measurement. **b**, Line plots of resistance versus temperature at different magnetic fields, from which the transition temperature for each magnetic field was extracted to obtain the field-temperature curve in **a**.

For measurements at lower magnetic fields in Fig. D.6b, we observe the familiar double transition, similar to other low field measurements. For each magnetic field, we pick a temperature above

the first inflection, but just before the resistance curve starts to rise to make sure that the junction is normal but the NbN electrodes are not yet resistive.

Once the transition temperature T is identified for each magnetic field $B(T)$ in Fig. D.6b, they are fitted to the equation

$$B_c(T) = B_c(0)\left[1 - \frac{T}{T_c}\right].$$

Although this equation is only valid for type I superconductors, it is still a very useful approximation for us to determine a temperature for R_n measurement at any given magnetic field. The fitted curve obtained with this equation is overlaid with the 2D data plot in Fig. D.6a.

With the temperature information, we then measure the resistance across the junction for each magnetic field at its corresponding temperature. Caution was taken to ensure that: 1. enough time was given for the fridge to reach thermal equilibrium before measuring; and 2. when the sample was moved to a different fridge, the temperature reading of the new fridge is calibrated against the old one by doing a few temperature-magnetic field line sweeps as in Fig. D.6, and assuming the discrepancy of the temperature readings between different fridges is a linear offset due to the placement of the thermal sensor relative to the sample.

R_n measured with this approach is presented in Fig. D.7. Quantum Hall-like steps, similar to those in the finite voltage measurement Fig. D.5, were observed. Moreover, the variation of resistance is less smooth in the magnetic field direction, as shown by the horizontal lines in Fig. D.7a. This could be due to processes such as vortex pinning in NbN, because both magnetic field and temperature are being varied in this measurement.

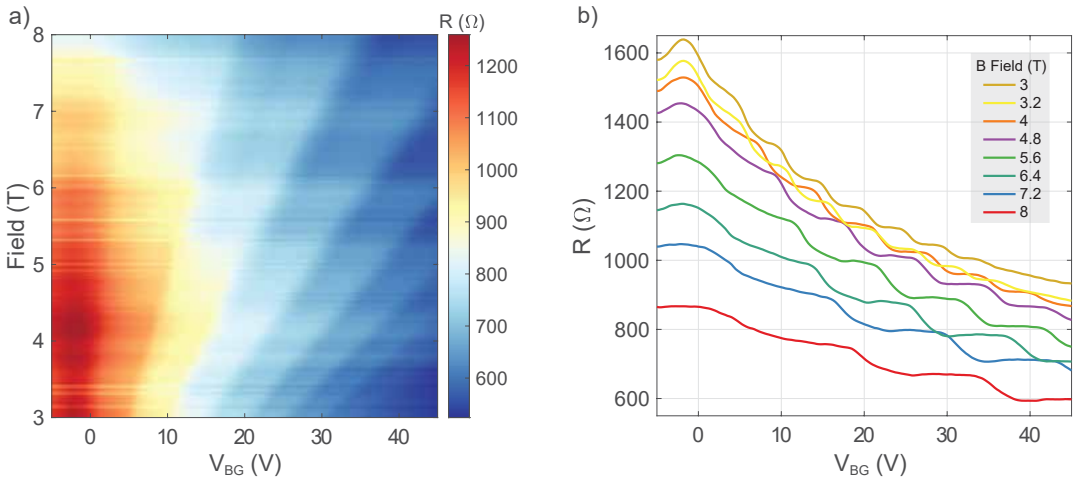

Figure D.7: Normal resistance R_n measured at a finite temperature, showing quantum Hall–like steps similar to the finite voltage measurement in Fig. D.5.

D.5 A comparison between finite-bias R_N, finite-temperature R_N, and R_{qH}

We can see how R_n measured at a finite temperature compares with that measured at a finite voltage in Fig. D.8, in which conductance is plotted in units of e^2/h for easier comparison with the quantum Hall conductance.

Both measurement schemes exhibit very similar trends in normal conductance G_n as back gate voltage is varied. The finite temperature measurement consistently yields a conductance higher than the finite voltage measurement. This could be due to the inaccuracy in either our choice of temperature, voltage bias, or both. As discussed in previous sections, because it is close to impossible to measure the true R_n with either method, we decided to employ the finite temperature method for most of the R_n measurements, due to the relative simplicity of the measurement process.

In Fig. D.9 we compare G_n (red, left axis) and G_{qH} (blue, right axis) in narrow junction 1. As discussed in Section 3.4.5 of Chapter 3, G_n ($G_{n,\,\mathrm{total}}$) is G_{qH} plus a constant offset. The only exception here is the data taken at 4 T, which shows a decreasing $G_{n,\,\mathrm{direct}}$ with gate voltage, indicating that other sample-specific factors are at play.

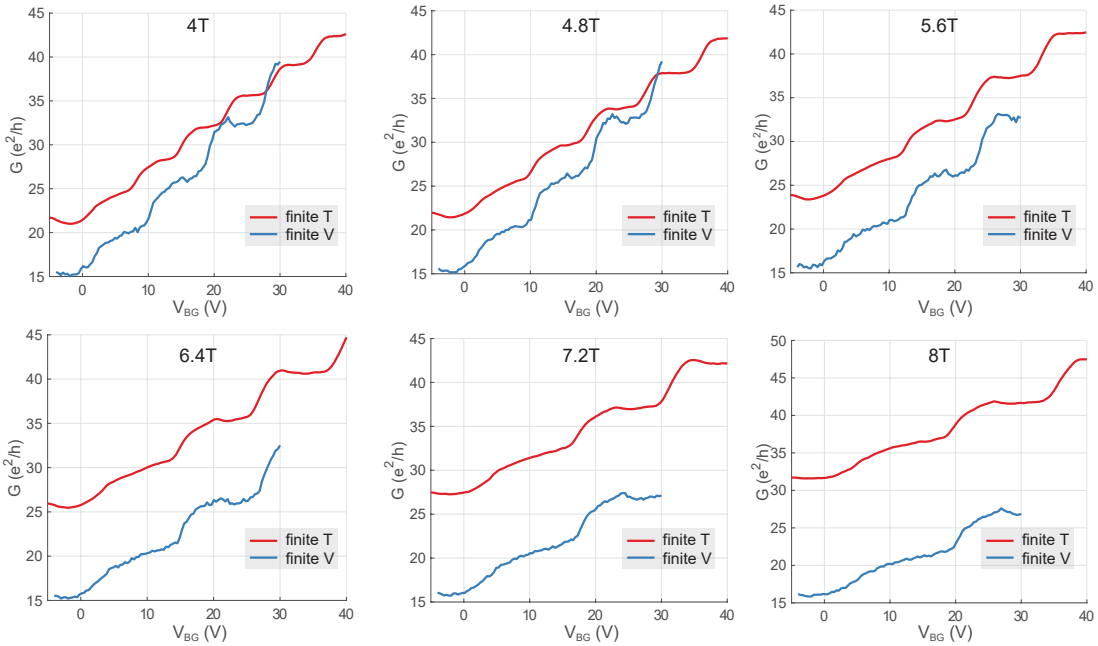

Figure D.8: A comparison between R_{n} measured at a finite temperature (red) and at a finite voltage (blue) at selected magnetic fields.

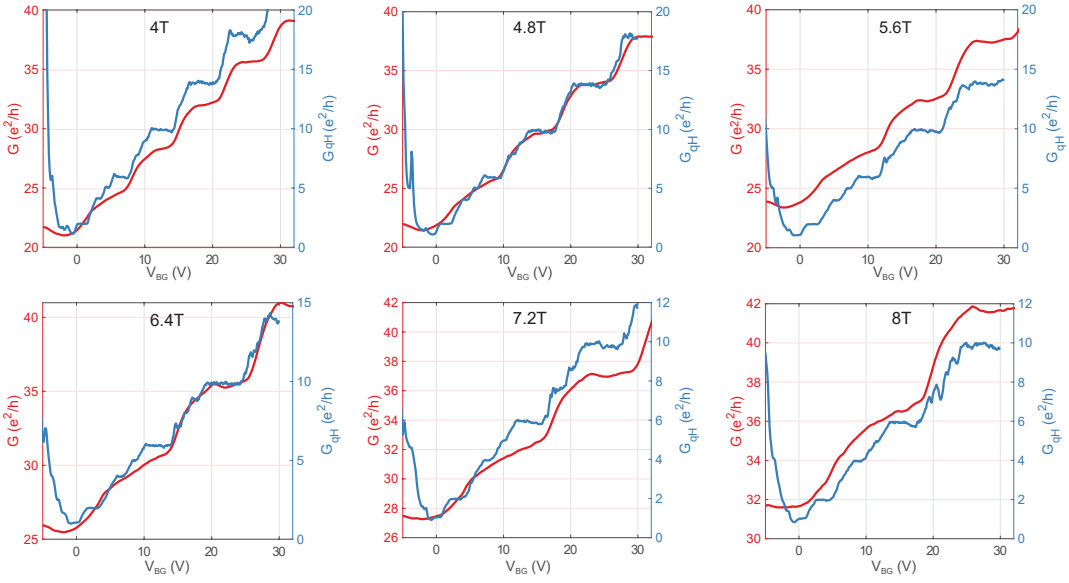

Figure D.9: A comparison between G_{n} (red, left axis), and G_{qH} (blue, right axis) in narrow junction 1.

References

[1] Albrecht, S. M., Higginbotham, A. P., Madsen, M., Kuemmeth, F., Jespersen, T. S., Nygård, J., Krogstrup, P., & Marcus, C. M. (2016). Exponential protection of zero modes in Majorana islands. *Nature*, 531(7593), 206–209.

[2] Alicea, J. (2012). New directions in the pursuit of Majorana fermions in solid state systems. *Reports on Progress in Physics*, 75(7), 076501.

[3] Alicea, J. & Fendley, P. (2016). Topological Phases with Parafermions: Theory and Blueprints. *Annual Review of Condensed Matter Physics*, 7(1), 119–139.

[4] Allen, M. T., Shtanko, O., Fulga, I. C., Akhmerov, A. R., Watanabe, K., Taniguchi, T., Jarillo-Herrero, P., Levitov, L. S., & Yacoby, A. (2016). Spatially resolved edge currents and guided-wave electronic states in graphene. *Nature Physics*, 12(2), 128–133.

[5] Bernevig, B. A. & Hughes, T. L. (2013). *Topological insulators and topological superconductors*. Princeton University Press.

[6] Bocquillon, E., Deacon, R. S., Wiedenmann, J., Leubner, P., Klapwijk, T. M., Brüne, C., Ishibashi, K., Buhmann, H., & Molenkamp, L. W. (2017). Gapless Andreev bound states in the quantum spin Hall insulator HgTe. *Nature Nanotechnology*, 12(2), 137–143.

[7] Courtney, T. H., Reintjes, J., & Wulff, J. (1965). Critical Field Measurements of Superconducting Niobium Nitride ARTICLES YOU MAY BE INTERESTED IN. *Journal of Applied Physics*, 36, 660.

[8] Deng, M. T., Vaitiekenas, S., Hansen, E. B., Danon, J., Leijnse, M., Flensberg, K., Nygård, J., Krogstrup, P., & Marcus, C. M. (2016). Majorana bound state in a coupled quantum-dot hybrid-nanowire system. *Science*, 354(6319), 1557–1562.

[9] Dynes, R. C. & Fulton, T. A. (1971). Supercurrent density distribution in josephson junctions. *Physical Review B*, 3(9), 3015–3023.

[10] Fernando Dominguez, E. H. (2020). Critical current of quantum-hall josephson junctions. unpublished.

[11] Halperin, B. I. (1982). Quantized Hall conductance, current-carrying edge states, and the existence of extended states in a two-dimensional disordered potential. *Physical Review B*, 25(4), 2185–2190.

[12] Harvey, S. (2020). special-measure.

[13] Hasan, M. Z. & Kane, C. L. (2010). Colloquium: Topological insulators. *Reviews of Modern Physics*, 82(4), 3045–3067.

[14] Hui, H. Y., Lobos, A. M., Sau, J. D., & Das Sarma, S. (2014). Proximity-induced superconductivity and Josephson critical current in quantum spin Hall systems. *Physical Review B - Condensed Matter and Materials Physics*, 90(22), 224517.

[15] Ivanov, D. A. (2001). Non-Abelian statistics of half-quantum vortices in p-wave superconductors. *Physical Review Letters*, 86(2), 268–271.

[16] Jaklevic, R. C., Lambe, J., Silver, A. H., & Mercereau, J. E. (1964). Quantum interference effects in Josephson tunneling. *Physical Review Letters*, 12(7), 159–160.

[17] Kitaev, A. Y. (2001). Unpaired Majorana fermions in quantum wires. *Physics-Uspekhi*, 44(10S), 131.

[18] Klitzing, K. V., Dorda, G., & Pepper, M. (1980). New method for high-accuracy determination of the fine-structure constant based on quantized hall resistance. *Physical Review Letters*, 45(6), 494–497.

[19] Le Calvez, K., Veyrat, L., Gay, F., Plaindoux, P., Winkelmann, C. B., Courtois, H., & Sacépé, B. (2019). Joule overheating poisons the fractional ac Josephson effect in topological Josephson junctions. *Communications Physics*, 2(1), 1–9.

[20] Lee, G. H., Huang, K. F., Efetov, D. K., Wei, D. S., Hart, S., Taniguchi, T., Watanabe, K., Yacoby, A., & Kim, P. (2017). Inducing superconducting correlation in quantum Hall edge states. *Nature Physics*, 13(7), 693–698.

[21] Lee, G.-H. & Lee, H.-J. (2018). Proximity coupling in superconductor-graphene heterostructures. *Reports on Progress in Physics*, 81(5), 056502.

[22] Li, L., Yang, F., Ye, G. J., Zhang, Z., Zhu, Z., Lou, W., Zhou, X., Li, L., Watanabe, K., Taniguchi, T., Chang, K., Wang, Y., Chen, X. H., & Zhang, Y. (2016). Quantum Hall effect in black phosphorus two-dimensional electron system. *Nature Nanotechnology*, 11(7), 593–597.

[23] Mondal, M., Kamlapure, A., Ganguli, S. C., Jesudasan, J., Bagwe, V., Benfatto, L., & Raychaudhuri, P. (2013). Enhancement of the finite-frequency superfluid response in the pseudogap regime of strongly disordered superconducting films. *Scientific Reports*, 3(1), 1357.

[24] Moore, G. & Read, N. (1991). Nonabelions in the fractional quantum hall effect. *Nuclear Physics, Section B*, 360(2-3), 362–396.

[25] Mourik, V., Zuo, K., Frolov, S. M., Plissard, S. R., Bakkers, E. P. a. M., & Kouwenhoven, L. P. (2012). Signatures of Majorana Fermions in. *Science*, 336(6084), 1003.

[26] Nadj-Perge, S., Drozdov, I. K., Li, J., Chen, H., Jeon, S., Seo, J., MacDonald, A. H., Bernevig, B. A., & Yazdani, A. (2014). Observation of Majorana fermions in ferromagnetic atomic chains on a superconductor. *Science*, 346(6209), 602–607.

[27] Nakahara, M. (1990). *Geometry, topology and physics*. Adam Hilger.

[28] Novoselov, K. S., Geim, A. K., Morozov, S. V., Jiang, D., Katsnelson, M. I., Grigorieva, I. V., Dubonos, S. V., & Firsov, A. A. (2005). Two-dimensional gas of massless Dirac fermions in graphene. *Nature*, 438(7065), 197–200.

[29] Paalanen, M. A., Tsui, D. C., & Gossard, A. C. (1982). Quantized Hall effect at low temperatures. *Physical Review B*, 25(8), 5566–5569.

[30] Prange, R. E. & Girvin, S. M. (1987). *The Quantum Hall Effect*. Springer.

[31] Pribiag, V. S., Beukman, A. J., Qu, F., Cassidy, M. C., Charpentier, C., Wegscheider, W., & Kouwenhoven, L. P. (2015). Edge-mode superconductivity in a two-dimensional topological insulator. *Nature Nanotechnology*, 10(7), 593–597.

[32] Rokhinson, L. P., Liu, X., & Furdyna, J. K. (2012). The fractional a.c. Josephson effect in a semiconductor–superconductor nanowire as a signature of Majorana particles. *Nature Physics*, 8(11), 795–799.

[33] Romito, A., Alicea, J., Refael, G., & Von Oppen, F. (2012). Manipulating Majorana fermions using supercurrents. *Physical Review B - Condensed Matter and Materials Physics*, 85(2), 020502.

[34] Shiino, T., Shiba, S., Sakai, N., Yamakura, T., Jiang, L., Uzawa, Y., Maezawa, H., & Yamamoto, S. (2010). Improvement of the critical temperature of superconducting NbTiN and NbN thin films using the AlN buffer layer. *Superconductor Science and Technology*, 23(4), 045004.

[35] Suzuki, M., Baba, M., & Anayama, T. (1987). Critical Magnetic Fields of Superconducting NbN Films Prepared by Reactive Sputtering. *Japanese Journal of Applied Physics*, 26(S3-2), 947–948.

[36] Thouless, D. J., Kohmoto, M., Nightingale, M. P., & Den Nijs, M. (1982). Quantized hall conductance in a two-Dimensional periodic potential. *Physical Review Letters*, 49(6), 405–408.

[37] Tinkham, M. (2004). *Introduction to superconductivity*. Dover Publications.

[38] Von Klitzing, K. (2005). Developments in the quantum Hall effect. *Philosophical Transactions of the Royal Society A: Mathematical, Physical and Engineering Sciences*, 363(1834), 2203–2219.

[39] von Oppen, F., Peng, Y., & Pientka, F. (2017). Topological superconducting phases in one dimension.

[40] Wakamura, T., Hasegawa, N., Ohnishi, K., Niimi, Y., & Otani, Y. (2014). Spin Injection into a Superconductor with Strong Spin-Orbit Coupling. *Physical Review Letters*, 112(3), 36602.

[41] Wang, L., Meric, I., Huang, P. Y., Gao, Q., Gao, Y., Tran, H., Taniguchi, T., Watanabe, K., Campos, L. M., Muller, D. A., Guo, J., Kim, P., Hone, J., Shepard, K. L., & Dean, C. R. (2013). One-dimensional electrical contact to a two-dimensional material. *Science*, 342(6158), 614–617.

[42] Wiedenmann, J., Bocquillon, E., Deacon, R. S., Hartinger, S., Herrmann, O., Klapwijk, T. M., Maier, L., Ames, C., Brüne, C., Gould, C., Oiwa, A., Ishibashi, K., Tarucha, S., Buhmann, H., & Molenkamp, L. W. (2016). 4\pi-periodic Josephson supercurrent in HgTe-based topological Josephson junctions. *Nature Communications*, 7(1), 1–7.

[43] Wu, Z., Xu, S., Lu, H., Khamoshi, A., Liu, G. B., Han, T., Wu, Y., Lin, J., Long, G., He, Y., Cai, Y., Yao, Y., Zhang, F., & Wang, N. (2016). Even-odd layer-dependent magnetotransport of high-mobility Q-valley electrons in transition metal disulfides. *Nature Communications*, 7(1), 1–8.

[44] Xu, J. P., Wang, M. X., Liu, Z. L., Ge, J. F., Yang, X., Liu, C., Xu, Z. A., Guan, D., Gao, C. L., Qian, D., Liu, Y., Wang, Q. H., Zhang, F. C., Xue, Q. K., & Jia, J. F. (2015). Experimental detection of a Majorana mode in the core of a magnetic vortex inside a topological insulator-superconductor Bi2Te3/NbSe2 heterostructure. *Physical Review Letters*, 114(1).

[45] Yen, C. M., Toth, L. E., Shy, Y. M., Anderson, D. E., & Rosner, L. G. (1967). Superconducting Hc-Jc and Tc measurements in the NbSingle Bond signTiSingle Bond signN, NbSingle Bond signHfSingle Bond signN, and NbSingle Bond signVSingle Bond signN ternary systems. *Journal of Applied Physics*, 38(5), 2268–2271.

[46] Zhang, Y., Jiang, Z., Small, J. P., Purewal, M. S., Tan, Y. W., Fazlollahi, M., Chudow, J. D., Jaszczak, J. A., Stormer, H. L., & Kim, P. (2006). Landau-level splitting in graphene in high magnetic fields. *Physical Review Letters*, 96(13), 136806.

[47] Zhang, Y., Tan, Y. W., Stormer, H. L., & Kim, P. (2005). Experimental observation of the quantum Hall effect and Berry's phase in graphene. *Nature*, 438(7065), 201–204.

This thesis was typeset using LaTeX, originally developed by Leslie Lamport and based on Donald Knuth's TeX. The body text is set in 11 point Egenolff-Berner Garamond, a revival of Claude Garamont's humanist typeface. The above illustration, "Science Experiment 02", was created by Ben Schlitter and released under CC BY-NC-ND 3.0. A template that can be used to format a PhD thesis with this look and feel has been released under the permissive MIT (X11) license, and can be found online at github.com/suchow/Dissertate or from its author, Jordan Suchow, at suchow@post.harvard.edu.